# In-liquid Electron Microscopy and Diffraction for real-time observation and structural analysis

Dissertation with the aim of achieving a doctoral degree
at the Faculty of Mathematics, Informatics and Natural Sciences
Department of Chemistry
of Universität Hamburg

submitted by Sercan Keskin
2016 in Hamburg

Day of oral defense: 28.10.2016

The members of the examination board:

Prof. Dr. R.J. Dwayne Miller

Prof. Dr. Ulrich Hahn

Prof. Dr. Martin Trebbin

# I.    List of Publications

Sercan Keskin et al., "Visualization of Multimerization and Self-Assembly of DNA Functionalized Gold Nanoparticles Using In-Liquid Transmission Electron Microscopy", J. Phys. Chem. Lett., 6, 4487−4492, 2015.

Stephanie Manz et al., "Mapping atomic motions with ultrabright electrons: towards fundamental limits in space-time resolution", Faraday Discuss., 177, 467, 2015.

Tadahiko Ishikawa*, Stuart A. Hayes*, Sercan Keskin et al., "Direct observation of collective modes coupled to molecular orbital–driven charge transfer", Science, 350, 6267, 1501-1505, 2015.

Masaki Hada et al., "Bandgap Modulation in Photoexcited Topological Insulator $Bi_2Te_3$ via Atomic Displacements", J. Chem. Phys. 145, 024504, 2016.

## II.  Table of Content

## III. List of Abbreviations

| | |
|---|---|
| ASE | Advanced silicon etch |
| AuNP | Gold nanoparticle |
| BF | Bright field |
| BOE | Buffered oxide etching |
| BSE | Back scattered electrons |
| CCD | Charge coupled device |
| CDW | Charge density wave |
| CS | Charge-separated phase |
| CTEM | Conventional transmission electron microscopy |
| CVD | Chemical vapor deposition |
| DF | Dark field |
| DFT | Density functional theory |
| DLS | Dynamic light scattering |
| DPCP | diphenylcyclopropenone |
| DRIE | Deep reactive ionic etching |
| dsDNA | double stranded deoxyribonucleic acid |
| DTEM | Dynamic transmission electron microscopy |
| E-diff | Electron diffraction |
| EGF | Epidermal growth factor |
| ESEM | Environmental scanning electron microscopy |
| FED | Femtosecond electron diffraction |
| FWHM | Full width half maxima |
| GHS | Globally harmonized system of classification and labelling of chemicals |
| HT | High temperature |
| Hz | Hertz |
| IC | Integrated circuit |
| ICP | Inductively coupled plasma |
| KOH | Potassium hydroxide |
| LPCVD | Low pressure chemical vapor deposition |
| LT | Low temperature |

| | |
|---|---|
| N-PR | Negative photoresist |
| Nt | nucleotide |
| PBS | Phosphor buffer saline |
| PECVD | Plasma enhanced chemical vapor deposition |
| PFA | Paraformaldehyde |
| PIPT | Photoinduced phase transition |
| PR | Positive photoresist |
| PSMA | Prostate specific membrane antigen |
| PVD | Physical vapor deposition |
| REGAE | Relativistic electron gun for atomic exploration |
| RDC | Radial distribution curve |
| RIE | Reactive ionic etching |
| RNA | Ribonucleic acid |
| Sccm | Standard cubic centimeter per minute |
| SiN | Silicon nitride |
| SiO | Silicon oxide |
| SNR | Signal-to-noise ratio |
| ssDNA | single stranded deoxyribonucleic acid |
| STEM | Scanning transmission electron microscopy |
| TEM | Transmission electron microscope |

# 1. Zusammenfassung

Eine der größten Herausforderungen im Gebiet der Lebenswissenschaften ist die Untersuchung chemischer und biologischer Reaktionen unter möglichst naturnahen Bedingungen. Gleichzeitig wird eine zeitliche Auflösung angestrebt, die es ermöglicht die Korrelation zwischen Struktur und Funktion aufzudecken. Im Allgemeinen wird in den Naturwissenschaften immer angestrebt, Bewegungen abzubilden wir sie geschehen – bis zum atomarem Niveau. In der Biochemie möchte man dies in einer naturnahen Umgebung darstellen, was bedeutet, dass die Probe in wässriger Lösung beobachtet wird. Die ultimative Abbildungsmethode mit Elektronen fehlt für diesen Zweck, wobei hauptsächlich Fragen der Probenerstellung und die Strahltechnologie selbst zu beantworten sind.

Innerhalb dieser Dissertation lag der Hauptschwerpunkt auf der Verbesserung der Probenvorbereitung für konventionelle Transmission – Elektronenmikroskopie (CTEM) und Femtosekunden - Elektronendiffraktion (FED) im flüssigen Zustand. Silizium basierte Mikro- und Nanofabrikationstechniken wurden angewandt um die neueste Generation nanofluider Zellen herzustellen und um ihre Effektivität bezüglich der Verbesserung räumlicher Auflösung zu erhöhen. Diese Probenhalter für Elektronenmikroskopie in Flüssigkeit wurden hauptsächlich für zwei verschiedene Systeme zum Einsatz gebracht: Erstens wurde eine statische Variante der Zelle verwendet, um die Dynamik von DNA Hybridisierung in Lösung zu beobachten. Zweitens wurden Krebszellen im TEM in-situ abgebildet, um ihre Morphologie und die Aufnahme von an Goldnanopartikel gebundene Oligonukleotide zu beobachten, die potenziellen Nutzen bei der gezielten Verabreichung von Medikamenten haben.

Das Verhalten der Fenster abhängig von den Dimensionen der nanofluiden Zelle wurde im Hochvakuum mit Hilfe eines Interferometers charakterisiert. Wir können die Dicke der Zelle im Vakuum interferometrisch bestimmen und einen Zusammenhang zwischen der im TEM erreichten räumlichen Auflösung herstellen. Die erhaltenen Ergebnisse sind für die weitere Entwicklung von nanofluiden Zellen für die Abbildung und Diffraktion mit Elektronen wichtig. Innerhalb dieser Arbeit wurde Elektronenbeugung erstmals in einer nanofluide Zelle beobachtet. Dabei wurde eine die Dicke der Flüssigkeitsschicht durch differentielles Pumpen kontrolliert. Die Methode erlaubt es direkt vor Ort die Probe zu liefern und fließen zu lassen. Die Ergebnisse heben das Potential der nanofluiden Zelle für die Untersuchung molekularer Dynamik in Lösung hervor, besonders für stroboskopische Messungen auf der Zeitskala von Femtosekunden.

# 2. Abstract

One of the biggest challenges in life sciences is to investigate chemical and biological reactions as they occur under natural conditions with sufficient spatiotemporal resolution to fully reveal the structure-function correlation. As a more general aspect in science, the aim has been to watch atomic motions as they occur. In biochemistry, natural environment refers to solution. An ultimate method to be implemented for this purpose is lacking for electrons mainly due to the difficulties in sample preparation and probe source design.

In this thesis, we focused on improving sample preparation methods for conventional transmission electron microscopy (CTEM) and femtosecond electron diffraction (FED) in solution phase. Silicon based micro- and nanofabrication techniques are used to manufacture the current generation of nanofluidic cells and developed new methods to improve its effectiveness regarding the spatial resolution with electrons. This device is used for mainly two different systems with in-liquid TEM in this thesis work. We used a no-flow version of the nanofluidic cell first to investigate DNA hybridization dynamics in solution. Secondly, we imaged cancer cells *in situ* with TEM to investigate their morphology differentiation and oligonucleotide bound gold nanoparticle uptake for potential use in targeted drug delivery.

The behavior of the nanofluidic cell windows in high vacuum has been characterized for different window lateral dimensions using custom designed thin-film interferometer. We can measure the sample cell thickness interferometrically and associate it with the obtained spatial resolution in TEM. The obtained results have importance for developing more advanced nanofluidic cells for both real space imaging and diffraction with electrons.

The nanofluidic cell was used first time for electron diffraction from liquid water in the course of this thesis. We used a differential pressure method to control the thickness of the liquid layer in flow cell allowing *in situ* sample exchange.

The obtained results highlight the potential of the nanofluidic cell to study molecular dynamics in solution in femtosecond time scale with ultra-fast stroboscopic techniques.

# 3.    Introduction

## 3.1.    Electrons as Probe Source

Electrons and X-rays are fundamentally superior to visible light for imaging applications. Conventional or super resolution light microscopy allows *in situ* imaging of biomacromolecules and organisms in natural conditions; however the spatial resolution they can achieve is limited by the wavelength of the source of illumination. Therefore, current electron and X-ray based sources are much more promising to reach atomic level resolution. Besides obtaining atomic resolution, they can also provide time resolution, which is a measure of the camera readout speed. However, mechanical speed is not adequate to capture fast phenomena on the relevant time scales. In order to investigate such fast dynamics, the probe speed has to be faster than the atomic motions governing chemical and biological changes. It is now possible to capture dynamic events in femtosecond (1 fs = $10^{-15}$ s) or even attosecond ($10^{-18}$ s) time scales with pulsed laser technology, which is offering a range of shutter speeds for different atomic motions to make so-called 'molecular movies'. With modern laser technology, today's ultra-bright compact electron sources can achieve a temporal resolution of <200 fs with $10^5$-$10^6$ electrons per pulse with a beam spot size of ~100 μm.[1,2]

In comparison of electrons with X-rays as probe source, first it should be pointed out that electrons interact with matter much stronger than X-rays. As charged particles, electrons are scattered mainly by the Coulomb potential of the atomic nucleus, on the other hand X-rays are scattered by photon-electron interactions by the electronic charge density. As a fundamental advantage of electrons over X-rays, the scattered beam has higher intensity and carries the direct information for the positions of the atoms in a specimen. The massive difference in scattering cross section for electrons and X-rays ($10^5$-$10^6$ higher for electrons) makes table top electron sources more efficient to investigate molecular structure of liquid or gas specimen compared to their X-ray counterparts.[1,3]

There are two main considerations regarding the use of electrons for exploration at the atomic level. First, the number density of electrons per time unit must be sufficient to gain valuable information from irreversible samples. Especially organic samples suffer from dramatic structure changes after electron or photon exposure. In a typical pump-probe experiment, the laser perturbation and electron probe are overlapped at the sample position. The difference between pump+probe and only probe signal reveals the perturbation induced dynamics for the

target system. Note that each of these beams can cause irreversible damage on the sample. Second, the thickness of sample should be on the order of the elastic mean free path of the electrons at a certain energy. This second issue is easier to overcome for solid matter compared to samples in liquid or gas forms with standard methods such as microtoming, ion milling, thermal evaporation and sputtering. This problem is less pronounced for X-rays due to the much higher elastic mean free path than the one for electrons (at any energy). Therefore, X-ray sources can use tens of micrometers thick liquid samples, which can simply be obtained by liquid jets.[4–6] On the other hand, having a liquid layer of a few hundreds of nanometers in thickness under high vacuum conditions requires more complex and nontrivial sample preparation methods, which will be discussed in detail in the following chapters.

The most common use of electrons as a probe source is the transmission electron microscope (TEM), which can be operated either in imaging or diffraction mode. Imaging experiments in real space can generate highly magnified frames of a specimen and are currently used as a straightforward method in biology, medicine and material sciences. Structural information can also be obtained from crystal forms of organic or inorganic materials in diffraction mode.[7]

A perturbation element (such as laser excitation or thermal induction) synchronized with a probe source (electrons or X-rays) allows performing time-resolved diffraction experiments with high signal-to-noise ratio (SNR) and temporal precision. A number of groups developed ultrafast electron diffraction setups with pulsed sources rather than the ones with continuous current to achieve femtosecond resolution.[8,9] Figure 3.1 shows a typical pump-probe setup. Typically, one magnetic lens is used in the setup to collimate the electron bunch before or after the sample. In the experiment, a photocathode is hit by an ultra-short pulse laser to generate ultra-short electron pulses. The electrons are accelerated via a high voltage towards an anode plate. The sample is probed by the electron pulses at a certain time point upon hit by an excitation pulse. The time delay between excitation and probing on the sample is varied by changing the optical path; hence the sample can be probed at various time points upon excitation. The temporal evolution of the acquired signal (intensity profiles) gives the time-resolved dynamics of the target system.

This technology was also adapted recently to commercial TEMs however with lower temporal resolution. It was shown that the use of aberration correctors, phase plates and energy filters increase the attainable spatial resolution and contrast.[10,11]

6
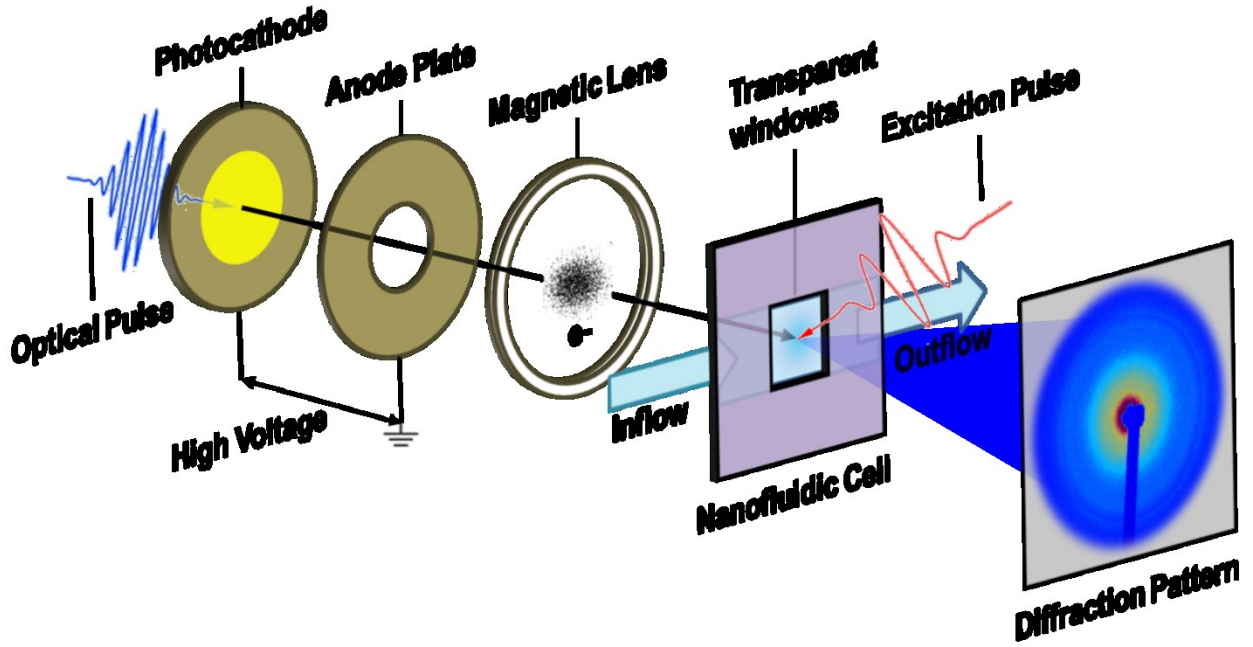
Figure 3.1. A typical layout of a pump-probe experiment (Not drawn to scale). A nanofluidic cell for liquid-state samples is depicted as a target in the layout. For solid-state samples, the target can be crystalline thin films on a support mesh.

## 3.2. Electron-Matter Interactions

Electrons are negatively charged and have both particle and wave properties. Based on *Louis de Broglie*'s formulation of wave-particle duality, the particle momentum $\rho$ can be related to its wavelength $\lambda$, represented by:

$$\lambda = \frac{h}{\rho},$$
(3.1)

(*h:* Planck constant). We can relate the momentum to the electron mass and kinetic energy with the equation given below,

$$\rho = m_0 v = \sqrt{2m_0 eV},$$
(3.2)

(*$m_0$*: electron mass, *v*: velocity, *eV*: electron kinetic energy accelerated through a potential drop V). Now we can find the relationship between the energy of an electron and its wavelength:

$$\lambda = \frac{h}{\sqrt{2m_0 eV}}.$$
(3.3)

7

From this equation, it can be seen that by increasing the kinetic energy of electrons, we can decrease their wavelength.

When matter is exposed to high energy electrons (> 500 eV)[12], the possible interactions between them can be divided into two main types: Elastic and inelastic interactions. In elastic events, electrons scatter from an atom without energy transfer, but change their momentum due to Coulomb interaction. When scattering from an isolated atom, electrons may interact with the positive potential of the atom and scatter at a higher angle or may interact with the electronic cloud of the atom and scatter with low angle. The Coulombic force (*F*) is represented by:

$$F = \frac{Q_1 + Q_2}{4\pi\varepsilon_0 r^2},$$
(3.4)

where *r* is the distance between charges $Q_1$ and $Q_2$ and $\varepsilon_0$ is the dielectric constant. It can be seen from this equation that as the distance of an electron to the positive core becomes smaller, the attractive force becomes stronger and consequently the probability of a scattering event with high angle or backwards increases. Figure 3.2 illustrates this phenomenon. A complete back scattering of electrons from positive core can infrequently occur, the electrons undergo such an event are called *backscattered electrons*. The amount of backscattered electrons increases with increasing atomic numbers of target, however it does not strongly depend on the acceleration voltage of the electrons. The signal arising from backscattered electrons is used for imaging the surface topography of the sample.

The constructive and destructive interference of the elastically scattered electrons from multiple atoms of a specimen result in a diffraction pattern, which can result in either bright spots or rings or even a mixture of both, depending on the crystallinity of the specimen. If sample atoms are not symmetrically arranged such as liquids, diffuse rings are expected in the diffraction pattern.
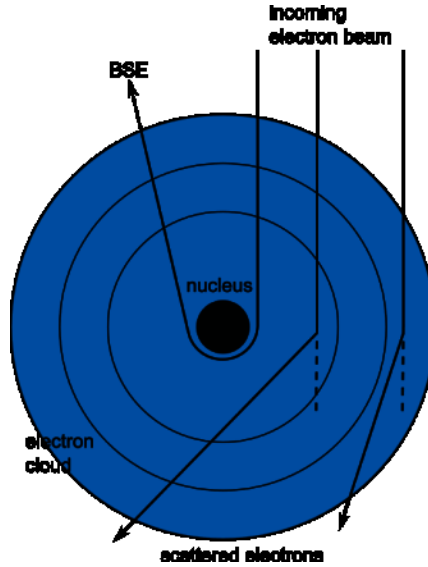
Figure 3.2.Scattering of electrons from an isolated atom. BSE: Back scattered electrons.

When a high energy electron interacts with a specimen, it might lose some fraction (or even total) of its energy and deflect under various scattering angles. If the incoming electron beam interacts with the inner shell electrons of specimen atoms and transfers excessive amount of energy, the inner shell electron(s) can be ejected from the atom. Then the atom goes into an excited state, and this phenomenon is called *inner shell ionization*. The vacancy in the inner shell is filled with an electron from the outer shell resulting an X-ray or Auger electron emission. If an electron is ejected from conduction or valence band (outer shell) of an atom, these electrons are called secondary electrons with a typical energy of <50 eV. These types of electrons are used in scanning electron microscopy (SEM) as standard signal and important for scanning transmission electron microscopy (STEM) to construct images of the specimen surface with high resolution. Signals arise from inelastic events are mainly utilized in analytical methods since they are specific to the atoms or molecules of the specimen (e.g. characteristic X-rays).

An electron can scatter in a specimen single or multiple times. The probability of a scattering event in a particular way depends on electron mean free path ($\Lambda$) or interaction cross section ($\sigma$). The interaction cross section has units of area but it represents a probability that a scattering event will occur. Consequently, the probability of a scattering event is attributed to the sum of all elastic and inelastic terms,

$$\sigma = \sigma_{elastic} + \sigma_{inelastic} \text{,} \tag{3.5}$$

9

and the total scattering cross section for a number of atoms in a certain volume is represented by:

$$\sigma_{total} = N\sigma_{atom} = \frac{N_A \sigma_{atom} \rho}{A},$$ (3.6)

($A$: Atomic mass, $\rho$: Atomic density, $N_A$: Avogadro number). For a specimen with a thickness $t$, the probability of scattering from the specimen is represented by:

$$\sigma_{total}t = \frac{N_A \sigma_{atom} \rho t}{A},$$ (3.7)

Eq. 3.7 gives the important variables that can change the scattering probability from a specimen. For thinner samples, it is more likely (and ideal) that most of the electrons scatter once or do not scatter at all in the sample. For elastic scattering from a nucleus, the radius of the interaction cross section is defined by:

$$r_{elastic} = \frac{Ze}{V\theta},$$ (3.8)

where $e$ is electron charge, $V$ is electron potential, $\theta$ is scattering angle and $Z$ is the atomic number of the target. This equation indicates that the higher the electron energy, the lower the probability of a scattering at high angle or a multiple scattering event takes place. More scattering events lead to more energy transfer and eventually the incoming beam is absorbed completely in the specimen. Also, higher atomic numbers lead to higher scattering probability for electrons in a specimen. If the electron is scattered close to the nucleus, it deflects with a wider angle, which is directly related to the image contrast in TEM. The atomic number directly dominates the elastic interactions with the nucleus and it is very important when the scattering needs to be enhanced, especially for low-Z biological specimens.

Another important parameter to have a qualitative sense of electron-matter interactions is electron mean free path, which represents the probability of a single electron being scattered in a distance through the material, or in other words, the average distance that an electron travels in a material before first collision occurs. It is the inverse of the total scattering cross section and given by:

$$\Lambda = \frac{1}{N\sigma_{atom}}.$$ (3.9)

Since electrons have very large scattering cross section (compared to X-rays), their elastic mean free path in non-relativistic regime is on the order of tens of nanometers for most materials. The elastic mean free path is 5 times longer for electrons in MeV energy range.[13,14] Figure 3.3 shows the mean free path of electrons as a function of their energy in aluminum derived from the Dirac

equation.[13] The probability of multiple scattering is reduced in MeV range for both elastic and inelastic scattering. Table 3.1 gives the fundamental constants mentioned above and some electron wavelength values at different energies.[7,15]
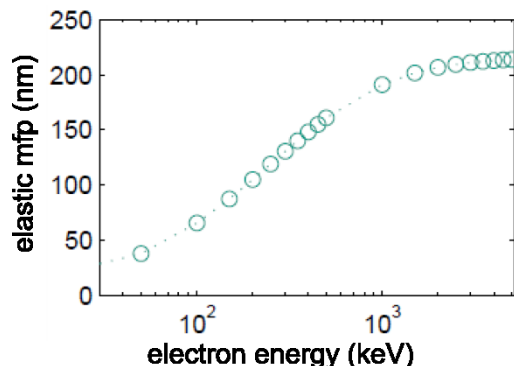


Figure 3.3. Elastic mean free path in Aluminum at increasing electron energies. (Taken from reference-13)

Table 3.1. Fundamental constants regarding electrons and their wavelengths at different energies[7,15]

| Electron charge | - 1.602 x $10^{-19}$ C | Electron energy (keV) | wavelength (nm) |
|---|---|---|---|
| 1eV | 1.602 x $10^{-19}$ J | 100 | 0.00370 |
| Rest e mass ($m_0$) | 9.109 x $10^{-31}$ kg | 200 | 0.00251 |
| Planck's constant (h) | 6.626 x $10^{-34}$ J·s | 400 | 0.00164 |
| Avogadro constant ($N_A$) | 6.022 x $10^{23}$ mol$^{-1}$ | 1000 | 0.00087 |

## 3.3.    Electron Microscopy

An electron microscope is a tool using high energy electrons to resolve structures in mostly life and material sciences at very high magnifications up to $10^6$-$10^7$. After *Louis de Broglie*'s formulation of wave-like properties of electrons with a wavelength smaller than visible light, it took short time for the idea of an electron microscope to be proposed, and the term was first used in the famous publication of Knoll and Ruska (1932).[16] Commercial TEMs were developed first in the UK four years after this publication and developed over time until today's state of the art systems offered by Hitachi, JEOL, Philips and FEI.

### 3.3.1. Transmission Electron Microscopy

Conventional TEM (CTEM) uses the transmitted electrons from a specimen as signal. It can be operated either bright field or dark field mode. In bright field (BF) imaging, some fraction of the incoming electrons is strongly scattered by the specimen based on different atomic weights and densities in the specimen (Eq. 3.8). The non-scattered beam appears as bright background in the detector while the features appear as darker regions. In dark field (DF) imaging, the main beam is blocked before detector and the image is constructed only by scattered electrons. This imaging mode is used for STEM, where the apparatus is equipped a specialized large area detector. The BF or DF images can be obtained by CTEM at a typical magnification range of 25,000-100,000 by simply adjusting according lenses of the microscope. CTEM uses a collimated beam, however beam diameter is larger compared to STEM and most scattered electrons stay in the same region with incident beam hence it enables good BF imaging.

The above mentioned DC-sources generate a continues current of electrons, while the specimen is exposed by. Pulsed electron beams can be realized making use of the photoelectric effect. Here a laser pulse hits on a metal (or semiconductor) plate (photocathode) to extract electrons.[17] Several groups have modified commercial TEMs to generate electron pulses on nanosecond time scale for time resolved experiments.[18,19]

A more detailed description of above given terms and some important concepts in TEM will be discussed in the following chapters.

### 3.3.2. The Characteristics of the Electron Beam

The performance of an electron source can be described by the terms brightness, coherence and stability. Brightness (β) is defined as the current per unit solid angle of the source:

$$\beta = \frac{4i_e}{(\pi d_0 \alpha_0)^2},\qquad\qquad(3.10)$$

where $i_e$ is the cathode emission current, $d_0$ is the diameter and $\alpha_0$ is divergence angle of the electron source. It is an important fact shown in Eq. 3.10 that brightness increases linearly with increasing accelerating voltage. Higher brightness corresponds to larger number of electrons per unit area on the sample. Consequently more information can be obtained from the sample with shorter exposure times minimizing image drift and other instabilities.

Another important parameter is the coherence of the electron beam. The light coming from a light bulb is incoherent, which means that it consists of photons in different frequencies.

We can discuss coherence under two definitions: Temporal coherence and spatial (transverse) coherence. The first one is a measure of correlation between waves (electrons) along the direction of propagation and the latter is a measure of correlation between waves transverse to the direction of propagation. A coherent electron beam indicates that the electrons in the beam have the same frequency (wavelength) at any point, so the same coherence length ($L_c$), which is represented by:

$$L_c = \frac{vh}{\Delta E},$$ (3.11)

($\Delta E$ is the energy spread of the beam and $v$ is the electron velocity). This sort of coherence is attributed to temporal coherence, which indicates how monochromatic the source is. For an electron source with zero energy spread, the temporal coherence length would be infinite. Eq. 3.11 indicates that it is necessary to have a stable power and high voltage supply to the source so that all the electrons have a small energy spread leading to a well-defined wavelength. On the other hand, spatial coherence is attributed to the size of the source. In case of emitting electrons from the same point at the source leads perfect spatial coherence. Therefore, smaller sources provide better coherence. The effective source size for coherent illumination can be defined as:

$$d_c = \frac{\lambda}{2\alpha},$$ (3.12)

where $\lambda$ is the electron wavelength and $\alpha$ is the divergence angle of the emitted electrons from the source. There are several options to increase the spatial coherence such as making the source size smaller (field emission sources) or using smaller illumination aperture to reduce $\alpha$ or increasing the electron wavelength by decreasing the acceleration voltage. Spatial coherence is very important for studying structures for large lattice constants (protein crystals) and for obtaining high resolution phase-contrast images. A phase-contrast image refers to a coherent imaging mode, which is produced by the interference of the diffracted waves from a specimen. Typical coherence length in an EM is a few hundred of nanometers ($\Delta E \sim 0.3\text{-}3$ eV).[7]

Stability of the high voltage supply and the current delivered from the source is important since it can affect the intensity on the screen (pixel intensity of the images). Commercial TEMs with thermionic emitters are generally very stable with an expected variation less than ±1 % per hour. On the other hand, field emitters are less stable and they require better vacuum conditions to maintain stability.

In summary, beams from small sources are more spatially coherent than large beams. The more coherent and parallel beams can provide better phase contrast in real space imaging and

sharper diffraction patterns, which simplifies the analysis and interpretation afterwards. Smaller electron sources can offer better spatial coherence, however they might suffer from low stability.

### 3.3.3.    Electron Microscope Instrument

The design of the electron gun differs for thermionic and field emission sources. Lanthanum hexaboride ($LaB_6$) crystals or tungsten metal are the general thermionic sources used for modern TEM technology. If a material is heated up to a temperature, which is high enough to overcome the natural barrier that prevent escaping of electrons from the material (material's work function, $\Phi$), the material starts emitting of its electrons. The $LaB_6$ crystals are heated by running a current through a metal wire to cause thermionic emission. The cathode emits the electrons towards the anode, which has a hole in the center. Electrons are accelerated by the high voltage applied between the crystal and anode plate. On the other hand, field emission guns use an extra fine tip (<100 nm) where the electrons are emitted from and two different anode plates. The first anode provides a relatively low voltage to only extract the electrons from tip and the second anode accelerates the electrons up to set energy (e.g. 100 keV). Since we used a thermionic $LaB_6$ source for the TEM experiments in this thesis, we will not go into detail for field emission sources.

After electrons generated from the source they go through a cross-over point by the first electrostatic lens called Wehnelt cap before they go through a series of lenses in the microscope column (Figure 3.4). The electrons are then focused onto the specimen using a set of magnetic lenses. We simply change the strength of the magnetic lenses during operation to change the magnification and focus of the electron beam. Lenses are combined with various apertures to control the divergence or convergence of the electron beam, change the illumination area or angle and brightness on the specimen. Larger apertures provide larger illumination angles and brightness.

Magnetic electron lenses have generally two parts. There is first a cylindrical core of magnetically soft material such as iron with a hole in the center, which is called polepiece and the central hole is called the bore of the polepiece. The second part of the lens contains a coil copper wire surrounding the polepiece. Simply, when a current is passed through the coil, a magnetic field is generated in the bore. The objective lens located after the specimen (very close to the specimen plane) is the strongest lens compared to other lenses in the system and has a focal length of a few millimeters. It generates an image which is magnified by the other lenses. The

14

overall alignment of the lens system must be done carefully to obtain high quality images. The objective lens aperture defines the image contrast and resolving power, which are very important if high resolution is required. Here it should be indicated that in contrast to glass lenses, magnetic lenses are not perfectly ideal due to fundamental reasons, which limits the resolution of the microscope.

The lenses in a TEM also govern the properties of *depth of field* and *depth of focus*. The first one, $D_{ob}$, refers to the object and it is the distance along the axis of the object plane within the object can be moved without detectable loss of focus in the image. The second one, $D_{im}$, refers to the image and it is the distance along the axis of the image plane within the image seems focused. These terms are illustrated in Figure 3.5. As seen, high $D_{ob}$ and $D_{im}$ provide us more freedom to image different heights in an object for more spatial information. This is important especially for imaging 3D objects, for instance a live cell in liquid, where different sub-cellular structures locate at different heights within the live cell.

Spherical aberration, chromatic aberration, and astigmatism are the most pronounced fundamental limitations that can considerably decrease the performance of the microscope. Spherical aberration ($C_s$) occurs when the lens magnetic field behaves differentially; as a result, off-axis electrons are bent more strongly toward the axis. This results a spatial distortion in the imaging plane, and consequently limits the attainable resolution especially at higher magnifications. Spherical aberration in objective lens is the most severe one since it escalades all the other errors caused by pre-locating lenses in the column hence it can dramatically limit the details that can be resolved in a TEM image. Highly complex, computer-controlled sets of quadrupoles or hexapoles are used to correct $C_s$ by diverging the off-axis rays that they converge to spatially overlap with the other rays at a certain point. $C_s$ corrector is the most prominent developments recently in TEM technology.[20,21]
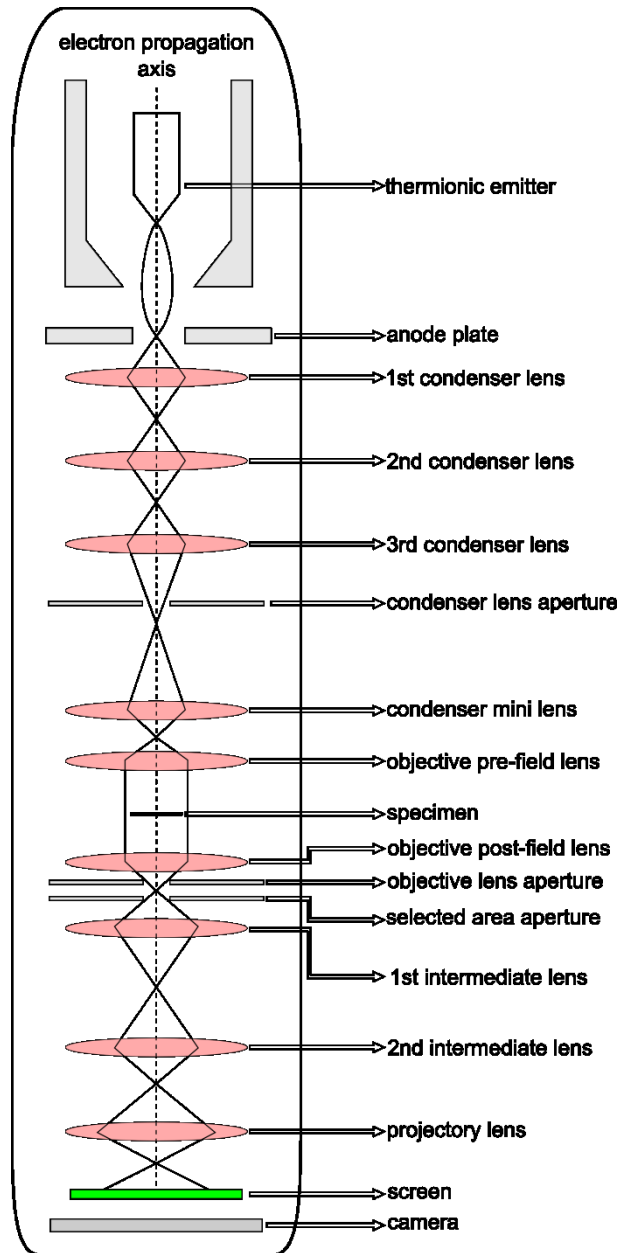
Figure 3.4. Schematic overview of a typical TEM.

Chromatic aberration ($C_c$) is related to the energy spread (or wavelength spread) of the electrons. Assumingly all emitted electrons are accelerated to the same energy by high voltage supply (monochromatic), however in reality there is a $10^{-6}$ deviation expected from the typical stability of the power supply (e.g. 0.1 eV for 100 keV). For thin samples, effect of $C_c$ is typically small on image resolution compared to $C_s$. An easy way to avoid $C_c$ is to use thin samples since it heavily depends on the energy loss of the electrons in the sample.
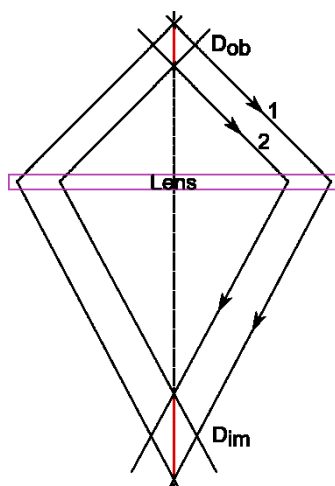
Figure 3.5. The illustration of the depth of field and depth of focus. Rays 1 and 2 represent the extremes of the ray paths.

Astigmatism occurs when the electrons are exposed to an inhomogeneous magnetic field as they move in the beam axis. It arises from the structural imperfections in the iron polepieces of the lens. Also, if the introduced apertures are not well centered on the axis or not clean, they might disturb the magnetic field and deflect the beam. However, these inhomogeneities can be balanced with a compensating field using stigmators that are placed in the microscope system.

In order to detect electrons, we need an interface to convert the electron intensity distributions into visible signal and record it. In case of detecting forward-scattered electrons from the specimen, the signal (electrons) is digitized and the digital image is displayed on a fluorescent screen coated with phosphor (such as zinc sulfide). Developments in computer technology lead the idea of recording analog TEM images via cameras. Charge-coupled device (CCD) cameras capable of collecting charge generated by electron beams, are generally coupled to fluorescent screen for on-line viewing and processing of TEM images. CCDs are manufactured by common silicon technology hence they offer low cost and variety in shape and dimensions. Besides source brightness, the camera readout speed is the main limitation of attainable time resolution in TEM imaging. For standard TEM acquisition, a frame rate of 1 hertz (Hz) is sufficient. However, *in situ* TEM requires much higher readout speed to resolve fast events in biology and chemistry. Currently it is possible to achieve a frame rate of kHz and even $10^5$ Hz with fast readout speed CCD cameras. As an alternative way to achieve high temporal resolution,

the concept of dynamic TEM (DTEM) was implemented including a pulsed laser in the TEM column to generate short electron pulses.

### 3.3.4.    Resolution and Contrast in Real-Space Imaging

For light microscopy, image resolution is typically estimated by the Rayleigh criterion. The criterion defines the smallest distance that can be resolved:

$$\delta = \frac{0.61\lambda}{\mu \sin \beta},$$    (3.13)

where $\lambda$ is the wavelength of the radiation, $\mu$ is the refractive index of the viewing medium and $\beta$ is the semi-angle of collection of the magnifying lens. This corresponds to around 300 nm for a typical light microscope. Recently developed super resolution microscopy techniques can achieve resolution greater than diffraction limit of light. Stefan Hell has developed stimulated emission depletion microscopy (STED), which is based on non-linear optical effects. Hell at al. obtained ~50 nm resolution on single quantum dots and could visualize synaptic vesicles of 40 nm in size in neuron cells.[22,23]    Despite STED is a great improvement over conventional fluorescence microscopy, it requires high intensity laser excitation, which often causes sample damage and photobleaching.  Another super resolution technique, namely stochastic optical reconstruction microscopy (STORM) uses photo-switchable fluorescent labels and a series of imaging cycles to construct an image. Huang et al. used STORM and demonstrated the 3D morphology of cellular structures with 20-30 nm resolution.[24]  Despite these techniques allow imaging under ambient conditions, they compulsorily use fluorescent labels and achieved resolution to-date is not sufficient even for nanotechnology. It is well appreciated that there is much more to discover in smaller scales (e.g. single protein imaging).

*Louis de Broglie* showed that diffraction limit of light can be overcome with wave properties of electrons. In Eq. 3.13, $\mu\sin\beta$ is called *numerical aperture* and can be approximated to ~1 (assuming a small angle of $\beta$ in radians and $\mu$~1), then the resolution corresponds to approximately half of the wavelength of the illumination source. Considering electrons have very small wavelengths (Table 3.2), a resolution down to pm range can theoretically be achieved. However, we cannot achieve such resolution because field inhomogeneities in magnetic lenses, which is a fundamental limiting factor.

Sample thickness is one of the main factors in resolution. Thick samples lead to multiple scattering events, which can result in chromatic aberration in the lenses after electrons

transmitting the sample. For *in-situ* TEM studies, specimen motion might cause blurring of the image, which depends on the velocity of monitoring objects and the camera readout speed. All limitations mentioned so far are related to how the electron trajectory is affected. In addition, electron induced damage and difficulties in the sample preparation can limit the highest attainable resolution.

By considering the advantages of high energy electrons especially for relatively thick specimens (Table 3.1 and Eq. 3.7), high voltage electron microscopes with accelerating potentials up to 3 MV were developed. However they were mostly operated to investigate radiation damage into specimens rather than increasing the resolution limit. Electron microscopes operated at intermediate voltage, 200-400 kV, were introduced in the 1980s and commercialized since they can also offer high resolution close to that obtained at 1 MV. It was shown that combination of intermediate energy electrons with $C_s$ and $C_c$ correctors achieve a resolution of ~1 Å. In general, it is considered more efficient to invest in aberration correctors to achieve high resolution rather than increasing the acceleration voltage.

Contrast is as much important as resolution to construct good TEM images. The Rose criterion suggests that signal is detectable if it is 3-5 times higher than background noise.[25] This can be attributed to minimum contrast of an object, which is detectable by a microscope. If we simply define the contrast ($C$), it is the intensity difference between two adjacent areas:

$$C = \frac{I_2 - I_1}{I_1} = \frac{\Delta I}{I_1} = 1 - e^{-Q\Delta t} , \tag{3.14}$$

where $Q$ is the total elastic scattering cross section and $\Delta t$ represents a change in the sample thickness. As seen, a change in the sample thickness at the constant atomic number affects contrast.

In conventional TEM, contrast has two contributions namely amplitude contrast and phase contrast which both strongly influenced by the sample characteristics. Amplitude contrast arises from the mass and/or thickness variations in a specimen since it alters the electron-matter interactions (differential absorption of electrons in the specimen). Therefore, amplitude contrast is often attributed to mass-thickness contrast, which is the main and sometimes the only contrast obtained from biological specimens. For high atomic number or thick specimens, low-angle Bragg scattering is usually negligible, instead the image is constructed by high angle scattered beams (> 5º) at low intensity, and hence the intensity of the scattering depends on atomic number of the specimen atoms, also called Z-contrast (incoherent imaging). Mass-thickness contrast is

also related with electron energy and lens-aperture settings of the microscope. Lower energy electrons and smaller objective apertures lead to a better contrast. However low energy electrons require even thinner samples to reduce absorption and chromatic aberrations originated from the sample. Therefore, one should find the optimum conditions within sample preparation and imaging parameters to achieve the best resolution-contrast balance for a particular specimen.

Phase contrast arises from the interference of the waves scattered from a specimen with the unscattered waves. Depending on variations in material characteristics in terms of thickness, composition or lattice defects, electrons undergo a phase shift when scattering from a specimen. The interference between these differential phases generates phase contrast images. However, in general, electrons undergo a small phase shift upon scattering from specimens composed of low atomic number elements, which results weak or no phase contrast. Phase shift increases with increasing atomic number and it generally decreases with increasing electron energy.[26] An emerging technology to enhance the phase contrast involves using phase plates, which are basically ultra-thin films with a central aperture, positioned in the back focal plane of the objective lens of the microscope. This aperture is centered in the optical axis, so unscattered electrons pass through without scattering. Scattered electrons from a specimen pass through the film in the outer region of the central aperture, which results in a delay in their phase. The interference between the scattered and unscattered beams results in phase contrast in the acquired images. The amount of phase delay depends on the electron wavelength ($\lambda$) at a certain energy ($U_0$), the film thickness ($t$), and the inner potential of the material ($V$), which is represented by:

$$\varphi = -\pi \frac{t}{\lambda} \frac{V}{U_0} \frac{1 + 2\alpha U_0}{1 + \alpha U_0}. \qquad\qquad (3.15)^{[27]}$$

where $\alpha$ is a constant ($9.8 \times 10^{-6}$ V$^{-1}$).

Although it was shown that phase plate significantly enhance the contrast for biological specimens, they are typically very thin and delicate, also have some major limitations such as short life span and  lack of hardware and software support for automated data acquisition.[27–29]

### 3.3.5.  Electron Beam Damage

The inelastic collisions between electrons and specimen atoms cause electron beam induced damage on the specimen. Despite the fact that it is heavily based on electron energy and the radiation tolerance of the specimen, in principle any sample can be damaged to certain extent with TEM. Beam induced damage can be divided into three forms: radiolysis, knock-on damage

and heating. Radiolysis changes the chemistry of the specimen by breaking chemical bonds or causes ionization. Knock-on damage can be attributed to high energy electrons; it causes displacements of the specimen atoms and generates local defects. If the electron energy is high enough, it might eject the atoms from the specimen, which is called *sputtering*. Heating is caused by phonons and it is the most severe one for biological samples since their thermal conduction is poor. Inelastic events (energy transfer) are more frequent at low electron energies thus radiolysis becomes more dominant in the specimen. As electron energy increases, radiolysis is decreased; on the contrary knock-on damage is increased.

In this thesis, all the samples studied in TEM have polymer structures, so they are more sensitive to damage occurs by radiolysis and heating. There are several ways to minimize the damage on biostructures such as operating TEM at low dose, cooling the specimen during the imaging and coating the specimen with conducting film. Additionally, using small apertures to reduce the electron exposed area on the specimen and pulsed electron sources instead of traditional continuous ones can reduce the damage on the specimen. *In situ* TEM allows using higher electron dose comparing to CTEM and cryo-TEM since hydrated electrons and beam generated radicals can diffuse out the beam exposed area in liquid medium more effectively.

### 3.3.6. Sample Preparation

Electron microscopy in transmission mode uses thin specimens. Here, thin means electron transparent to fall sufficient intensity onto the detector to generate an information carrying image. This requirement is strongly related with the electron energy and average atomic number of the specimen. However, in general "thinner is better" and a thickness of <100 nm is preferred in TEM studies. In extreme cases for high resolution TEM imaging, even 10 nm thick samples might be required.

A TEM is operated at high vacuum to minimize the interaction of electron beam with air molecules. This is the main constrain of studying liquid or gas phase samples, since the samples may have a low lifetime in vacuum. Therefore, TEM is traditionally used for solid samples. The most common way to prepare TEM samples in the solid state is sectioning from bulk material using a microtome, which employs fine glass or diamond blades combined with a light microscope. The sectioning process can be automated and it is possible to make even ultra-thin samples (down to 10 nm) for both conventional and cryo-TEM. Soft materials can be embedded

into resin before sectioning. Small and sufficiently thin structures can be directly deposited onto grid structures or ultra-thin continues films for support and are imaged upon solvent evaporation.

Above mentioned sample preparation methods obviously do not allow real-time observations of dynamic events. Only way to reveal structure-function relationship of chemical and biological phenomena is monitoring atoms, molecules or particles in their native environment. In-liquid TEM offers that privilege however it comes with challenges in silicon based micro-fabrication, sample preparation and often acquiring poor resolution and contrast from organic structures. In the following chapters of this thesis, we will discuss on the current microfluidic chips for in-liquid TEM, what can be achieved with them in regard to attainable resolution-contrast and suggest a novel fabrication method to achieve sub-nanometer resolution with large sampling areas.

### 3.3.7. In-Liquid Transmission Electron Microscopy

Sample preparation of inorganic compounds for conventional TEM is straightforward using microtoming, thin film deposition techniques or focused ion beam.[30–32] Organic compounds require further pre- or post-preparation steps in order to maintain their structural integrities. Cryogenic TEM has been developed based on "flash freezing" samples in liquid nitrogen. It allows imaging bacteria, viruses, tissue specimens and mammalian cells using a specialized sample holder.[33–35] It is possible to capture high-resolution still frames from a iterative procedure with TEM by using series of frozen samples in different stages of biochemical processes to protect their structural integrities during the measurement; however, one cannot fully understand structure-function relationship from static images where the intrinsic motions are lost.

Environmental scanning electron microscopy (ESEM) has the advantage of imaging surface of the organic compounds in aqueous environment while maintaining the sample close to its native state. Even though this is a remarkable advantage over conventional TEM, it requires transferring the specimen into ~4℃ water environment, which can cause dramatic changes in the sample structure and maybe also observed dynamics.[36–38]

In order to perform high resolution TEM imaging in the liquid state, the thickness of the liquid layer should match with electron elastic mean free path and the sample must be isolated from the high vacuum of TEM. Electron transparent windows have been fabricated and used for this purpose. Silicon nitride (SiN) is currently the most common material for windows due to its rigidity and straightforward processing as free standing thin film. It is now possible to image

high atomic number materials such as metallic nanoparticles in solution with nanometer spatial resolution.[39–49] However, resolving soft materials in solution is a greater challenge due to weak electron scattering from low Z material.[50] This challenge is more pronounced for biomolecules due to their low tolerance to radiation damage.[51–53]

The current approaches for TEM studies in liquid phase involve 1) trapping the liquid specimen between two transparent windows based on hermetic sealing, 2) using a cell with again ultra-thin windows and flow capability allowing *in situ* sample exchange and 3) using single or multiple graphene layers to encapsulate the sample to isolate it from the high vacuum. Each approach has its own advantages and shortcomings comparing to other methods. A static liquid cell is simple to use and a few μL volume of sample is sufficient for a measurement, which is a major advantage for precious samples. However, having tiny volume of sample in the chamber might result in acquiring insufficient information, hence requires sample exchange multiple times.[46,48] On the other hand, flow cells allow *in situ* sample exchange but it is difficult to control pressure fluctuations in the flow system, which directly affects the stability of the windows during a measurement. Furthermore, depending on the inner diameter and the length of used tubing, generally large sample volume is necessary to flow the sample into the viewing area.[36,45,49] Graphene liquid cells currently can provide higher spatial resolution compared to SiN based liquid cells by trapping a small volume of liquid between two graphene sheets, however it suffers severely from drying out the liquid sample quickly after first electron exposure.[54–58] As seen, there is lack of universal solution to above mentioned problems; hence one should choose the experimental setup according to sample requirements.

## 3.4.    Introduction to Scattering and Diffraction of Electrons

In this chapter, we will be discussing some of the fundamental terms regarding scattering and diffraction. When waves are scattered from an atomic plane (a specimen), if the distance between the adjacent scattering centers corresponds to an integer multiple of wavelength, these waves remain in phase and can interfere constructively. It was von Laue, who first predicted the interference of waves scattered from crystal planes for the case of X-rays. Figure 3.6 depicts this phenomenon, where $\theta_1$ is the angle of incidence between the two atoms indicated by purple spheres in Figure 3.6 and the incoming wave and $\theta_2$ is the one between the same atoms and the

diffracting wave. Then the shortest distance between the scattering centers, *a*, is defined by simple trigonometry:

$$a(\cos\theta_1 - \cos\theta_2) = h\lambda.$$

(3.16)

If we rewrite Eq. 3.16 for three dimensional space, we have *b* and *c* additional to *a* as the distances between scattering centers and consequently different scattering angles and integers (*h, k, l*). The letters *hkl* are known as the Miller indices and correspond to the indices of diffracted beam from a crystalline plane. In other words, plane (*hkl*) cuts a, b and c axes at 1/h, 1/k and 1/l, respectively, as reciprocal lattice vectors. These lattice parameters represent the unit cell of a crystal, which is the smallest repeating unit in the crystal representing its overall structure.
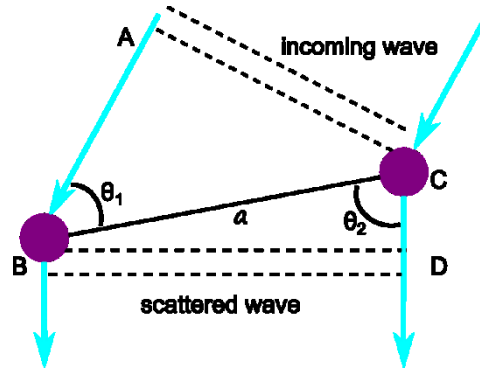


Figure 3.6. Schematic illustration of the von Laue approach to calculate the path difference for a wave scattering from two atoms within a distance *a*.

If we consider waves scattering from multiple adjacent planes, the distance between these planes should equal an integer multiple of wavelengths so the waves remain in phase upon scattering, which is known as Braggs' law. Figure 3.7 shows the description of the scattering of incoming waves from atomic planes of spacing *d* and with an angle of *θ*. As seen in the figure, the distances AB and BC are equal and the distance between the adjacent planes are represented by:

$$n\lambda = 2d\sin\theta_B,$$

(3.17)

where *λ* is the wavelength of the waves. The term *n* in Eq. 3.17 indicates that waves are scattering from multiple planes with spacing *d/n*.
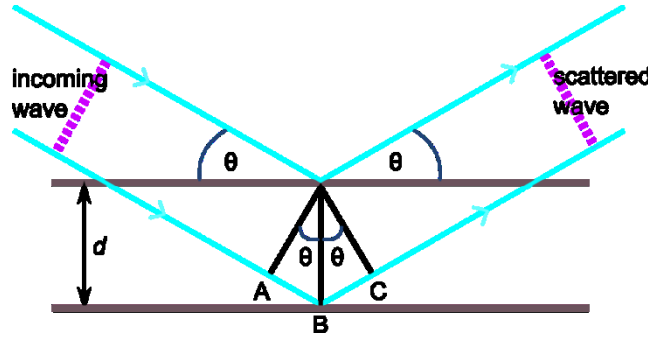
Figure 3.7. Reflection of waves from two adjacent atomic planes with a spacing of $d$. The path difference between the reflected waves is AB+BC.

Given that all Laue conditions are satisfied in three dimensions, we can expect a diffraction pattern form electrons also in the TEM.

The atomic positions of a specimen, either crystalline or amorphous, can be related the amplitude scattered by regularly arranged atoms in its structure, which is the sum of the scattering from all the $i$ atoms ($x_i$, $y_i$ and $z_i$ are the atomic coordinates) in the unit cell. If the specimen is crystalline, the structure factor $F(\theta)$ is given by:

$$F(\theta) = \sum_{i}^{\infty} f_i e^{2\pi i (hx_i + ky_i + lz_i)} \tag{3.18}$$

where $hkl$ are the Miller indices for the unit cell, $\theta$ is the scattering angle. As seen from Eq. 3.18, the atomic coordinates are multiplied with a phase factor of $2\pi$ to include the scattering from different but on parallel atomic planes, which causes a phase difference. The scattering factor is related with the type and position of the atom and specific crystalline planes that build up the whole structure.

The term $f$ in Eq. 3.18 represents the atomic scattering factor from isolated atoms, which is usually defined for electrons as:

$$f(\theta) = \frac{\left(1 + \frac{E_0}{m_0 c^2}\right)}{8\pi^2 a_0} \left(\frac{\lambda}{\sin\frac{\theta}{2}}\right)^2 (Z - f_x) \tag{3.19}[7]$$

where $E_0$, $m_0$, $c$ and $a_0$ are electron energy, electron mass, speed of light and the Bohr radius, respectively. The term $f_x$ represents the scattering factor for X-rays.

In amorphous samples, liquids and gases, the atoms and molecules are arranged almost randomly. However, one can still find a characteristic length scale in the interatomic and intermolecular distance. Hence the scattering intensity renders this structure as stronger intensities at certain angles, and as result we obtain diffuse rings in the diffraction pattern.

## 3.5. Micro- and Nanofabrication

In this chapter, basic micro-nanofabrication techniques and their applications to this thesis will be discussed. Using these techniques, the 'Nanofluidic cell' was previously manufactured in Miller Group and the detailed information about its fabrication and use for electron microscopy was given in the thesis of Maher Harb and Christina Mueller. Therefore, the sections related to the previous design will be kept brief while including some later modifications applied. The use of nanofluidic cell without flow for precious samples and mammalian cells will be discussed in detail. The reinforced windows composed of multiple hexagonal silicon nitride films were designed and fabricated in the course of this thesis. The novel fabrication sequence of these devices will be explained in detail.

The ultimate goal of transferring a honeycomb pattern onto silicon nitride film is to increase the overall size of the aperture for probing electrons in diffraction experiments and to be able to image wider structures such as live cells with transmission electron microscopy, while keeping the deflection of SiN film in vacuum tolerable for the electron energy in 100-200 keV range.

### 3.5.1. Introduction to Micro- and Nanofabrication

Silicon is the most common material in worldwide for processing semiconductor devices due to its abundance, low cost and the ability of being incorporated into integrated circuits. Single crystalline silicon wafers are heavily used in most of the fabrication processes of MEMS (micro-electromechanical systems) devices. In this thesis, all the micro/nano fabrication processes involve single crystalline silicon wafers.

Specifications of a silicon wafer are determined based on its size, thickness, doping material and level, crystal orientation, resistivity and polishing. These parameters can be chosen depending on the requirements of the fabrication process.

In the following sections, regarding the techniques used in the overall work, thin-film deposition methods, photolithography, dry and wet etching and wafer bonding will be briefly discussed.

### 3.5.2. Thin-Film Deposition

Thin film deposition techniques can be given under two major sub-titles: Physical vapor deposition (PVD) and chemical vapor deposition (CVD).

In most of the PVD processes, the coating vapor is first produced from the source material, then this vapor is transferred onto the substrate and finally the vapor is condensed on the surface of the substrate. Thermal evaporation and sputtering are the most common examples of PVD. Sputtering is more preferred than evaporation because a wider range of materials can be used as target and also it provides a better adhesion to the substrate. During sputtering, the target, which is at negative potential, is bombarded with positive argon ions (in general), which creates plasma in the vacuum. The ejected atoms from the target material due to ionic bombardment deposit onto the substrate placed on the anode. In this work, silicon oxide (SiO) as the spacer material for the liquid cell is deposited on silicon substrates by sputtering.[59,60]

On the other hand, in CVD, chemical reaction is carried generally on a heated substrate to form intended film. The precursor gases diffuse convectively and adsorb onto the substrate surface. The reaction between precursors results the formation of a continuous film on the substrate. In this thesis, SiN thin films (unknown stoichiometry) used as transparent window material for electrons and also as hard mask for chemical etching, is manufactured with CVD. Therefore, the quality of the thin film, which directly affects the mechanical stability of the windows during the experiments and the masking in the fabrication process, is crucial. The pressure and temperature used in the deposition process define the specifications of the film. For a high quality of silicon nitride film (uniformity is better than 5%), low pressure CVD (LPCVD) is used. In a standard LPCVD process, the operating pressure, temperature and gas flow rates range from 0.25-2 Torr, 300-900 ℃ and 100-1000 sccm, respectively. A conventional coating of silicon nitride on silicon with reaction of silane and ammonia at around 800 ℃ is given by: $3SiH_4 + 4NH_3 \rightarrow Si_3N_4 + 12HF$. However, CVD method results generally non-stoichiometric nitride ($Si_xN_y$).[61,62]

### 3.5.3. Photolithography

Lithography can be simply defined as transferring patterns from masks onto thin films or thick substrates. The resolution and the minimum feature size that can be transferred are based on the type of the illumination source. For micron size features, UV- photolithography is widely used for high throughput production in IC (integrated circuit) industry. For finer structures, electron beam or X-ray lithography can be used.

In shadow printing, which involves *contact and proximity printing*, the critical dimension (minimal feature size, a measure of resolution) can be theoretically approximated by:

$$R = k\sqrt{\lambda\left(s + \frac{z}{2}\right)},$$ 
(3.20)

where $R$ is the minimum transferable dimension in the photomask (resolution), $k$ is a constant which equals to ~1.5, $z$ is photoresist thickness, $s$ is the gap between photoresist and the mask and $\lambda$ is wavelength of the exposing radiation. By this equation, using standard ~2 µm resist thickness and deep UV illumination source (~250 nm), contact printing (zero gap between the mask and the photoresist) gives a resolution of ~0.75 µm. In a more advanced method called *projection printing*, objective lens(es) are placed between the mask and the wafer. The diffracted light waves from the mask features are focused on the photoresist. Here, the resolution depends on numerical aperture of lens system and also the resist specifications.

Before applying a lithography step, the surface of the substrate is coated (e.g. spin coating) with polymer based resists. There are two types of photoresists based on the chemical change that they undergo during the exposure. If the resist weakens upon the photochemical reaction during exposure, and the exposed parts become more soluble in developing solutions, this type of resist is called *positive* resist. If resist becomes stronger upon illumination due to cross-linkage occurring in polymer structure and becomes less soluble, it is called *negative* resist. A spinning vacuum chuck holds substrate while resist is dispensed on. After spin coating, resist still contains up to 15% of solvent which can be evaporated either by heating it on a vacuum hot plate or in a convection oven. The resulting thickness of the resist depends on spin speed, solution concentration and viscosity. In *development* process, the unpolymerized fraction of the resist dissolves in the solution and thus the latest pattern is transferred onto the resist and also to the substrate.

*Mask* used in photolithography is a glass or quartz material transparent to near/deep UV coated with an absorbent metallic layer (e.g. chromium). This metallic layer contains the pattern

to be transferred on the substrate. Mask can be also negative or positive like resist. On a *positive* or *dark field* mask, the pattern is clear with dark background. On a *negative* or *clear field* mask, the pattern is dark with a clear background.

The proximity between mask and substrate also affects the resolution of the final pattern, especially if UV light is used as a divergent illumination source comparing e-beam lithography. Therefore, the masks which are in direct contact with substrate (*hard contact*) can be preferred for a higher resolution, however direct contact decreases the mask life time hence it is not preferable for large scale manufacturing.

### 3.5.4. Etching Techniques

Subsequent to the lithography and resist development, an etching step can follow to remove material from thin films and/or substrates. Etching can be divided into two categories: *Dry* and *Wet etching*. Chemical solutions are used for wet etching. On the other hand, in dry etching, substrate is not exposed to wet chemical etchants, but to gas, vapor or ion bombardment, in general etching is implemented by plasma assisted chemical reactions. However, both techniques rely on the selectivity between different layers, which is based on dramatic etch rate difference between the masking layer and etched substrate.

### 3.5.4.1. Dry Etching

A chemical reaction through reactive species at the surface or combining of chemical and physical mechanisms is the major routes of dry etching in general. In selecting a dry etching process, final etch profile of the features and the selectivity of the process must be considered carefully. In this thesis, reactive ion etching (RIE) and deep reactive ion etching (DRIE) with fluorine based gases are used to remove mainly SiN and silicon, respectively, due to their high selectivity and high etch rates resulting vertical side walls (high anisotropy).[63–65] During the process, high energy magnetic or electric fields ionize feed gases to form energetic ions, neutrals, reactive radicals…etc. and the substrate surface is exposed to bombardment of these radicals, which leads to removal of the material and formation of by-products. RIE can be used to etch a few tens of microns features with reasonable aspect ratio. Otherwise, by-products may not be removed sufficiently and accumulate in the incomplete features, which may inhibit further etching.

DRIE can compensate most of the shortcomings of RIE. It includes two different types of processes, known as Cryogenic DRIE and Bosch process. In this work, we used Bosch process to etch 100 μm deep features in silicon with vertical side walls. In Bosch process, a passivating layer is generated at the feature side walls to prevent further etching while the bottom part of the features is exposed to ion bombardment. These short, passivation-etching cycles result highly anisotropic etching profile for deep features with high aspect ratios of 20-30:1. This process is schematically depicted in Figure 3.8. For advanced silicon etched (ASE), high density plasma system switches between sequential passivation (~10 nm thick fluorocarbon deposits) and etching ($SF_x^+$ ions remove the passivation layer and substrate underneath at the bottom) steps. Even though some scalloping near the top of the trenches, large variation in the etch rate throughout the wafer area or feature broadening might be observed, side walls shows excellent surface planarity with a roughness of <50 nm in general.[63]
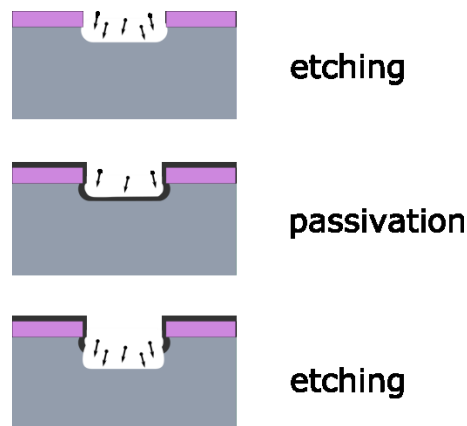


Figure 3.8. Schematic illustration of the Bosch process.

### 3.5.4.2. Wet Etching

Wet bulk micromachining is a technique to generate isotropic or anisotropic features in single crystal substrates by immersing it in alkaline or acidic solutions. The 3D etch profile of the features are defined by the orientation dependency of the etch rate. If the substrate is single crystalline silicon, the dramatic difference in etch rates on different crystalline planes results the anisotropy. Silicon atoms are packed heavily in (111) plane, which leads to the slowest etch rate. On the other hand, the etch rate is a few microns per min in (100) plane (depending on solution

type/concentration and temperature), which is orders of magnitude higher than that in (111) plane. This leads to a very specific and reproducible etching profile with an angle of 54,7° between (100) and (111) planes, which is illustrated for Si<100> substrate in Figure 3.9. One can use Equation 3.21 to calculate the relation between the area of the opening in the masking layer and the resulting dimensions of the pit at the bottom with known wafer thickness, $d$. In this thesis, solution of potassium hydroxide (KOH) is used to etch Si<100> with LPCVD nitride as masking layer (the etch rate of KOH in SiN is negligible (<1nm/h)).

$$y = x - \frac{2d}{\tan 54.7} \tag{3.21}$$

In this work, we also used concentrated hydrofluoric acid to etch glass wafers for fabrication of reinforced windows and buffered oxide etching (BOE, a mixture of ammonium fluoride and hydrofluoric acid) to pattern silicon oxide films. They both result isotropic etching profiles.
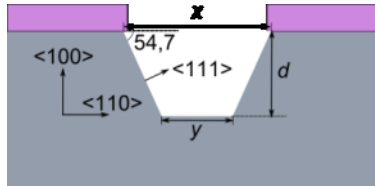


Figure 3.9. Etching profile of Si<100> in alkaline solutions.

# 4. Aim of the Study: Making Molecular Movies

The term "Molecular Movie" refers to capturing atomic/molecular motions "live on air". For this highly challenging task, one needs a "super" camera with sufficient shutter speed to catch fast motions and a bright illumination source to resolve atoms. More specifically, shutter speed of the camera must match with the speed of atomic motions. For the sake of simplicity, we consider a bond displacement of 1 Å and atoms moving with the speed of sound, the time between the onset of the process to the no-return point is approximately 100 fs. This time scale coincides with the one suggested by Arrhenius theory for unimolecular motions.[1,2] Despite there are higher frequency motions with smaller displacements (intramolecular motions or molecular vibrations, e.g. OH stretch in liquid water), these motions are generally small amplitude and not over chemically relevant length scales. Therefore, we can define 100 fs as the needed shutter speed to resolve key motions in a chemical reaction. The second challenge is the illumination requirement. A probing source, which possess wavelengths shorter than the interatomic spacing is required. In this case, X-rays and high energy electrons are the two and only candidates to be used. In either case the intensity of the probing beam must be sufficient for image quality in terms of contrast.

After dealing with the issues regarding illumination source and effective camera shutter speed, one come across with the concept of signal-to-noise ratio. Random transition between one stable state of matter to another is a very infrequent event. Hence, one has to induce the transition by perturbing a certain minimum portion of the target atoms to be able to detect the outcome and convert it into measurable signal. Heat is one of the common perturbative elements to increase the rate constant of a chemical reaction. Another approach involves using a laser to excite the sample to an excited-state and trigger the dynamics. Today's femtosecond laser technology not only offers very short pulses to excite the sample, it also makes femtosecond time domain accessible using cameras with slow shutter speed. Here, the excitation pulse triggers a change in the sample, and this change is probed at a well-defined time point upon excitation. Therefore, the limiting factor here is not the shutter speed of the camera alone; it is the pulse duration of the excitation-probe beam.

Sample preparation is one of the major limiting factors in regard to achievable resolution in both imaging and diffraction with electrons. This limitation can be overcome for crystalline forms of solid specimens by traditional methods. However life is mostly governed by chemical

reactions in solution. To understand chemistry and hence biology, one has to look into solution phase and monitor reaction dynamics in their natural environments. This is a greater challenge compared to experiments conducted in solid phase especially if the probing element is electrons. In regard to sample specifications for electrons, the sample should obey the general law of "Thinner is better" in electron diffraction and ideally has a large area (more specifically, the viewing area should match with the specimen size and also the size of the electron beam). This requires (with ballpark numbers) a liquid film with an ideal thickness of maximum a few hundreds of nanometers, an area of ideally minimum 50-100 $\mu m^2$ and stable in high vacuum. In this thesis study, a great deal of work has devoted to achieve this ideal liquid film thickness in vacuum using modern nanofabrication techniques and micro-nanofluidic approaches.

# 5.    Nanofabrication: Meeting the Challenges

## 5.1.    Nanofluidics for Imaging with Electron Sources

The first nanofluidic cell design was reported in the thesis of Maher Harb in Miller group, and it was presented as a promising tool to investigate structural dynamics occurring in atomic scale in liquid phase using electrons. The first design featured 40 nm thick silicon nitride windows and 100 nm thick silicon oxide spacer in order to match with (or getting close to) the mean free path of high energy electrons in liquid sample. First sample used in liquid phase electron diffraction experiments in Miller group is diiodomethane ($CH_2I_2$) to possibly acquire diffraction signal from iodine. However, this attempt resulted unsuccessfully probably due to the outward bowing of ultra-thin SiN windows as a result of the pressure difference between the inside of the cell and the vacuum chamber and additional internal pressure of the microfluidic setup.

Christina Mueller accomplished to scale the lateral dimensions of SiN windows and the spacer thickness down to 100x50 μm and 45 nm, respectively, and also adapted the outer dimensions of the nanocell for conventional TEM.[66] This design was combined with an *active feedback loop* to prevent the minor fluctuations in liquid layer thickness during *in situ* measurements. Despite the fact that the latest concept does not help the ultimate bulging problem of SiN windows and obstruct a continuous flow during a measurement, nanometer spatial resolution is achieved from gold and polymer nanoparticles in solution using STEM.[49]

Among other efforts in this thesis, the SiN windows were aimed to be reinforced with a *honeycomb* pattern. Using multiple, relatively small, hexagon shaped SiN windows with thin bars in between has three major advantages: First, hexagon windows with low stress LPCVD SiN ($a =$ 5.8 μm) theoretically exhibit only ~80 nm deflection in the center in high vacuum, which is a factor of 15 less than that of 100x50 μm windows with the same SiN specifications. This leads to ~160-260 nm liquid sample thickness (assumed spacer thickness is <100nm), which is perfectly suitable for electrons at >100 keV scale.[1] Second, they are more mechanically stable than the large rectangular windows, thus they might be less sensitive to pressure fluctuations in the flow system. Consequently, one can flow sample continuously during a measurement, which is a remarkable advantage for studying on nonreversible systems. Third, the overall window size can be increased up to 1 mm; having a large viewing area is very important for imaging large

structures such as live cells with TEM, and capturing more electrons of the beam, whose size can be larger than a few hundreds of microns for some electron gun setups.

In the followings sections, the microfabrication sequence of the current generation nanofluidic cells will be briefly discussed. The fabrication of honeycomb patterned windows will be given in detail.

## 5.2.    Fabrication of the Nanofluidic Cell

Compared to the previous design for TEM, the outer dimensions were set to 8x4 mm for a JEOL electron microscope, and eight different window sizes were introduced on the same photomask. The windows (50 nm thick) have lateral dimensions of 200x50, 200x30, 200x10, 100x50, 100x30, 100x10, 50x50 and 30x30 μm. Large windows were intended to use for *in situ* live cell imaging and small ones for imaging the dynamics of organic and inorganic nanomaterials in solution. Note that these dimensions correspond to the ones imprinted on the photomask; the actual features in the final product can show slight variations.

Figure 5.1 shows the fabrication steps of the nanofluidic cell for electron diffraction and microscopy. The fabrication is based on anisotropic etching of LPCVD SiN deposited single crystalline silicon wafers in hot KOH. UV-photolithography is used for pattern transfer and reactive ion etching is used for SiN removal. The remaining SiN film is used as a hard mask for KOH etching and free-standing 50 nm thick SiN windows and openings for the liquid flow are obtained. For the spacer, a 100-500 nm silicon oxide film is sputtered on the top half and patterned as a rectangular nano-channel with following standard lithography steps and buffered oxide etch. The robustness of the sputtered oxide is found to be comparable with PECVD (plasma enhanced CVD) oxide since the etching time of both films with the same thickness in BOE is similar. This channel is overlapped with 150-200 μm deep reservoirs (trenches). These reservoirs reduce the high flow resistance area and allow flowing the sample in ~50 nm thick channels with a reasonable internal pressure. This is obviously not a trivial task, considering such minute dimensions and SiN film as a hydrophobic material. Therefore, nanocell parts need vigorous cleaning to remove particles and surface treatment to increase the wettability. The cell parts are cleaned with a mixture of sulfuric acid and hydrogen peroxide at 80 ºC for 30 min (piranha solution). This solution oxidizes organic contaminants on the cell surface and also leaves it hydrophilic, which is crucial for wetting the windows effectively in sample loading. Figure 5.2 illustrates the flow setup for TEM imaging or e-diff experiments. In the figure, a liquid transfer

arm for TEM is illustrated. Different sample holders can be designed with the same principle and used in custom made electron sources. Also note that windows are positioned perpendicularly in the top and bottom wafers to ease the alignment.

The microfluidic setup for the cell requires a minimum of 0.5-1 mL sample volume for *in situ* flow. This amount can be difficult to obtain for precious samples such as DNA/RNA oligonucleotides or some proteins especially since the concentration should not be low. However, the nanocell can be also used without flow function by using only top parts of the cell; hence a volume of 1-3 μL sample solution is loaded in between two top parts of the cell and the sample cell is sealed with soft O-rings in the liquid specimen holder.
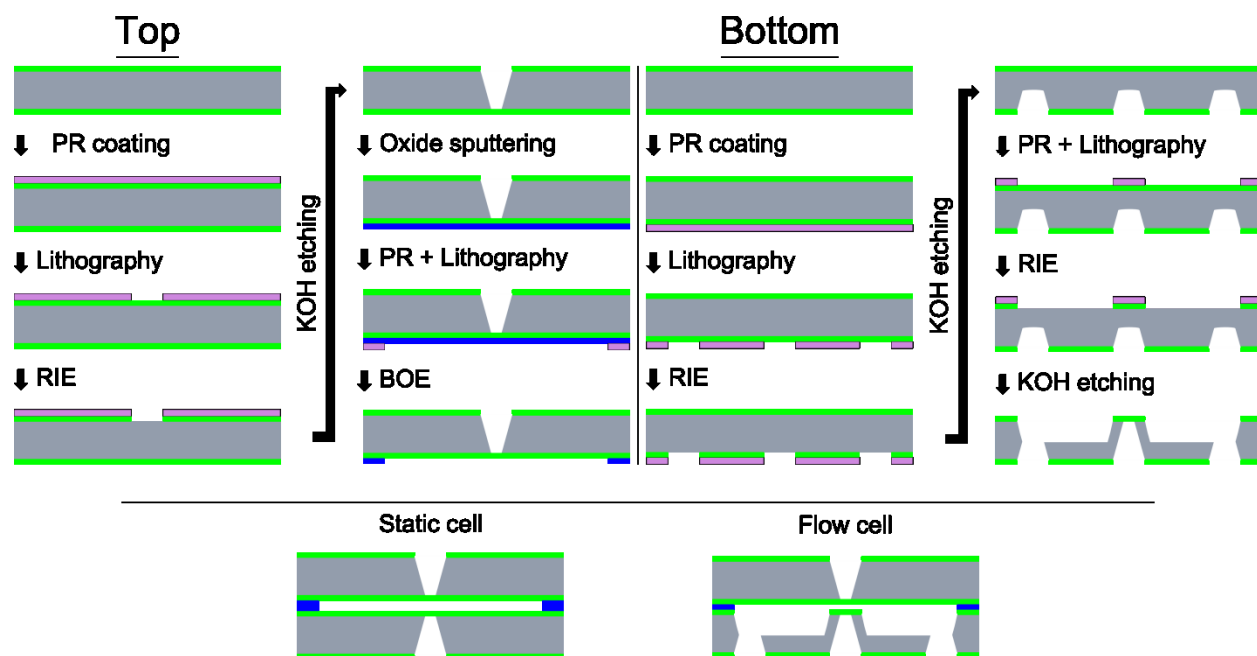


Figure 5.1. Fabrication steps of the nanofluidic cell. Color coded as follows: Gray is silicon, blue is silicon oxide, green is silicon nitride, and pink is photoresist (PR).

36
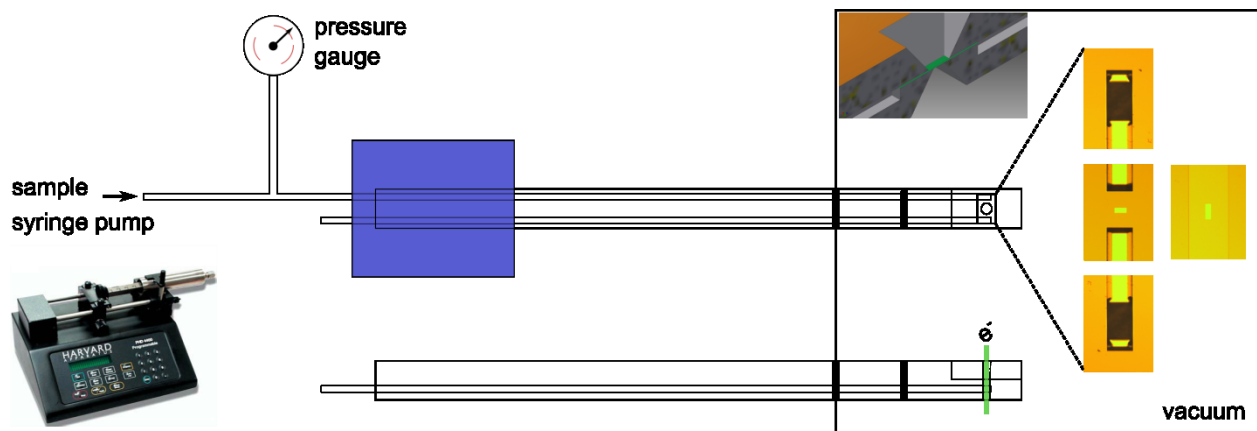
Figure 5.2. Nanofluidic setup for TEM imaging and e-diff. The sample is introduced into the viewing area by pressure driven flow and pressure is continuously monitored during the experiment. In the right panel, the 3D cross sectional view and the light microscopy images of the halves of the nanofluidic cell are shown (not drawn to scale).

### 5. 3.    Mechanical Stability of the SiN Windows under Uniform Pressure

We investigated the behavior of SiN windows in vacuum in order to characterize the actual thickness of the liquid layer. Ultra-thin SiN windows are very sensitive to pressure differences and immediately respond by deforming. We preferred to use rectangular geometry for the SiN windows in order to ease the alignment of the halves while keeping the short edge as small as possible since the deflection mostly depends on the shorter edge.[67,68] We used 200 µm x 100 µm windows for e-diff experiments and various sizes ranging from 200 µm x 50 µm to 100 µm x 10 µm for TEM measurements. It is well known that smaller dimensions are more stable in vacuum and result in smaller deflections. Since the electron beam can be collimated down to a few µm spot in TEM with high number of electrons, we chose the smallest dimension possible for windows. However, windows smaller than 10-20 µm in short edge can be difficult to align and also lead to a very small probing area during the measurement. In contrast to commercial TEMs, custom designed electron sources based on the photocathodes generate larger beams thus we chose 200 µm x 100 µm window size to match with the beam size.

In this chapter, after introducing a model on thin films to define their deflection under uniform pressure, bulging test results in vacuum for three different window sizes will be given.

The characterization of the SiN window behavior in vacuum will assist development of next generation nanofluidic chips with minimum deflection and large probing apertures.

### 5.3.1. Experimental Model

We can estimate the deflection in the center of a free standing thin film of silicon nitride using Eq. 5.1.[69,70] The deflection in the center of the membrane under a uniform pressure is given by:

$$P = \frac{ct\sigma_0}{a^2}h + \frac{8Et}{6a^4(1-v^2)}h^3 , \qquad (5.1)$$

where $P$ is pressure (Pascal), $h$ is maximum deflection in the window's center, $t$ and $a$ are the thickness and the half length of the window's short edge, respectively. Figure 5.3 shows the schematic diagram of the membrane for clarity. In Eq. 5.1, $E$ and $v$ are Young's modulus and Poisson's ratio of the SiN film. Young's modulus was reported as 235 GPa for low stress LPCVD method assuming a Poisson's ratio of 0.28.[69] Due to the nature of the deposition process, SiN has residual stress, $\sigma_0$, which was reported as $124 \pm 14$ MPa for square and $147 \pm 25$ MPa for rectangular membranes.[69] The deflection also depends on the geometry of the membrane, which is contributing to the first part of Eq. 5.1 as the residual stress coefficient, $c$. The residual stress coefficient as a function of membrane aspect ratio was reported as 2 for the geometry of the membranes with an aspect ratio of $\geq 2$.[69]

We found a deviation between the feature sizes on the mask and the real ones possibly due to undercut in KOH etching step. Therefore, we measured the real lateral dimensions of the windows with a light microscope before the bulge test. We found the lengths of the short edges to be 115 μm, 70 μm, and 15 μm for the targets of 100 μm, 50 μm and 10 μm, respectively. The maximum deflection in the center of a single window with a dimension of 200 μm x 115 μm was calculated to be ~3.8 μm ($P = 1$ bar) using Eq. 5.1, which corresponds to a height of ~7.7 μm in the center including the deflection in both windows and the spacer thickness (generally ~100 nm). Figure 5.4 shows the deflection in both windows of the nanocell ($2h$+spacer thickness) as a function of window short edge (A) and thickness (B). Figure 5.4 A illustrates how the total deflection is increased with larger window sizes. Figure 5.4 B shows that total deflection is decreased to less than a micrometer for 200 μm x 50 μm windows if 1 μm thick windows are used: however window thickness should be kept ≤50 nm for sufficient electron transmission in both windows.
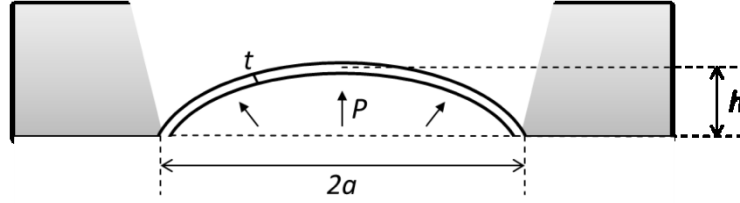
Figure 5.3. Schematic diagram of the membrane under uniform pressure

In order to determine the thickness of the liquid layer precisely, more aspects must be considered such as liquid vapor pressure and the degree of wetting. Wetting of the liquid cell can be modified by surface treatment. For example, cleaning with strong oxidants makes the windows hydrophilic, consequently increases the wetting degree. In a flow cell, the resistance of the nanometer channel and applied flow rate, which is related to the generated internal pressure, also affect the deflection of the membranes (Figure 5.1 and 5.2). Additionally, the residual stress of the SiN film depends on the deposition conditions and can show variations from batch to batch. Therefore, we decided to measure the deflection of the windows using thin-film interferometry to obtain the actual thickness of the liquid film in vacuum. We used three different window dimensions for a comparison and also to test the reliability of the method.
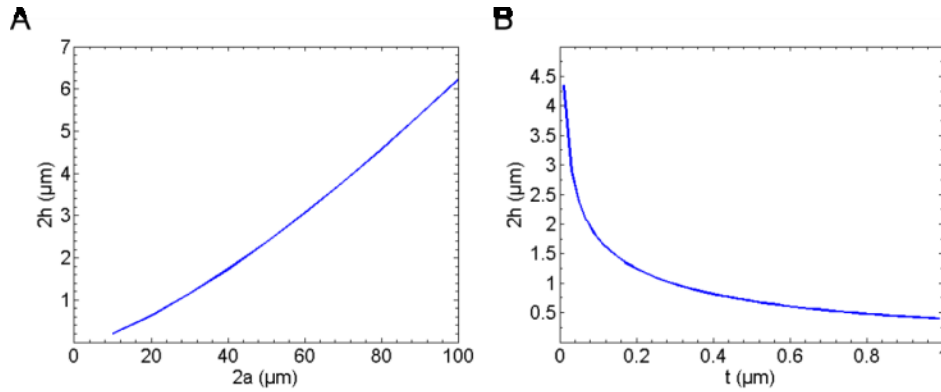


Figure 5.4. Total deflection in nanofluidic cell windows as a function of window short edge (A) and thickness (B). A window thickness of 50 nm and a short edge of 50 μm are used for the analysis shown in A and B, respectively. An aspect ratio of >2 for lateral dimensions of the windows and a pressure difference of 1 bar are used for the analysis.

### 5.3.2. Bulging Test on SiN windows

We used thin film interferometry with a 550 nm bandpass filter to observe the interference of light waves transmitted the liquid cell windows in vacuum. Due to constructive and destructive interference of light waves depending on the distance between windows, one can observe bright and dark fringes similar to Newton rings. These fringes can be used to calculate center-to-center distance between the windows.

The O-rings pressing against the silicon wafer in the mount of the liquid cell in the holder can induce a mechanical stress on the windows. If one applies inhomogeneous force on the liquid cell, the windows can deform and consequently interference fringes appear. When we evacuate the experimental chamber or apply additional pressure through the liquid cell channel with a syringe pump to flow the sample in, the number of fringes observed on the windows increase and their shape-width can also change based on the curvature of the windows. Figure 5.5 shows the illustration of the geometry, under which we observe interference (A), and the interferometry setup we used to record the window images in vacuum (B).
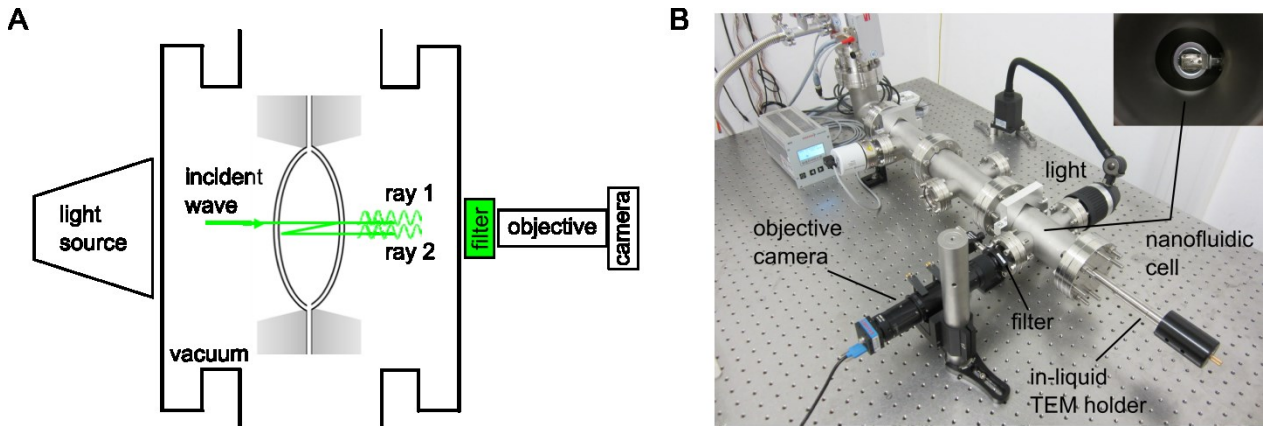


Figure 5.5. (A) Schematic illustration of the observed interference phenomenon and (B) the interferometry setup used to record window images in vacuum.

We used an LED light source with a 550 nm band-pass filter (FWHM 10±2 nm) to obtain quasi-monochromatic light. As illustrated on Figure 5.5, when the windows are illuminated, some fraction of the incident rays is transmitted (ray 1) and some fraction is reflected from top and bottom windows and then transmitted (ray 2). If ray 1 travels a distance of "d" in the thin film, ray 2 travels a distance of "3d". When the difference, 2d, corresponds to a multiple of the

wavelength of the light source, the rays interfere constructively and a bright fringe appears in the center of the window image. This is represented by:

$$2dn = m\lambda \,, \tag{5.2}$$

where $d$ is the distance between the two windows, $n$ is the refractive index of the medium, $m$ is the number of fringes and $\lambda$ is the wavelength of the light source.

First we tested the windows with a short edge of ~100 μm, which were aimed to be used in e-diff experiments. Figure 5.6 shows the interference images of the liquid cell windows at 0, 1 and 2 s after the onset of the evacuation of the chamber and the intensities at the center of the window images depending on the pressure difference, which simply counts the number of fringes. In the measurement, first the interferometry chamber was evacuated to 4 mbar and we confirmed by observing a stabilization in the fringe pattern indicating windows reach the maximum bulging. Then we slowly vented the chamber to ambient pressure while recording the interference fringes.

As seen in Figure 5.6 upper panel, the windows deform to the vacuum side as soon as the pressure in the chamber starts decreasing. In the lower panel, it is shown that the deflection is damping as a function of decreasing pressure and the windows reach maximum deflection at >4 mbar pressure difference. This suggests a low mechanical stability for 100 μm wide and 50 nm thick SiN windows in vacuum. Based on this data and using Eq. 5.2, the sample thickness of the liquid cell was calculated to be ~8.3 μm in the center, which is in good agreement with that calculated with Eq. 5.1 (7.7 μm).

Since the bulging is mostly determined by the short edge of the membrane[69], we performed the same measurements for 70 μm and 15 μm wide membranes for a comparison and also to check the reliability of the method. Figure 5.7 shows the evolution of the bulging of 70 μm wide windows as a function of decreasing vacuum pressure. As shown, it counts 17 fringes in total, which corresponds to ~4.6 μm path length for electrons in the center.
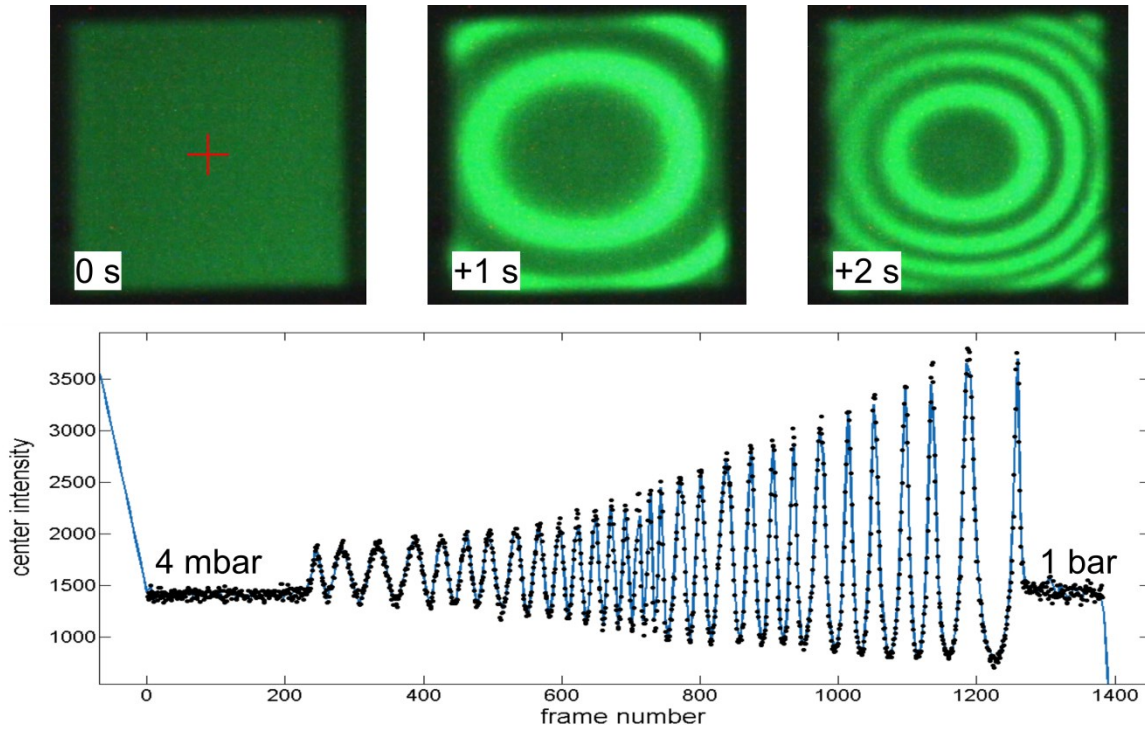
Figure 5.6. (Upper panel) Interference images of the liquid cell window at 0, 1 and 2 s after the onset of the evacuation of the chamber. (Lower panel) The intensities at the center of the windows as a function of acquired frame number. The cross in the image represents the center of the window. The window short edge and thickness are 115 μm and 50 nm, respectively (the viewing area appears as 115 μm x 115 μm because of the perpendicularly aligned windows).
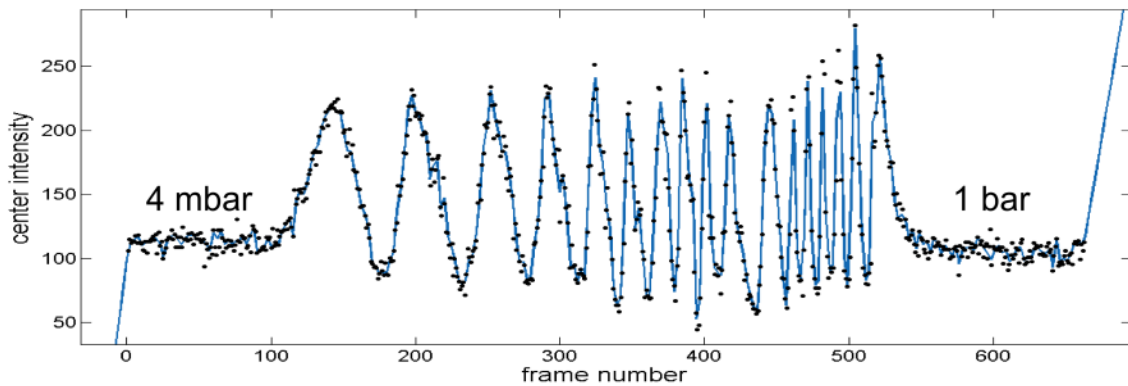


Figure 5.7. Intensities at the center of the window images as a function of acquired frame number. The window short edge and thickness are 70 μm and 50 nm, respectively.

We calculated the deflection of the SiN windows as a function of applied pressure using Eq. 5.1 and compared it with the ones found by the bulging test for three different window sizes, which is shown in Figure 5.8. As can be seen, the experimental result is in perfect agreement with the model for 15 µm wide windows, whose bulging was found to be ~0.43 µm at 1 bar pressure difference. The deviation between the values found by the model and the bulging test was found as ~0.6 µm for both 70 µm and 115 µm wide windows, which indicates good agreement.

In conclusion, 50 nm thick SiN windows with rectangular geometry and 10-20 µm short edge are found to be mechanically stable sufficiently to keep the liquid layer thickness <500 nm (addition to 100 nm thick window background). These sample specifications are relatively suitable for electron diffraction experiments at >100 keV regime. However, as discussed previously, 10-20 µm wide windows offer very small aperture size thus cut off a major fraction of the electron beam. This situation is detrimental for e-diff experiments performed by custom designed sources and also prevents TEM imaging of wide structures, mainly mammalian cells. Therefore, a serious amount of effort was dedicated to transfer a mechanically stabilizing grid pattern onto free standing SiN, which will be discussed in the following chapter.
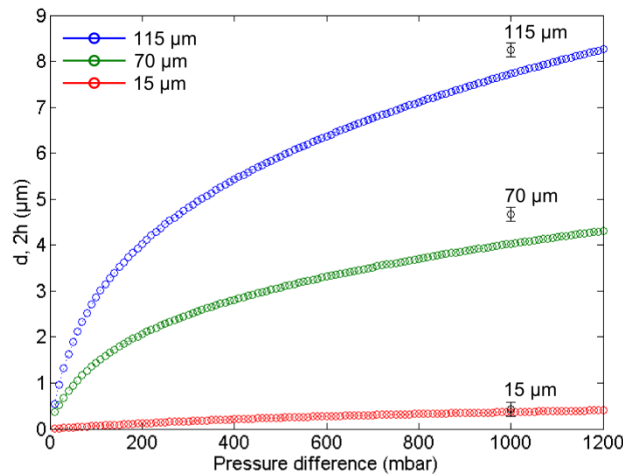


Figure 5.8. Comparison of the bulging test results with the model for 115 µm, 70 µm and 15 µm wide windows at 1 bar. Blue, green and red curves: Model; Black points: Bulging test results. Error bars represent ±10 nm deviation in the bandpass filter. Spacer thickness is included while calculating the deflection with the model.

## 5.4. Fabrication of the Reinforced Nanofluidic Cells

It was mentioned that using small multiple windows separated by bars (5-10 μm thick) rather than a single large window for the liquid cell can significantly increase the mechanical stability of the window in high vacuum. Therefore, we decided to transfer a honeycomb pattern onto the window surface. The fabrication of honeycomb liquid cells relies on the deep etching of 100 μm thick single crystalline silicon wafers. The process starts with 100 μm silicon wafers with 150 nm thermal oxide grown on both sides, then 50 nm low stress LPCVD nitride deposited on oxide for both sides. As one can imagine, 100 μm thick wafers are extremely fragile and they require extra care for handling. Therefore, they must be temporarily bonded to supportive wafers (dummy) from the very beginning of the process. We used photoresist (HPR-504, 2 μm) as glue to bond the thin wafers to dummy wafers. The thin wafers are transferred carefully on dummies and pressed on a thin wafer-dummy stack gently with a soft tool (e.g. tweezers) to remove air bubbles as much as possible. After bonding, the stack is placed on a vacuum hot plate (120 ºC) for 10 min, and then kept in the oven at 90 ºC for at least a day in order to strengthen the bond. This bonding step is very important in order to keep the thin wafers stable for the rest of the process.

Figure 5.9 shows the fabrication steps of the honeycomb patterned nanofluidic cells and cross-sectional view of the resulting structures after each step. In the process, first nitride-oxide stack is removed from one side with RIE and BOE, respectively. Deep ionic etching requires thicker photoresists comparing to that for standard RIE due to longer etching times. In an RIE step, ~2 μm thick PR (HPR-504) is sufficient for the removal of 50 nm thick SiN for about 2 min. On the other hand, DRIE takes much longer time with many repeating cycles (60-70 min). Therefore, a thicker photoresist (AZ9260) is spin-coated on the wafers with a thickness of around 10 μm. Then the honeycomb pattern is transferred onto the resist under vacuum contact with UV exposure for 6-7 min. The transferred features are etched in a Bosch process using $SF_6$ and $O_2$ plasma and $C_4F_8$ for passivation layer. This procedure should be done step by step while measuring the depth of the hexagons with a profilometer between multiple cycles. However, using a profilometer can be inconvenient for small features with high aspect ratio since the size of the probe tip is too large to reach the bottom of the features for a precise measurement. Alternatively, one can use a light microscope to observe the hexagons.

Once the silicon is completely removed from the features, a thin layer of oxide underneath appears in different colors due to well-known thin-film interference. From this point, it is risky to

continue with plasma etching since $SF_6$ based plasma does not stop etching on SiN once SiO is removed.[61] Therefore, we stop Bosch process at some level in oxide buffer layer and remove the remaining oxide with BOE, which has a very high selectivity against nitride (etch rate <1nm/min).[61] BOE has an etch rate of ~50 nm/min for oxide. However this etch rate is not valid for deep features with high aspect ratios. In our case, the features are 100 μm deep with a width of 15-25 μm. Consequently, we experienced that the wafers should be kept in BOE solution for longer times.

The formed side wall slope showed slightly reentrant profile, which could be due to relatively long etch cycles comparing to passivation cycles in DRIE[63], that results in ~5 μm widening through the bottom of the features. Figure 5.10 shows the light microscopy images of the hexagons before and after the final BOE step.

The next step is separating the thin wafers from dummies, which is performed by simply keeping the wafer stack in acetone (dissolves PR) until they come apart. Upon this step, the windows can be imaged on the front side and their final structure can be clearly seen, as shown in Figure 5.10 (right) and Figure 5.11 (right). As seen, corners of the hexagons are rounded as it goes deeper in the DRIE step. Besides the reentrant profile of the feature walls, ionic bombardment of the insulating silicon oxide results in charge accumulation and leads to further widening of the features. This phenomenon is called "notching" and very common in MEMs fabrication.[63] The cross-sectional view of the reentrant profile and notching effect is schematically depicted in Figure 5.11 (left).

After removing the dummies, the thin wafers should be bonded to a permanent support since they are too fragile to be used in the experiments on their own. For this purpose, we decided to use Pyrex glass wafers as support since it is straightforward to do anodic bonding to silicon. We used concentrated hydrofluoric acid to etch Pyrex on both sides. Pyrex wafers have polycrystalline silicon on both sides deposited in house with a thickness of around 200 nm as a hard mask for HF etching. However, an additional PR coating should be applied onto polysilicon for better masking, since the polysilicon film might have structural defects originating from the deposition process. In order to reduce the etching time, both sides of the wafers are patterned identically with UV-lithography and the polysilicon is etched with RIE all the way down to Pyrex. From this point the wafers are ready for HF etching, which takes 50 min for 500 μm Pyrex wafers. A final KOH etching step is necessary to remove the polysilicon selectively and leave plain Pyrex wafers.
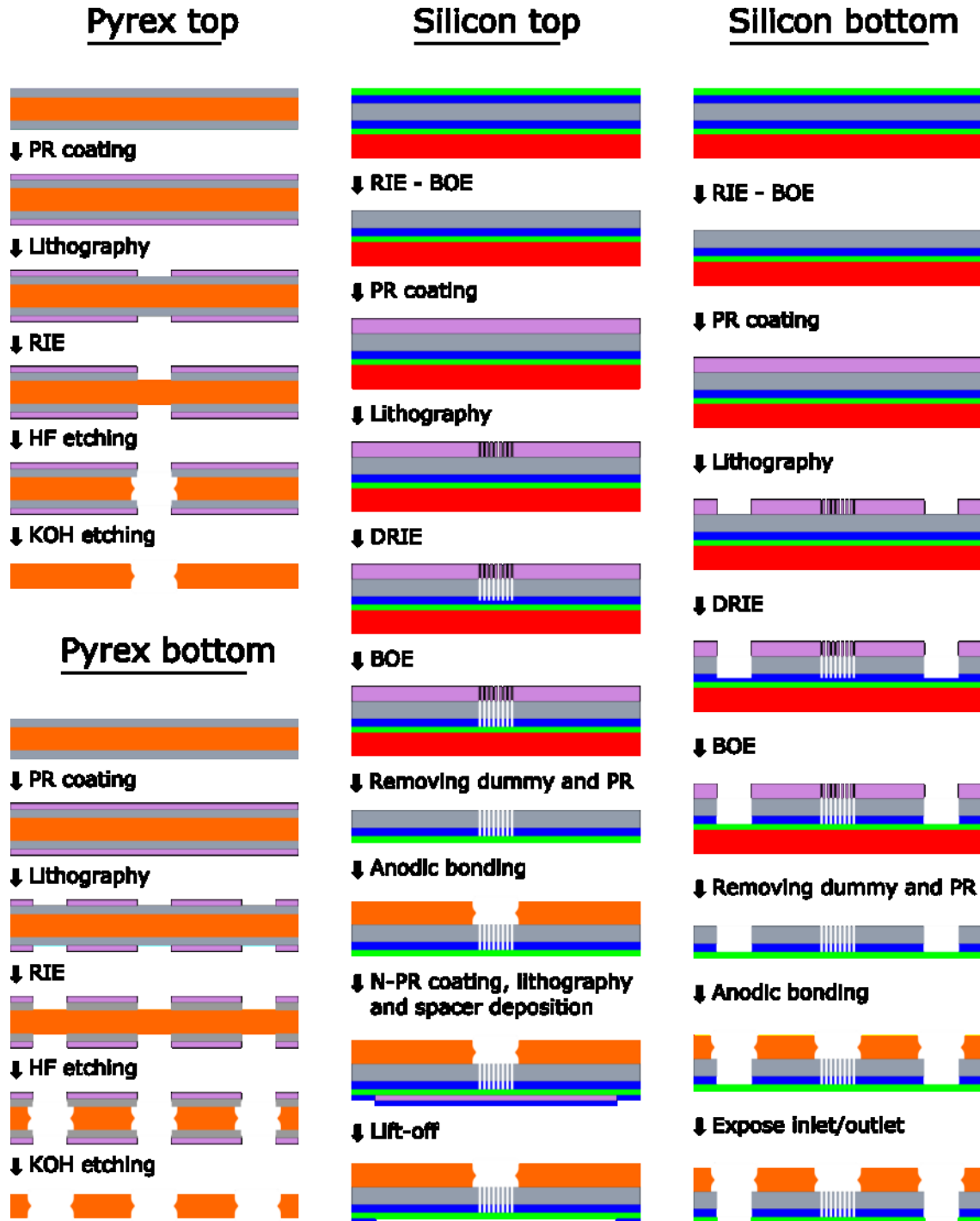
Figure 5.9. Fabrication steps of the honeycomb patterned nanofluidic cells and cross-sectional view of the resulting structures after each step. Color coded as follows: Gray is silicon, blue is silicon oxide, green is silicon nitride, red is dummy wafer (silicon), orange is Pyrex glass and pink is positive and negative photoresist.
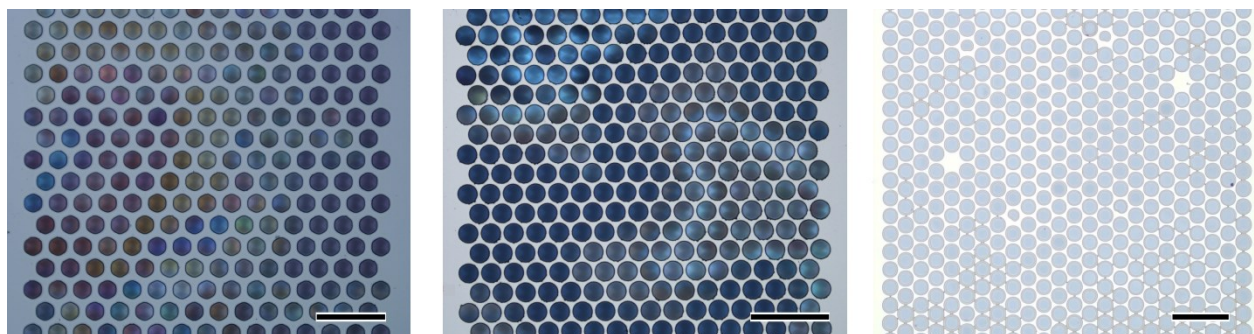
Figure 5.10. Light microscopy images of the honeycomb patterned liquid cell windows. (Left and middle) After Bosch process (190 cycles), (Right) after BOE, SiN windows are free-standing. Scale bars represent 100 μm.
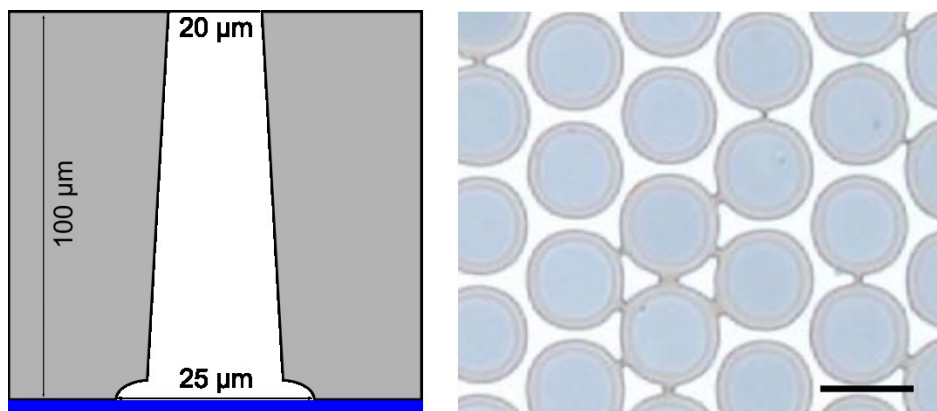


Figure 5.11. (Left) Schematic illustration of the cross-sectional view of the reentrant profile and notching effect in silicon, gray: Silicon; blue: Silicon oxide. (Right) Zoom-in image of the honeycomb windows after deep etching and BOE steps. Scale bar represents 25 μm.

Anodic bonding is a combination of a thermal and an electrostatic process, and can be performed in an equipment called "wafer bonder". Silicon is commonly used with Pyrex glass (# 7740) since their thermal expansion coefficient match well, which prevents stress forming after cooling the stack.[71] During the process, the polished silicon and glass surfaces are kept in hard contact. The stack is heated while a negative voltage is applied to the Pyrex glass. Elevated temperatures help $Na^+$ ions to become mobile in glass and increase the conductivity. $Na^+$ ions

travel to the cathode and O⁻ ions travel to the glass-silicon interface and react with silicon surface (anode) to form a Si–O bond.

After the bonding step, the SiN layer in the openings can be popped up with tweezers or another RIE can be applied to remove it. For the top parts, following another lithography step, a spacer layer is deposited onto the patterned photoresist. When the wafers are dipped into acetone, PR dissolves and a rectangular channel is achieved. This method is called "lift-off" and used as an alternative to BOE for silicon oxide spacer (At this point BOE cannot be used to pattern oxide spacer since it also attacks the buffer layer between the Si and SiN layer).

In this work, it was shown that fabrication of the reinforced SiN windows with the given method is feasible. However, the current method is suffering from low yield thus not suitable for high throughput production. It requires more work to understand the effect of residual stress in the SiN-SiO stack and a better optimization of the process parameters. Therefore, in this thesis, all the experiments are conducted using the current generation nanofluidic cells.

In the following chapters, we present our results on the dynamics of DNA attached gold nanoparticles (AuNPs), imaging of mammalian cancer cells and imaging of DNA origami structures with in-liquid TEM.

# 6. Visualization of Multimerization and Self-assembly of DNA Functionalized Gold Nanoparticles with In-liquid TEM

We previously reported the potential of using a nanofluidic cell with controllable flow for imaging with TEM.[49] Here, we preferred to use a static cell since the amount of DNA-AuNP suspension is generally too low to flow *in situ* during the measurement. The advanced design of the liquid specimen holder allows replacing the sample in minutes; hence many samples can be measured in a short amount of time. The liquid cells were pre-cleaned with piranha solution. A volume of 1 μL of sample solution is loaded in between two SiN windows. The halves of the cell were overlapped in the sample holder and sealed with soft O-rings. The liquid cell specifications and the sample preparation procedure were kept identical for all the measurements in the study. Figure 6.1 shows the schematic illustration of the liquid cell before assembly and the sample preparation procedure.
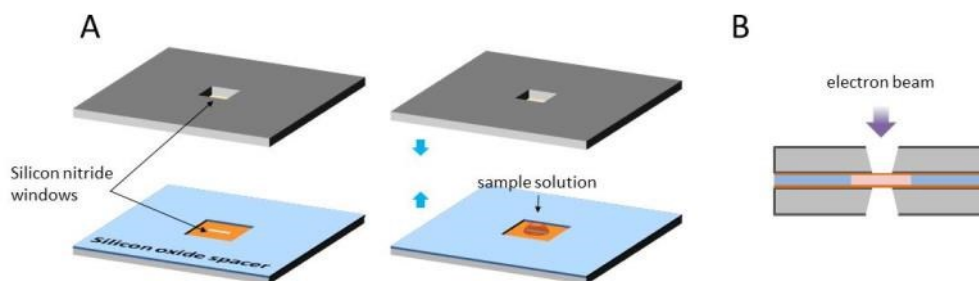


Figure 6.1. Schematic illustration of the liquid static cell. (A) The parts of the cell with one drop of (1 μL) sample solution on one of the windows. (B) Cross-sectional view of the cell after overlapping the halves. Not drawn to scale. (Taken from reference-46)

The outer dimensions of the nanocell are adapted to a custom-made liquid specimen holder for a JEOL JEM-2100 transmission electron microscope, equipped with a thermionic $LaB_6$ emitter, and a CMOS detector (TVIPS TemCam-F216). It is operated at 200 kV in bright field mode for all the measurements.

DNA attached to AuNPs is the first system studied with in-liquid TEM in this thesis. We aimed to investigate the dynamics of DNA such as folding, winding or stretching etc. in its natural environment and also the hybridization dynamics of single stranded DNA (ssDNA). DNA as an organic molecule is composed of light atoms, which leads to weak scattering of probing

electrons from its structure. Furthermore, short DNA strands have a very high diffusion coefficient in water[72], which makes them difficult to be resolved with a low camera read out speed. We were limited to 200 millisecond time resolution for this study. Therefore, we tagged DNA with AuNPs in order to locate them easily in water and visualize its dynamics indirectly.

The stability of the DNA-AuNPs and the specificity of their hybridization under aqueous conditions and electron beam exposure are very important issues for many fields of chemistry and biology in regard to using this imaging methodology; however, they have not been addressed to date. In a relevant study, Chen et al. imaged the dynamics of AuNPs linked by double-stranded DNA molecules (dsDNA) in graphene liquid cell.[54] In this work, we used a similar strategy while using ssDNA and including AuNPs with two different sizes into our experimental scheme to monitor the dynamics of DNA hybridization. Both sizes of AuNP were functionalized with one of the two different DNA oligonucleotides in multiple binding sites. The surfaces of both AuNP types were saturated with ssDNA. The DNA strands on different NPs in size are not complementary to each other. The quasi-spherical AuNPs with a core size of 17.5 ± 3.5 and 61.2 ± 8.2 nm in diameter were named DNA1-AuNP and DNA2-AuNP after coupling with DNA, respectively. DNA1-AuNPs and DNA2-AuNPs have 3′- and 5′-thiol modified ssDNA attached to their surfaces, respectively. We designed another DNA strand (Hyb-DNA) with complementary sites for both DNA1-AuNP and DNA2-AuNP to form multimers via hybridization. In order to test the specificity of the multimerization, a control DNA was designed without any complementary sites. Figure 6.2 A shows the schematic description of the formation of DNA-AuNPs multimers and Table 6.1 shows the components of each sample for clarity.

The obtained samples are plain citrate-stabilized AuNPs (no. 1), a mixture of DNA1-AuNP and DNA2-AuNPs (no. 2), DNA1-AuNP and DNA2-AuNP mixture with addition of the control DNA (no. 3), and the multimers of DNA1-AuNP and DNA2-AuNP with Hyb-DNA (no. 4). We performed statistical analysis on in-liquid TEM images of these samples to quantify the specificity of the multimerization with complementary units in sample no. 4. We acquired at least three data sets per sample in three separately loaded nanofluidic cells to increase statistical reliability and test reproducibility. The statistical data was collected from minimum 30 TEM frames per liquid cell within the 100 x 15 μm viewing area.

Figure 6.2 B shows the typical TEM images of each sample considered. It is well-known that citrate stabilized AuNPs are negatively charged due to the citrate ions on their surfaces.[73] As seen in Figure 6.2 B (no. 1), they locate in the solution separately without showing any

multimerization due to the repulsive electrostatic forces between them. We observed only a small number of multimers in the sample of DNA-AuNPs without hybridizing DNA strand (no. 2) and with control DNA (no. 3). Observed multimers in sample no. 2 and 3 suggest that some interaction between DNA strands and AuNP surface can still occur possibly due to the flexibility of the DNA shell within the liquid.[74] We observed the highest number of multimers in sample no.4 with both types of functionalized AuNPs and Hyb-DNA, as shown in Figure 6.1 C. Each frame obtained from sample no. 4 typically involves 2-3 large multimers. We performed a t-test to determine the level of difference between no. 4 and the control samples and found that p values for each control sample are dramatically lower than the significance level of the test ($\alpha$ = 0.05), which indicates the significant difference of sample no. 4 from all other control samples. This clearly suggests that multimerization of DNA-AuNPs is a result of DNA hybridization and not based on random aggregation of unstable AuNPs.
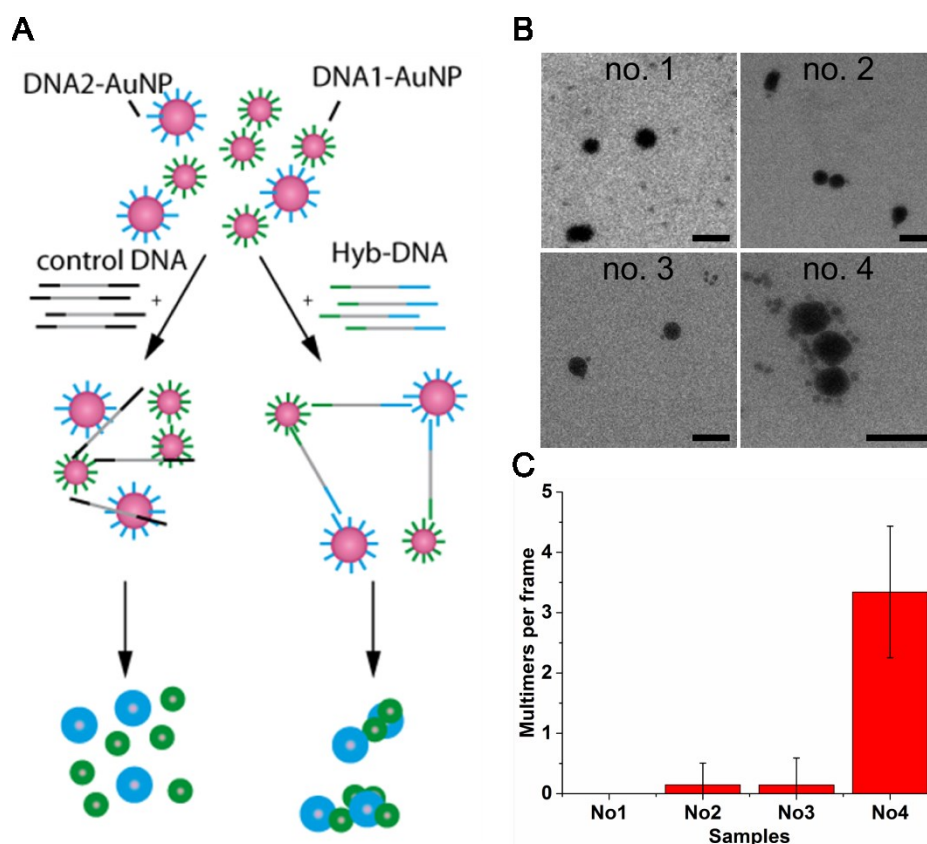


Figure 6.2. DNA-AuNP multimerization. (A) Schematic overview of the hybridization of DNA coated gold nanoparticles DNA1- and DNA2-AuNPs using a hybridizing DNA strand (Hyb-DNA). Lengths of DNA strands are not drawn to scale. (B) In-liquid TEM images of different samples. Images were taken with an electron dose of 15 $e^-\cdot nm^{-2}$, and an exposure time of 2 s.

The scale bar for each TEM image represents 100 nm. (C) Histogram shows the average number of multimers observed per TEM frame. The error bars represent standard deviation (frame-to-frame variability). (Adapted from reference-46)

The total length of a dimer including both DNA1- and DNA2-AuNP hybridized by the linker is ~120 nm. After hybridization, there is a single-stranded section of 39 nucleotides (nt) as spacer between the hybridized sections flanked by the two 21 nt long double-stranded areas and spacer sections for AuNP attachment. Table 6.2 shows the sequences of the DNA oligonucleotides used in the study. Highlighted parts are complementary sections between DNA1 and Hyb-DNA, underlined parts are complementary sections of DNA2 and Hyb-DNA. Based on the length of 340 pm per base pair and a total DNA length of 116 nt between two AuNP surfaces, the calculated distance is 39 nm when the linker DNA is in fully stretched state. Therefore, we expected that the distance between small and large NPs should show a variation within ~40 nm due to the flexibility of DNA in liquid.

Table 6.1. Elements of each sample used in the study

| Elements \ Sample | No. 1 | No. 2 | No.3 | No.4 |
|---|---|---|---|---|
| Citrate AuNPs | + | | | |
| DNA1-AuNPs | | + | + | + |
| DNA2-AuNPs | | + | + | + |
| Control DNA | | | + | |
| Hyb-DNA | | | | + |

Table 6.2. Sequences of different DNA oligonucleotides used in the study

| Name | nt | Sequence 5′→3′ |
|---|---|---|
| DNA1 | 30 | TAA GTC TAC GTT GCC AGA CGA AAA AAA AAA-SH |
| DNA2 | 47 | HS-AAA AAA AAA AT CGG GCG AGT CGT CTG TCG TCG TCG TCG TCG TCG TCG |
| Control DNA | 72 | GCG TTT TCG CTT TTG CGT TTT GGG TCA TCT GCT TAC GAT AGC AAT GCT CGG CTT TTT TTT TTT TTT TTG CCG |
| Hyb-DNA | 90 | TCG GGC GAG TCG TCT GGG AAC GTA GAC TTAGTA TAG AAG TCA GGT CTT TTT CGG TCC GCA TCG TCC TCC CGA CGA CGA CGA CGA CGA CGA |

52

Figure 6.3 shows the in-liquid TEM images of a multimer at different time points (A), the trajectory of the small particle in the multimer (B), the measured interparticle distance between the large and small particle (C), and the displacement of the small particle relative to the position in the previous TEM frame for 30 s. The center-to-center distance between NPs at each time step was measured and excluded half the size of both particles to reveal the edge-to-edge linear distance more precisely. As shown in Figure 6.3 B, the distance between the small and large NP fluctuates within 30 nm, which suggests the bonding. We also observed that the resolution of the small particle changes due to the variations in the Z-position of the particle in the consecutive TEM frames.[75]
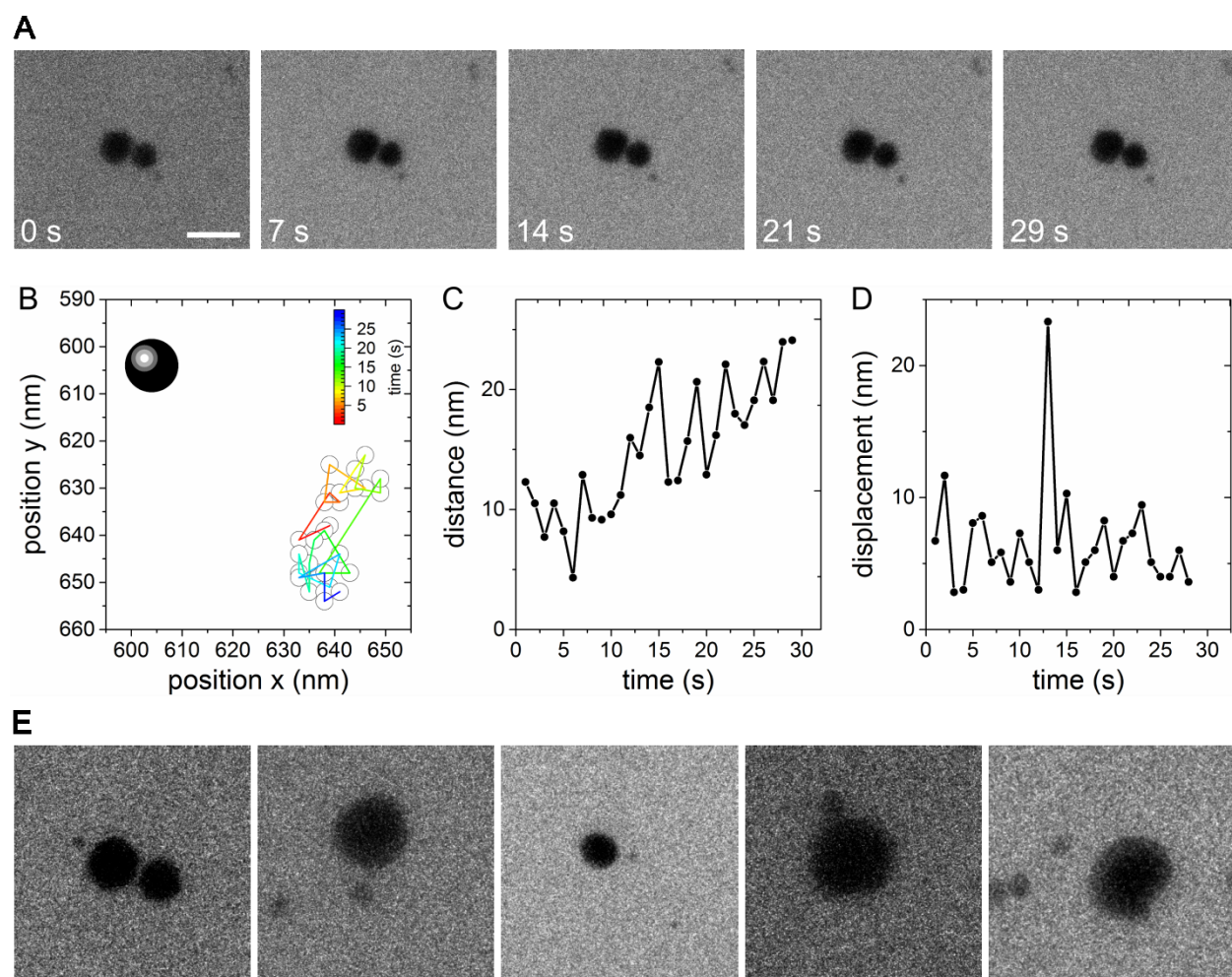


Figure 6.3. 2D analysis of a multimer motion. (A) In-liquid TEM images of a multimer at different time points. (B) Trajectory of a small DNA-AuNP (18 nm) bound to a large DNA-AuNP (55 nm, shown as black sphere). (C) The measured interparticle distance between the large and small particle. (D) Displacement of the small particle relative to its position in the previous

TEM frame for 30 s. Scale bar represents 100 nm, and the color index shows the time traces of the motion. Electron dose rate is 15 e$^-$·nm$^{-2}$·s$^{-1}$. (E) A series of multimers with varying interparticle distances between NPs indicating the flexibility of DNA in solution. (Adapted from reference-46)

As shown in Figure 6.3 E, we observed a high number of different multimers composed of a few big and small NPs with similar type of motion as characterized in Figure 6.3 B-D. We also observed that small NPs move more freely in small multimers compared to the ones in large multimers as shown in Figure 6.2 B (no. 4). It can be suggested that large multimers with many NPs result in a more confined area for NPs to move and therefore their motions are restricted.

For comparison, we investigated the motion of individual DNA-AuNP conjugates (without forming multimer) and observed that they generally move diagonally in one direction due to local heating in the liquid cell (Figure 6.4).
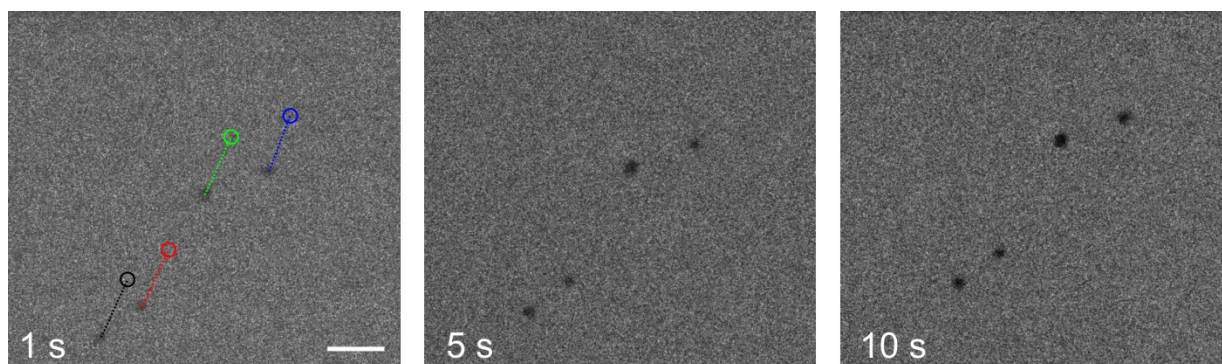


Figure 6.4. In-liquid TEM images of small (~20 nm) AuNPs at different time points. The black and colored spheres on the image (Left) represent the position of each NP at 10 s. Electron dose rate is 15 e$^-$·nm$^{-2}$·s$^{-1}$. Scale bar represents 100 nm and is same for all the images.

We calculated the average displacement of individual DNA1-AuNP conjugates to be 9.6 nm for 1 s of time steps, which was expected to result in a ~290 nm displacement after 30 s. On the other hand, the small particle in the multimer (Figure 6.3 D) exhibits an average displacement of 7.63 nm for 1 s time steps, while its distance to the large particle varies within 40 nm (Figure 6.3 C). This suggests that 40 nm long and mostly single-stranded DNA does not affect the velocity of a small particle significantly; however, it is sufficiently strong to keep the small

particle attached to the large particle. It should be pointed out that the strength of the bond depends on the number of DNA linkers between the particles. The large particle in the multimer did not show any significant motion rather than tumbling with low frequency due to its larger mass and the fact that it is attached to another large particle. We observed a similar motion in different multimers for multiple times. Figure 6.3 E shows some of these multimers imaged for sample no. 4 in different TEM measurements.

We observed larger displacements and an interactive motion within small and large DNA-AuNPs at higher electron beam intensities. Figure 6.5 shows the trajectories of DNA-AuNPs (sample no. 4) involving in the assembly with their associated in-liquid TEM images. We observed in consecutive TEM frames that their displacement is very random and shows variation between 5 and 70 nm at time steps of 1 s for both DNA1-AuNPs and DNA2-AuNPs (Figure 6.5 B) once the electron dose rate exceeds 110 $e^-\cdot nm^{-2}\cdot s^{-1}$. On the contrary, we did not observe such dynamics and assembly behavior in the solution of only citrate-stabilized AuNPs at the same and even higher electron dose rates (140 $e^-\cdot nm^{-2}\cdot s^{-1}$). The pairs and single forms of citrate-AuNPs showed very slow dynamics with very small displacements, requiring observation times of minutes with continuous exposure. This suggests that once DNA-AuNP conjugates are exposed to an electron beam of >110 $e^-\cdot nm^{-2}\cdot s^{-1}$, the DNA on the particle surfaces and additional charging from the electron beam result in a stronger dipole moment between DNA-AuNPs than the ones between citrate-AuNPs. The net effect of these electrostatic forces brings the DNA-AuNPs into close vicinity to one another.

We suggest that these strong dipole forces are originating from the random distribution of the DNA molecules on particles' surfaces.[76] We believe that base-pairing interactions between ssDNA on AuNP surfaces assist them overcome repulsive electrostatic forces and assemble into higher order structures in solution once the interparticle distance becomes smaller than the total length of DNA linker. In general, we could not distinguish the interface region of the small and big particles clearly as they move with high velocities. Also, we could obtain images from only a single projection since we cannot tilt the liquid specimen holder. Due to these methodological drawbacks, we cannot make a sound conclusion about the true characteristics of the interactions in NPs' interface. However, it can be suggested that the reason behind the observed self-assembly is DNA hybridization with complete or partial sequence matching because we did not observe this type of formation without complementary units. On the other hand, nonspecific interactions

between DNA-AuNPs are possible and this might have an effect in the observed assembly at a lower frequency.
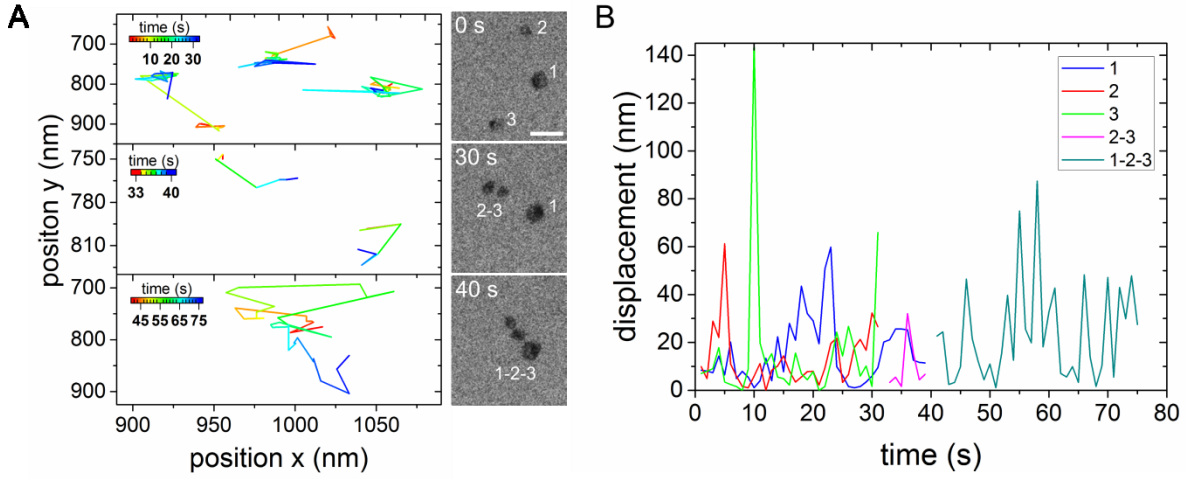


Figure 6.5. Time sequential formation of DNA-AuNP clusters at higher electron doses. (A) Trajectories of DNA-AuNPs (no. 4) with their TEM images in liquid. (B) Displacement of each labeled NP with time steps of 1s. Scale bar is 100 nm and the same for all of the images. Electron dose rate is 110 $e^-\cdot nm^{-2}\cdot s^{-1}$. The center points of the clusters are selected while calculating the trajectories in time. (Adapted from reference-46)

We observed that once the electron dose rate exceeds 110 $e^-\cdot nm^{-2}\cdot s^{-1}$, the DNA-AuNPs in sample no. 4 form pairs first, then trimers and finally 1D grown structures. Figure 6.6 shows the in-liquid TEM images of DNA-AuNPs (A) and citrate-AuNPs (B) at different time points from the onset of the electron exposure. As seen in Figure 6.6 A, single DNA-AuNPs form into mostly trimers and longer 1D chain type structures with continuing exposure. On the contrary, citrate-AuNPs did not exhibit any significant motion in the same time frame at a higher electron dose rate of 140 $e^-\cdot nm^{-2}\cdot s^{-1}$.

We observed that the clusters composed of >3 NPs show a notably different ordering and eventually form into more random structures than 1D pearl-necklace type and 2D aggregates of NPs.[77–79] Figure 6.7 shows the in-liquid TEM images of two DNA-AuNP clusters (sample no. 4) before and after combining into one larger cluster and subsequent motion at different time steps. Figure 6.7 B shows their 3D configurations at 0 and 3 s. As seen in Figure 6.7 A, small particles cannot be distinguished clearly since they can locate in between or on the surface of the big NPs.

In order to construct the 3D configuration of Cluster-2 (green) in Figure 6.7 B at 3 s, the values for x and y axes are directly obtained from the projection of the large particles. The values for the z axis are calculated by using an Euclidean function. In the analysis, we assumed that the particles positioned parallel to the x−y plane (equal z values) at 0 s and the relative distances of large particles in each cluster did not change significantly when they merge into a larger cluster. We found that this assumption is valid since the x−y projection of Cluster-2 and its TEM image at 3 s are matching well.
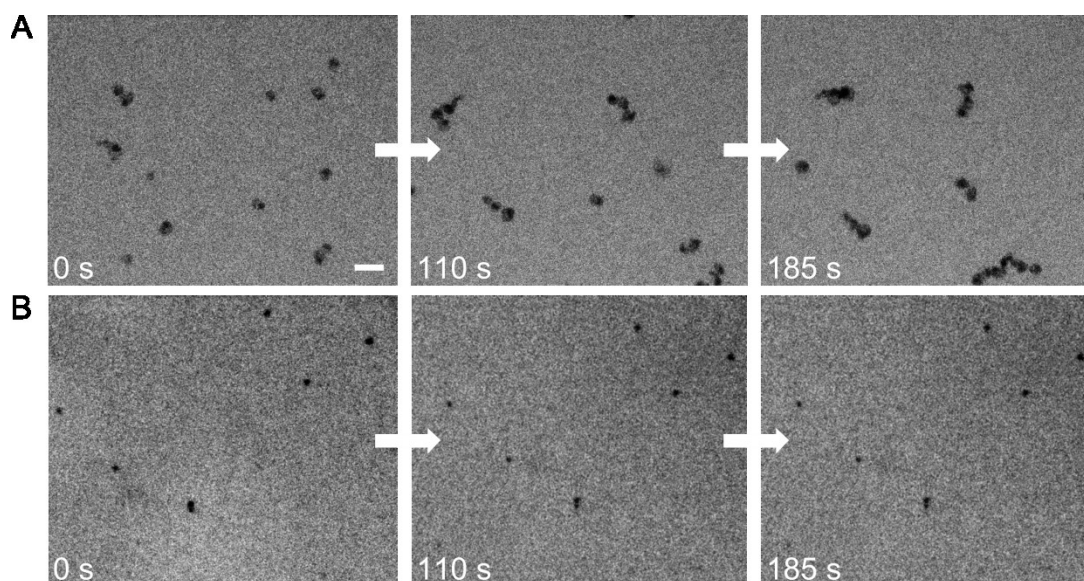


Figure 6.6. (A) In-liquid TEM images of DNA-AuNPs (no. 4) and (B) citrate-AuNPs (no. 1) at different time points. Electron dose rates are 110 and 140 $e^-\cdot nm^{-2}\cdot s^{-1}$ for sample nos. 4 and 1, respectively. Scale bar represents 100 nm and is same for all the images. (Adapted from reference-46)

We believe that ssDNA at the particle interface plays a critical role in the tilting motion of Cluster-2 at 3 s. As seen in Figure 6.7 A, once two clusters combine into one, the overall structure starts to rotate in 3D fashion. The overall height of the cluster was measured to be ~90 nm at 3 s (Figure 6.7 B), which is smaller than the spacer thickness (150−200 nm) of the liquid cell. It should be noted that the limited free space in the liquid cell can affect the configuration of the structures formed and their motion; however, thicker spacers lead multiple scattering events and inevitably result in a loss of the spatial resolution.[75]
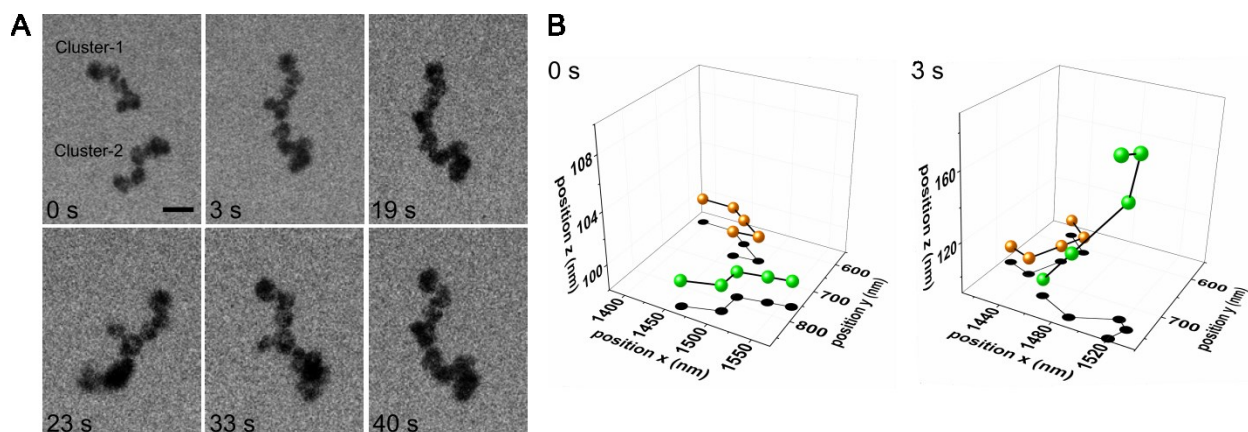
Figure 6.7. 3D configuration of DNA-AuNP clusters (sample no. 4). (A) In-liquid TEM images showing two clusters before and after merging and subsequent motion at different time steps. (B) Their analyzed 3D configurations at 0 and 3 s. The resolved large particles in Cluster-1 and Cluster-2 were shown as orange and green spheres, respectively. The scale bar represents 100 nm and is same for all the images. Electron dose rate is 110 e$^-$·nm$^{-2}$·s$^{-1}$. (Adapted from reference-46)

In conclusion, we qualitatively observed that the hybridization strength of ssDNA was not diminished by electron exposure for minutes at an electron dose rate of 110 e$^-$·nm$^{-2}$·s$^{-1}$. We observed that dimers and larger clusters of the DNA functionalized and the citrate-stabilized AuNPs without complementary units might infrequently form due to nonspecific interactions between the particles. We observed a statically significant larger number of multimers composed of multiple DNA1-AuNP and DNA2-AuNP in sample no. 4 with complementary DNA linkers and to a much lesser extent in sample no. 3 with identical conditions but with non-complementary DNA linkers. This proves that sequence specific hybridization clearly increases the number of AuNPs within a multimer.

In the experiments using higher electron dose rates, we observed intense interactions and interactive motions between DNA-AuNPs due to dipolar forces. These forces bring the particles into close proximity of one another in solution. We suggest that the base-pairing interactions between highly flexible ssDNA are the driving forces for self-assembly of AuNPs into 1D structures with random ordering and dimensionalities. Moreover, the formation of higher order multimers indicates that the structural integrity and the function of the DNA does not vanish under an electron dose rate of >110 e$^-$·nm$^{-2}$·s$^{-1}$ for several minutes. In contrast to DNA-AuNPs,

the suspension of citrate capped AuNPs did not show such dynamics and self-assembly under the same imaging conditions at even higher electron dose rates.

In this study, the electron dose rate was varied between 5 to 140 $e^-\cdot nm^{-2}\cdot s^{-1}$. The effect of intermediate dose rates was examined on sample No.4 and compared with the dynamics observed at 110 $e^-\cdot nm^{-2}\cdot s^{-1}$. A similar effect can also be observed with lower dose rates, but much longer observation times. This effect is not linear, as an example; 10 s of exposure with a dose rate of 11 $e^-\cdot nm^{-2}\cdot s^{-1}$ does not give the same effect as that of 1 s of exposure with a dose rate of 110 $e^-\cdot nm^{-2}\cdot s^{-1}$. That is why we have considered the electron dose rate instead of dose. For inducing the motion, we move to a fresh spot using a certain electron dose rate. If we set the dose rate to >110 $e^-\cdot nm^{-2}\cdot s^{-1}$, the observed dynamics immediately evolve for sample no. 4. We compared this dose rate with the theoretical study by Schneider et al. based on the interactions between electron beam and water and found that our dose rate does not cause any unintended chemical change in the samples.[80]

For calculation of the DNA-AuNP trajectories, the center of NPs is found by first convolving the data with a Gaussian of 1 nm rms radius, and then using a function to find local extrema, with a given minimum volume for noise rejection. The particle positions found in this way were used to calculate the projected distances in the x-y plane. These procedures were performed using ImageJ (NIH). If a particle fluctuates up and down (moving in and out of focusing plane), this blurs its projection. Due to the concomitant decrease in signal-to-noise ratio, this has to be taken into account by increasing the level of noise rejection in the peak-finding function.

This study proves that the static nanocell design can provide a fully closed system for *in-situ* TEM imaging, capable of investigating biomolecular dynamics without liquid loss and over viewing times of up to several hours under the previously described low electron dose conditions.

## 6.1.    Analysis of the Spatial Resolution

We compared the edge slope of the AuNPs in air filled and liquid filled nanocells in order to reveal the loss in the spatial resolution due to the liquid background. We compared these findings with the study by C. Mueller, which uses relatively large SiN windows (100x50 μm) with thinner spacers (45 nm) and under flow conditions.[49] It should be noted here that the previous study involves STEM measurements rather than TEM as we used in this work. The spatial resolution depends on the specimen Z-position, which applies oppositely in TEM and

STEM. In STEM, the structures on top of a substrate give a better resolution compared to the ones on the bottom side of the substrate. This situation is other way around in TEM, which obstructs a sound comparison between these two imaging modes in terms of spatial resolution.[15]

As described above, the liquid background and motion of the particles result in loss of resolution, which appear as blurring the edges of the particles. Therefore, the edge slope is a measure of the achieved spatial resolution for a given substrate and imaging condition. Basically, the steeper the edge gets (the distance from the baseline to the minimum intensity), the better the resolution is. In the analysis sequence, first we extracted line profile from the raw TEM image of AuNPs using the software *ImageJ*. Line profiles are then transferred to the software *Origin* and the edge of the NPs are fitted using Boltzmann equation:

$$y = \frac{A_1 + A_2}{1 + e^{\frac{x - x_0}{dx}}} + A_2 \, , \tag{6.1}$$

where $A_1$ and $A_2$ are the min and max y values of the fitted curve, respectively, $x_0$ is the center of the rising slope and $dx$ is the edge slope or change in the intensity per nanometer at the edge, which is directly related to the spatial resolution.

Figure 6.8 shows bright-field in-liquid TEM image of a DNA-AuNP cluster with the averaged line profile of the marked area (A), Boltzmann fit to the dropped intensity at the edge (B) and the same analysis applied to a dried nanocell (C/D). The edge slope is found to be 4.7±1.9 nm for liquid filled and 2.5±1.9 nm for air filled nanocell with a ratio of [$dx_{\text{liquid filled}} / dx_{\text{air filled}}$] 1.88. In the previous work, $dx$ was found to be 12.3 and 6.6 for liquid and air filled nanocells, respectively, with a ratio of 1.86 at an acceleration energy of 200 kV. Besides the ratio between liquid/air filled static cell is in perfect agreement with the previous work, a remarkable improvement in the spatial resolution was obtained. Although we used thicker spacers for DNA-AuNPs, the smaller lateral dimension of the SiN windows (100 μm x 15 μm) reduces the bulging and results in a better resolution. It is also very likely that the internal pressure in the flow cell is higher than that in the static cell, which further deteriorates the resolution for the flow cell.

We also imaged the polymer nanospheres (polystyrene ($C_6H_5CH=CH_2)_n$) to characterize the obtained resolution and contrast for a light material in water. Figure 6.9 shows the in-liquid TEM images of the polystyrene beads (Sigma-Aldrich, diluted in $dH_2O$ (1:10)) with a diameter of 100 nm in solution (A) and dried on the liquid cell window (C). An edge slope of 13.7 nm obtained from the beads in water indicates that it is possible to observe organic materials with a spatial resolution of ~10 nm in the static nanocell.
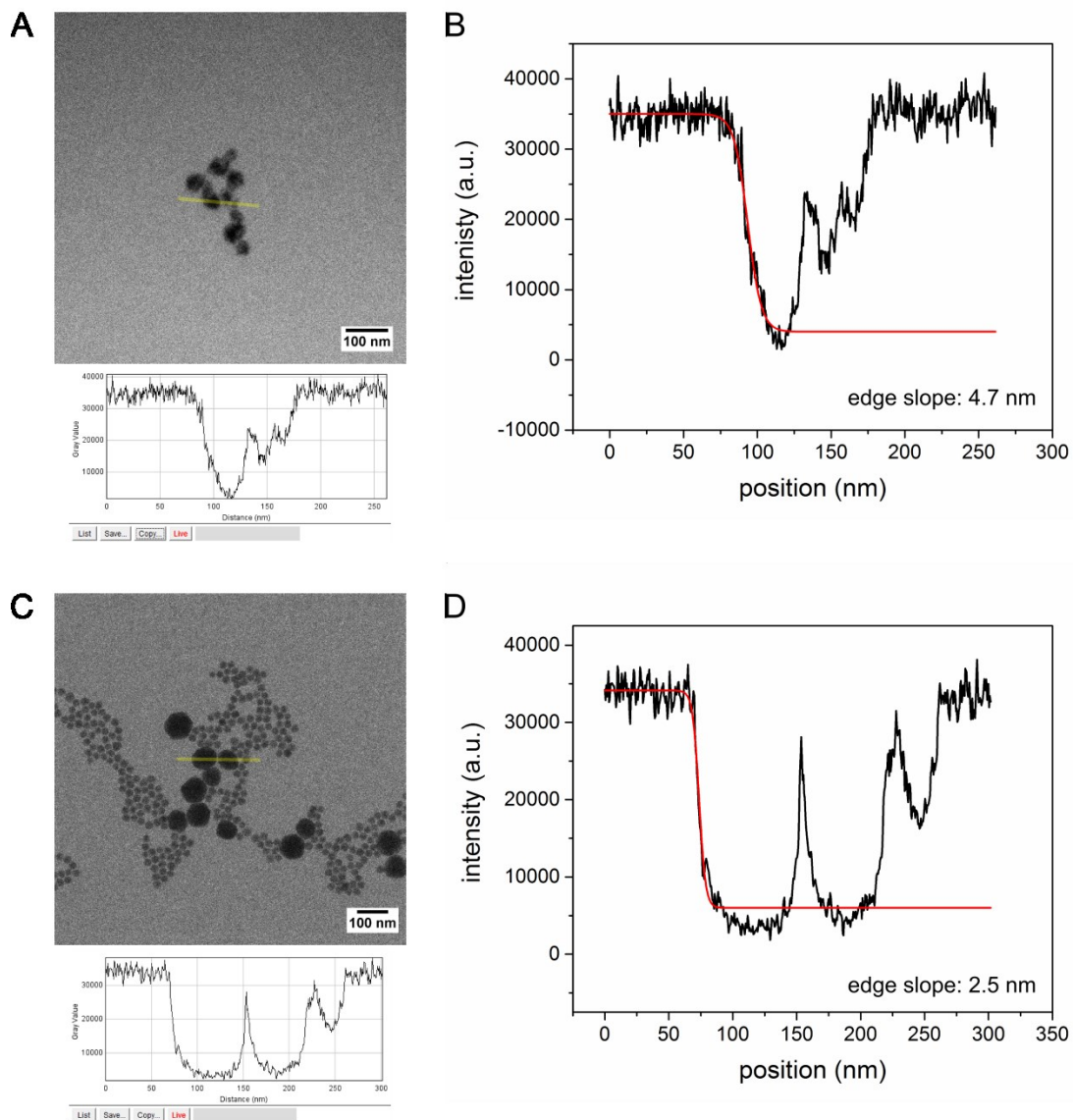
Figure 6.8. Calculation of the edge slope. (A) In-liquid TEM image of a DNA-AuNP cluster with the averaged line profile of the marked area. (B) Boltzmann fit to the dropped intensity at the edge. (C/D) Same analysis applied to a TEM image of DNA-AuNP aggregates dried on the liquid cell window. The aggregates could be stuck on the inner parts of either top or bottom windows in C. Scale bars represent 100 nm (A/C). SiN window dimensions and spacer thickness are 100 μm x 15 μm x 50 nm and 100 nm, respectively.
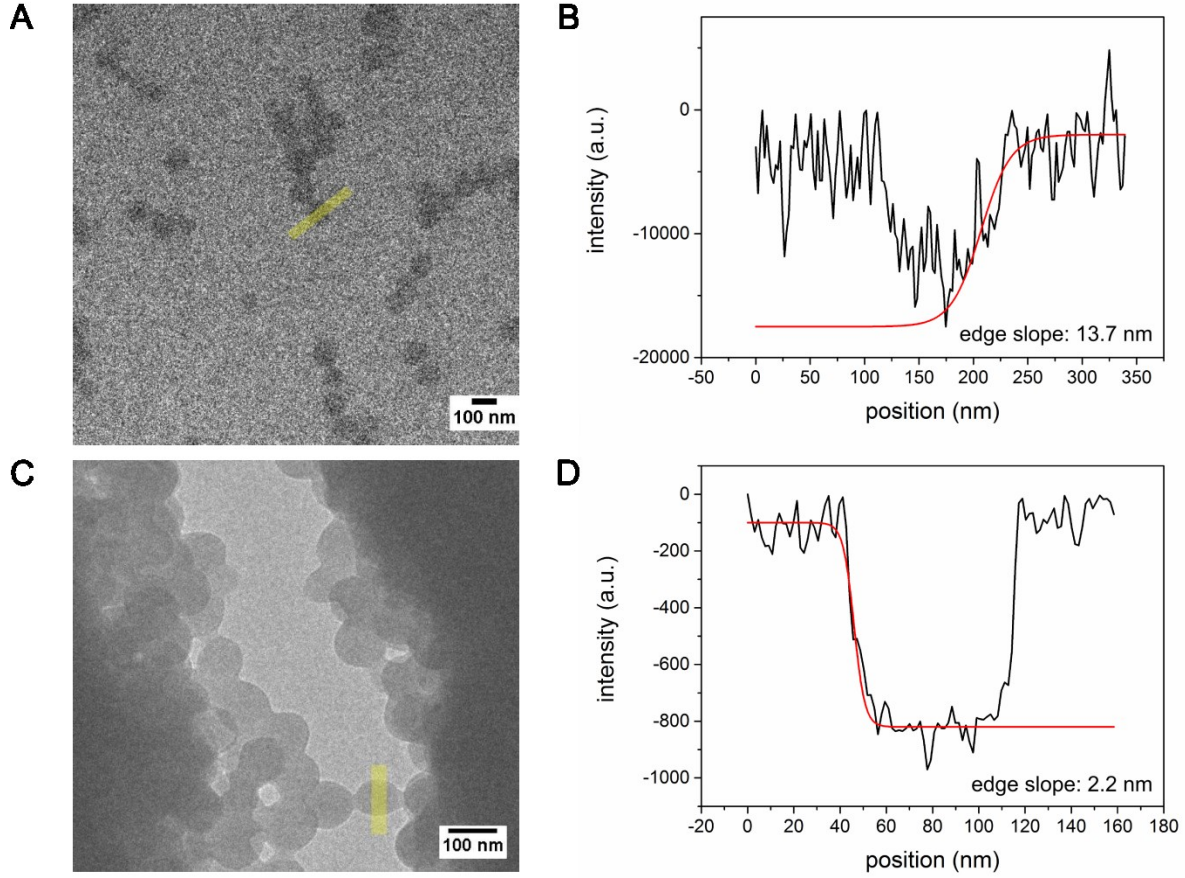
Figure 6.9. TEM images of the polystyrene beads with a diameter of 100 nm in solution (A) and dried on the liquid cell window (C). Plot profiles of the yellow lines shown on each image (B/D). An edge slope of 13.7 nm and 2.2 nm is obtained with and without of solution, respectively. SiN window dimensions and spacer thickness are 100 μm x 15 μm x 50 nm and 100 nm, respectively.

We measured the thin film interference on 100 μm x 15 μm wide SiN windows in vacuum to associate the achieved spatial resolution with the liquid layer thickness. The details of the interferometry setup and the measurements are given in section 5.3.2. The pressure difference between inside and outside of the liquid cell is assumed to be ~1 atm once the cell is exposed to vacuum. We recorded the intensity in the interference pattern and extract the liquid layer thickness. Figure 6.10 shows the images of the SiN windows obtained in vacuum (A) and a plot showing the intensity in the center of the window depending on the pressure difference (B). Due to the geometry and the relative position of the windows, we observed bright and dark lines instead of circles. In Figure 6.10 B, the abscissa might scale non-linearly because the pressure

was not controlled during pumping down. The first fringe appeared immediately after switching the vacuum pump on and the windows reached the maximum bulging with 2.1±0.2 fringes in total. The bulging in the liquid cell windows was calculated as 434±40 nm using Eq. 5.2. This value corresponds to the liquid layer thickness in the center of the viewing area. Since the window is attached to the thick silicon substrate with negligible deflection at the edges, the bulging is considerably less in these areas, which results a respectively higher spatial resolution in these regions.
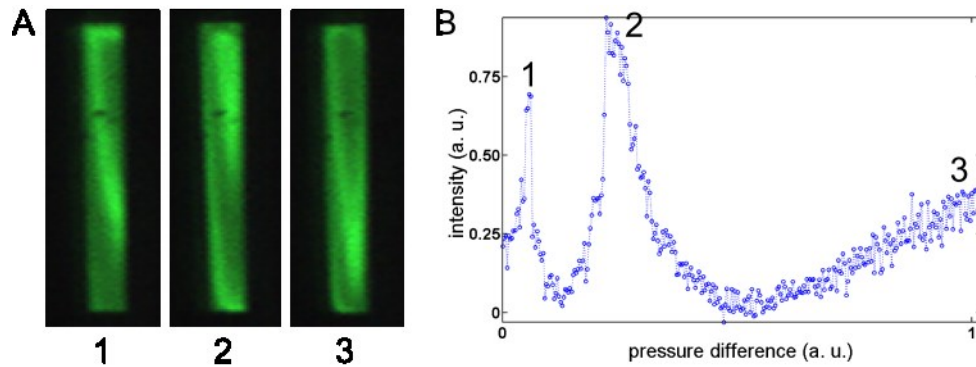


Figure 6.10. Bulging test on 100 μm x 15 μm wide SiN windows. (A) Images of the windows obtained in vacuum and (B) the intensities in the center of the window depending on the pressure difference. (Taken from reference-46)

# 7.    In-liquid TEM Imaging of Fixed and Non-fixed Mammalian Cells

Present imaging techniques for live cells provided extensive information for understanding cell structures, dynamics, and trafficking. It can be considered that light microscopy is the simplest one among these techniques with relatively easy operation and sample preparation procedure. However, the highest resolution for live cell imaging with light microscopy is currently limited to ~200 nm. Super resolution light microscopy can overcome this limitation and achieve a resolution down to ~50 nm (for certain cases to a few nm) for live cell applications. However, these techniques need specific labelling with fluorescent dyes that makes them still quite challenging.[81–85] The spatial resolution offered by light microscopy is significantly lower than what has been achieved with electron microscopy. It is well accepted that state of the art TEM can routinely resolve much finer structures, as the resolution limit reaches well into the atomic range. Electron microscopy is typically used for cell imaging to investigate structures of isolated or fixed cellular components such as membranes or the nucleus.[86–88]

Despite the fact that TEM is superior to optical microscopy in terms of spatial resolution, it is operated under high vacuum, which is detrimental for living systems. Due to this constraint, the traditional approach is embedding the specimen (e.g. tissues) in a supporting material (resin) and subsequently microtoming it to sub-micron thick slices for imaging.[89] This approach is not favorable for radiation sensitive organic specimens especially if high electron doses are used. In order to gain contrast at low electron doses, the specimen needs to be stained using generally osmium and uranyl acetate, both of which are highly toxic and thus cannot be used for live cell imaging.[90,91] On the other hand, cryo-EM allows imaging radiation sensitive specimens such as cells, viruses, bacteria or proteins without staining.[92–94] In this technique, the specimen is frozen with liquid helium or nitrogen and imaged at low temperatures with specific sample holders. Developments such as flash freezing in glass-like ice or plunge freezing of hydrated specimens for cryo-electron tomography allow reconstructing 3D structures of molecular complexes from acquired tilt series of images. However, this technique requires tedious sample preparation and it is not possible to track real-time cellular dynamics under cryogenic conditions.[95,96] Furthermore, formation of ice crystals or local melting of the frozen sample by the electron beam could introduce artifacts such as drifting the specimen during the measurement, which further complicate the data analysis.

The advances of today's micro-nanofluidic devices allow maintaining non-fixed cells fully hydrated in high vacuum and imaging them without freezing or staining under near native conditions. It is possible to culture mammalian cells directly on SiN windows and image them with or without liquid flow using in-liquid TEM. Peckys et al. investigated AuNP uptake in fibroblast cells using a SiN based microfluidic chamber with continuous flow and scanning transmission electron microscopy (STEM).[97] The same group imaged AuNP-labeled epidermal growth factor (EGF) bound to cellular EGF receptors of fixed fibroblast cells in liquid with STEM.[98] In their study, they resolved AuNPs with 4 nm spatial resolution in 7 μm thick microfluidic chambers based on their experimental findings and theoretical calculations. However, they suffered from obtaining low resolution and contrast from the cellular material due to the weak electron scattering from organic molecules and excessively thick liquid layer.

It was reported that multi-layer graphene supported with regular TEM grids can be used to sandwich epithelial cells and allow imaging with TEM.[57] In the study, the specimens are encapsulated with graphene and they achieved nanometer scale resolution. However, graphene, even multilayers, cannot provide a fully closed system, hence the specimen is inevitably dehydrated quickly after first electron exposure, which is a general problem of a graphene liquid cell.

In our study, we combined these two approaches using SiN based static cells without flow and with relatively thinner spacers. In this way, we can hermetically seal the mammalian cells in the static nanocells with a spacing between ~600 nm. Expecting that the thickness of the mammalian cells used are larger than 1 μm, which exceeding the total spacer thickness, we suggest that the mammalian cells are in contact with both windows of the liquid cell.[99]

The SiN windows used in the experiments are deposited with LPCVD with a thickness and elastic modulus of 50 nm and ~230 GPa, respectively.[69] Therefore, they can possibly deform according to the curvature of the mammalian cells without giving excessive stress to them. This suggests that the windows encapsulate the cells to some extent while keeping them fully hydrated during the TEM measurements. This phenomenon is schematically illustrated in Figure 7.1.
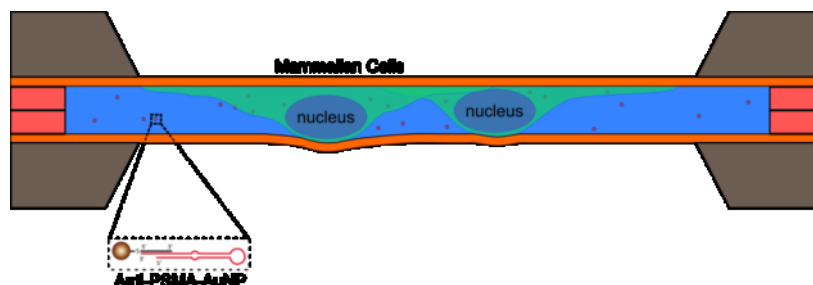
Figure 7.1. Schematic illustration of encapsulated mammalian cells in a nanofluidic cell. Gray: silicon, orange: silicon nitride, red: silicon oxide. Not drawn to scale. Red dots in the liquid cell represent the aptamer functionalized AuNP targeting the surface antigens of the LNCaP cells.

The mammalian cells also exhibit flexibility as well as the SiN windows, in lateral and vertical axes, corresponding to their width and thickness, respectively. This situation offers two major advantages. Firstly, most of the observed structures can be attributed to the ones inside the cells, not the ones located above or below of the imaging plane of the cells.[57] Secondly, the spatial resolution and SNR are significantly increased by using a thin spacer since thick liquid layer around the specimen leads to multiple scattering or absorption of the incoming electrons. Consequently, obtaining images with acceptable resolution at low electron doses leads less radiation damage on the mammalian cells and prolongs the total observation time before the onset of visible damage. Here, we should underscore that the electron radiation damage is one of the major limitations in TEM studies for biological specimens. All types of biological molecules such as DNA, RNA, lipids, and proteins are proven to be severely affected by the radiation damage.[100–102]

In this study, first we investigated fixed PC3 prostate cancer cells with in-liquid TEM without any contrasting agent to evaluate the sample preparation method and in-liquid TEM configuration used in terms of achieved spatial resolution, and determine suitable imaging conditions before proceeding with non-fixed cells. Figure 7.2 shows the schematic overview of the sample preparation of fixed or non-fixed cells for in-liquid TEM measurements.

We observed that the attachment of the cells onto SiN windows takes around 3-6 h. We analyzed the shape differentiation of the PC3 cells on SiN windows with light microscopy at 1, 4 and 24 h after seeding. As shown in Figure 7.3, most of the cells have a round shape and they are floating above the window 1 h after seeding. The cells are still round after 4 h, but in contact with

SiN window and stop floating. After 24 h, most of the cells show the typical long stretched shape. After this point, the cells are fixed with 4% paraformaldehyde (PFA) to preserve their structures. The fixed cells are sealed with 1 μL of ddH2O in the holder to keep the sample wet during the TEM imaging.

Figure 7.4 shows in-liquid TEM images of PFA fixed PC3 cells grown on 200x50 μm SiN windows. Conventional light microscopy (Figure 7.4 A) was used as a map for the following electron microscopy images. Figure 7.4 B-J show the in-liquid TEM images of the cells and their subcellular structures. We observed that cell boundaries, nucleus and nucleoli are resolved without staining and with high contrast even at very low electron doses. In general, the cells were imaged at low dose (~2.5 $e^- \cdot nm^{-2} \cdot image^{-1}$) and we observed first indications pointing towards structural damage on the cells at 90–120 min after the first electron exposure.
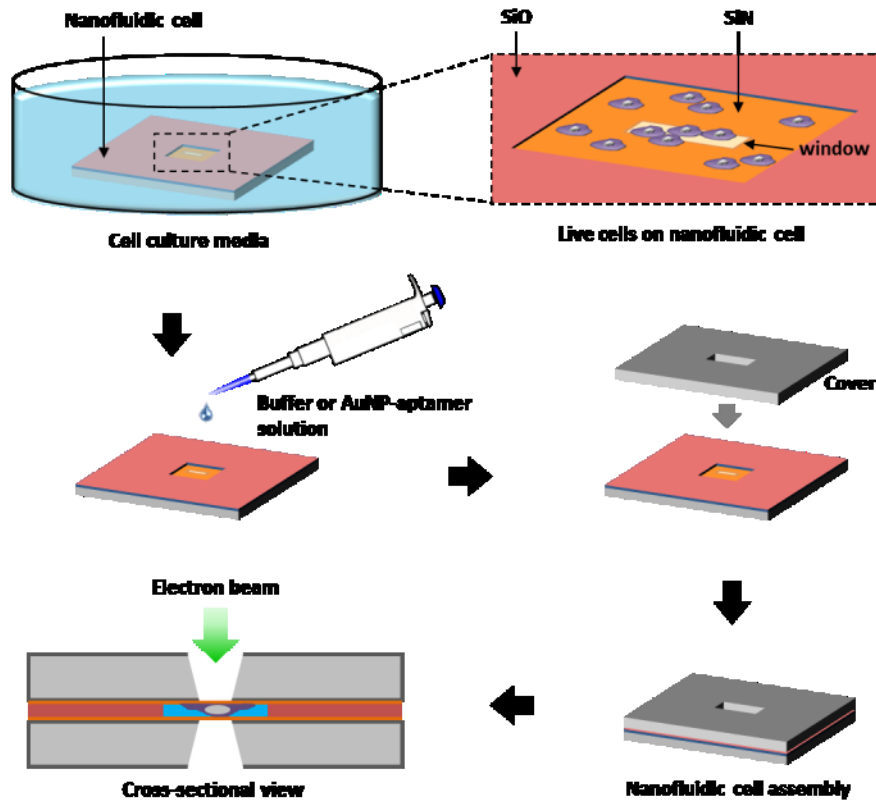


Figure 7.2. Schematic illustration of the sample preparation for in-liquid TEM measurements (not drawn to scale). The nanofluidic cell is inserted into a well and mammalian cells are seeded on the nanocell surface. After culturing the live cells on the nanocell for a certain time, buffer, anti-PSMA-AuNP solution or assay media can be drop casted on the live cells. Then, the nanocell is

covered with an identical nanocell and the assembly is sealed in the holder. (Taken from reference-99)
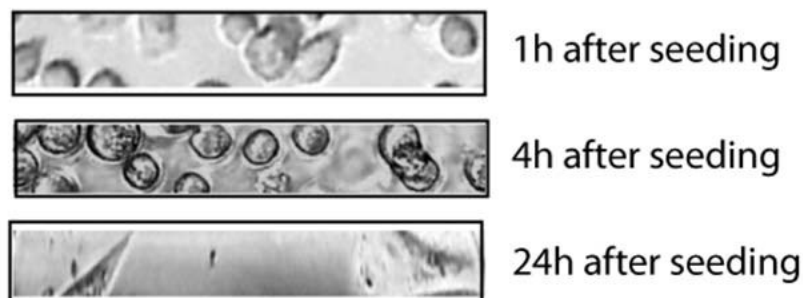


Figure 7.3. Light microscopy images of PC3 live cells on SiN window at different time points. (Taken from reference-99)

We obtained the highest contrast from the nucleus (Figure 7.4 B–H). The nucleoli, which has a high RNA content and thus phosphate groups, can be clearly seen in the nucleus. Figure 7.4 E shows a PC3 cell that was fixed during a late stage of cell division, suggesting that it should be possible to monitor the process of mitosis *in situ* with in-liquid TEM. A higher magnification image of the area marked in Figure 7.4 H (green rectangle) is shown in Figure 7.4 I. It highlights the good resolution and contrast. The small, relatively dark features are 100-300 nm in size, which roughly corresponds to the size of ribonucleoproteins. It is known that ribonucleoproteins are composed of RNA and protein molecules.[103,104]

We validated the observation of nucleus via fluorescence labeling and overlaying of the fluorescence light microscopy and in-liquid TEM images of the same cells. The nucleus was stained using Hoechst 33258, resulting in blue fluorescence (Figure 7.4 J).

The obtained contrast can be attributed to the mass-thickness contrast of the specimen (Z-contrast). The cell boundaries can be distinguished clearly in the obtained images, presumably due to the high phosphate concentration in the phospholipid bilayer. Phosphorus (Z: 15) is relatively heavy and one of the most abundant elements in mammalian cells. It also presents in backbone of the DNA and RNA. This explains that nucleus and nucleoli give higher contrast compared to other cellular structures in the TEM images.
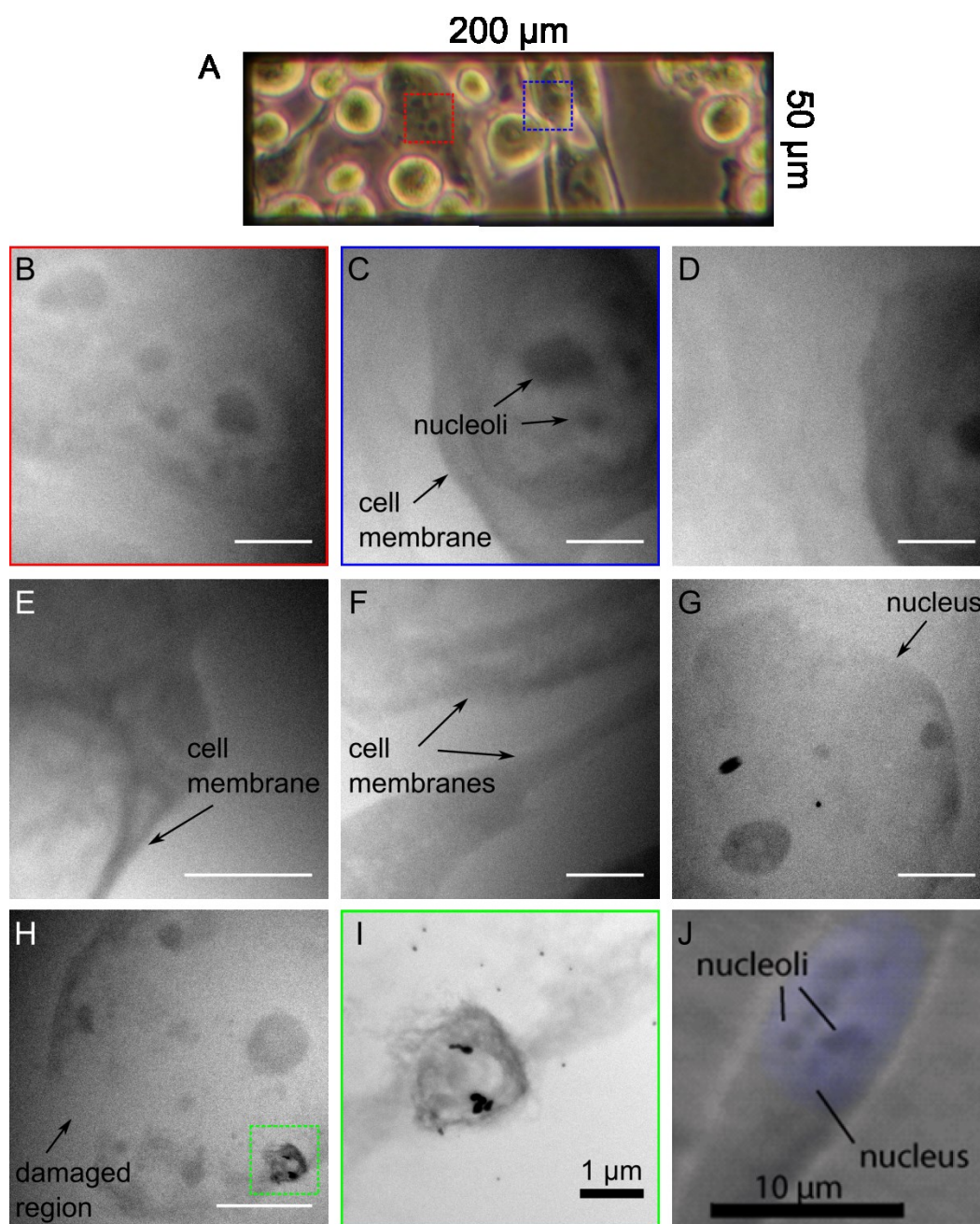
Figure 7.4. In-liquid TEM images of fixed PC3 cells. The electron dose and magnification are ~2.5 e⁻·nm⁻² and 1200x, respectively for the images shown in B-H. The typical exposure time is 1 s. All the scale bars in white color represent 5 μm. (A) Light microscopy overview of the cells on the SiN window. Some of the areas imaged with in-liquid TEM are marked with colored dashed rectangles. (B-D) Cell bodies of PC3 cells. (E) A PC3 cell fixed during mitosis. Two different cytoplasms (light grey) can be seen. (G) Nucleus of another PC3 cell. (H) A region damaged by radiation is marked on the same cell. (I) High magnification image of the marked area in H showing fine structures within the nucleus membrane, captured with an electron dose of

70 e$^-$·nm$^{-2}$. (J) Confocal light microscopy image of a PC3 cell to visualize the DNA staining (blue). (Adapted from reference-99)

We did not observe any noticeable structural damage in the fixed cells over 90 min of observation time at a low electron dose mode (~2.5 e$^-$·nm$^{-2}$·image$^{-1}$). We analyzed around 50 cells individually with the similar imaging conditions and observed that over a cumulative dose of 1000 e$^-$·nm$^{-2}$ causes visible damage on the fixed PC3 cells. It suggests that the structural integrity of fixed PC3 cells can be maintained during the in-liquid TEM measurements for a certain time depending on the total electron dose used. Besides imaging with low electron dose, we suggest that encapsulation of the cells with the SiN windows can also protect their structural integrities.

Here, it should be pointed out that the onset of the radiation damage on the cells is not clear since we can obtain only structural information by TEM. Unfortunately, we cannot recover the imaged cells after the experiment for a viability test since it is not possible to open the sealed liquid cell without rupturing the cell membranes. Therefore, we can currently conclude only the structural integrity of the cells, not their functionality during or after the imaging.

It was reported that the wet biological membranes are disrupted by the electron beam with a dose of 30 e$^-$·nm$^{-2}$. [105] We suggest that diffusing of beam generated radicals out of the beam exposed area and recombination of the hydrated electrons in liquid allow us using higher cumulative doses before the onset of the damage. As a side note, we observed a detached part of the nucleus membrane drifting in the surrounding. This indicates that the surrounding of the fixed cell was hydrated during the entire imaging time and liquid loss is negligible (Figure 7.5).

We confirmed by the above presented results that we could obtain sufficient resolution and contrast from the PC3 cells with the nanofluidic cell and above mentioned TEM configurations. Therefore, we continued with imaging of non-fixed PC3 cells with in-liquid TEM. The non-fixed mammalian cells are in their near-native state; hence they can exhibit cellular dynamics. We seeded the PC3 cells on the SiN windows and allowed them to grow for 4 h at 37°C and 5% CO$_2$ in a cell culture incubator. The nanocell was sealed with an identical nanocell 4 h after seeding. When the PC3 cells are still in the settlement phase, they don't exhibit the typical long stretched shape; instead they appear more rounded and larger during the

attachment onto SiN (Figure 7.3, 4 h after seeding). We used these PC3 live cells to track their cellular and adhesion dynamics with in-liquid TEM.
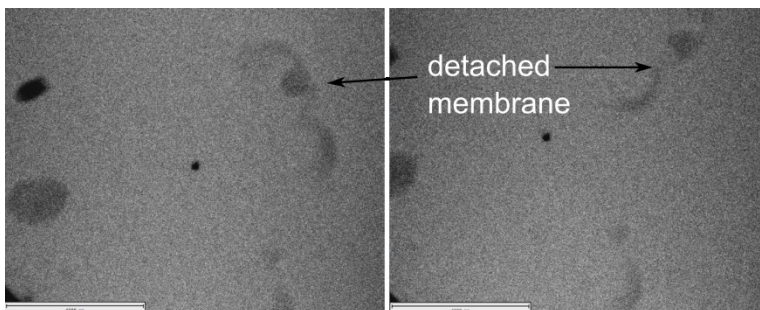


Figure 7.5. In- liquid TEM images of a fixed PC3 cell captured at approximately 90 min after the first electron exposure with a dose of 2.5 $e^-\cdot nm^{-2}$ and a cumulative dose of ~1000 $e^-\cdot nm^{-2}$. The intact form of the same cell can be seen in Figure 7.4 G. The scale bars represent 6 μm.

Figure 7.6 shows a compiled TEM image of a PC3 cell with four consecutively acquired frames (A), in-liquid TEM images showing vesicles in motion (B–E) and a plot showing the distance of one of these vesicles (vesicle-1) to the cell boundary as a function of time (F).

We imaged half of an entire cell in four individual TEM frames (Figure 7.6 A) since we cannot decrease the magnification any further without changing the TEM imaging mode. Surprisingly, the cell boundaries appeared as a mesh like structure, which could be a result of their phase. The PC3 cells were imaged when they were attaching onto the SiN thus they did not exhibit the final stretched shape. Gauthier et al. investigated the folding and shape differentiation of cell membranes during mitosis.[106] In their work, it is shown that cell membrane can form into different shapes depending on the phase of the cell, which determines the type of molecules presenting in the membrane. This phenomenon continues with endocytosis and active trafficking of these molecules in the cell. Our observations suggest that it is possible to study the dynamics of mentioned cell restructuring, adhesion and active trafficking in real time with in-liquid TEM.
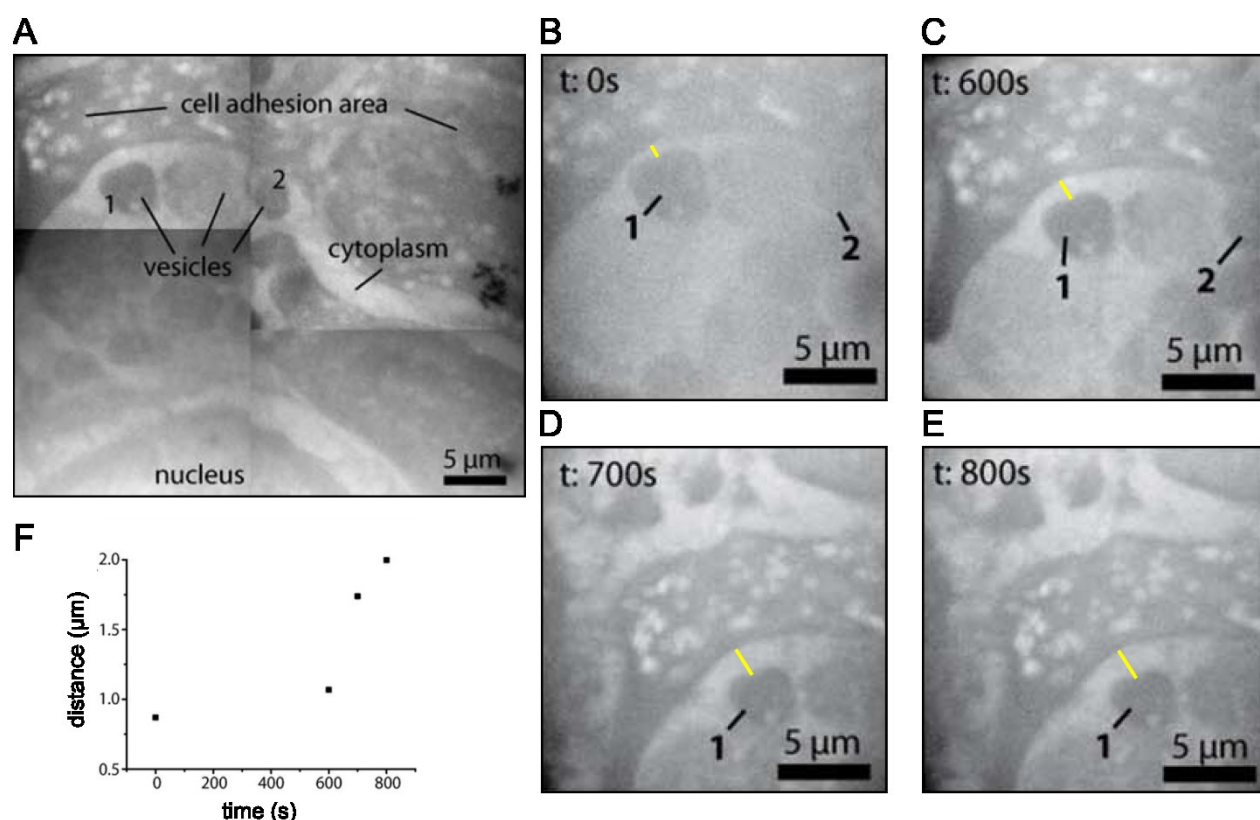
Figure 7.6. In-liquid TEM images of non-fixed PC3 cells. Cells were directly seeded on SiN windows, allowed to settle down for 4 h and prepared for imaging. (A) Compiled image of a PC3 cell with four single images. (B–E) In-liquid TEM images of vesicle-1 and (B-C) -2 at different time points. (F) Plot showing the edge-to-edge distance between vesicle-1 and the cell boundary as a function of time. The yellow bars on the images B–E represent the measured distances. (Adapted from reference-99)

Even though we missed the onset of the adhesion process, we were able to capture intracellular dynamics in the same cell by taking images with time steps of 3 min. We observed two different structures near the cell membrane that showed displacement in time (Figure 7.6 B–E). Since they have similar contrast with the cell boundary, which indicates similar thickness and molecular composition, their shape and close proximity to the boundary, we suggest that these structures might be vesicles. We located a second vesicle (vesicle-2) at even closer to the cell boundary. It seems that it is in the budding process (Figure 7.7 at 0 s), which is known for different types of vesicles (clathrin coated particles, macropinocytosis etc.).
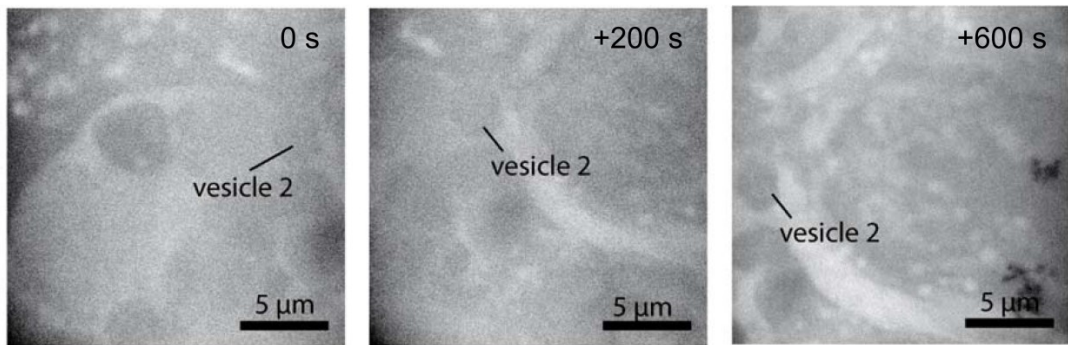
72

Figure 7.7. In-liquid TEM images of the cell boundary of a PC3 cell. Images show the motion of vesicle-2 relative to the cell boundary over 10 min. (Taken from reference-99)

We tracked the displacement of vesicle-1 and plotted as a function of time shown in Figure 7.6 F. Vesicle-1 with a diameter of ~3 μm moved ~1 μm towards the cell center within 13 min. After 744 s, we did not observe any significant motion in the vesicle-1 and -2. We observed that they get into contact with dense material and stopped moving. Despite the fact that we monitored the these structures in motion, it is not possible to identify vesicle type with label-free TEM imaging since there can be various types of vesicles within a cell such as transport vesicles, secretory vesicles, clathrin coated pits, vesicles formed after micropinocytosis, apoptotic bodies and stress vesicles.[107,108] The use of selective labelling methods should allow one to identify different vesicle types.

The non-fixed PC3 cells in this measurement were imaged with an electron dose of ~6 $e^-\cdot nm^{-2}\cdot image^{-1}$ (exposure time of 1 s per image) and ~120 $e^-\cdot nm^{-2}$ in total.

It is challenging to calculate the achieved resolution on live cells with in-liquid TEM due to the flexible cellular material composed of light atoms and liquid background. In order to estimate the resolution, we used internalized AuNPs in the cells. The AuNPs are functionalized in a way similar to that in our previous work presented in chapter-6.

We used LNCaP cells for the internalization of AuNPs of 20 nm in size. LNCaP cells present the prostate specific membrane antigen (PSMA) on their surface, which can be targeted with anti-PSMA-aptamer functionalized AuNPs.[109] It is reported that PSMA is internalized into live cells by either ligand-mediated endocytosis or spontaneously.[110,111] An aptamer is a short single stranded oligonucleotide of RNA or DNA, which can bind to its target by folding into a 3D structure.[112,113] The anti-PSMA design used in this study was reported previously by Lupold et

73

al.[114] Anti-PSMA molecules are coupled with AuNPs with a diameter of ~20 nm following the procedure and experimental design reported by Mirkin et al.[115] and Kim et al.[109], respectively.

Upon functionalization of 20 nm AuNPs with aptamers and non-binding controls, binding was characterized via dynamic light scattering (DLS). A significant increase was detected in the hydrodynamic diameter of AuNPs after coupling and hybridization with either anti-PSMA or control aptamer (Appendix-3, Table A3.2).

First the internalization of the particles was checked at different time points via dark-field light microscopy. Figure 7.8 shows a schematic overview of the functionalized AuNPs with anti-PSMA-AuNPs (A) and a non-binding control (B) and dark field microscopy images of LNCaP cells targeted with either anti-PSMA-AuNPs or control PSMA-AuNPs at 5, 10 and 20 min (C). The signal originated from AuNPs appears as bright orange dots in the images. The more AuNPs are internalized, the brighter the detected signal is obtained. As clearly seen in Figure 7.8 C, a greater fraction of the observed AuNPs is in the LNCaP cells compared to control group, which suggests a high internalization capability for anti-PSMA-AuNPs.
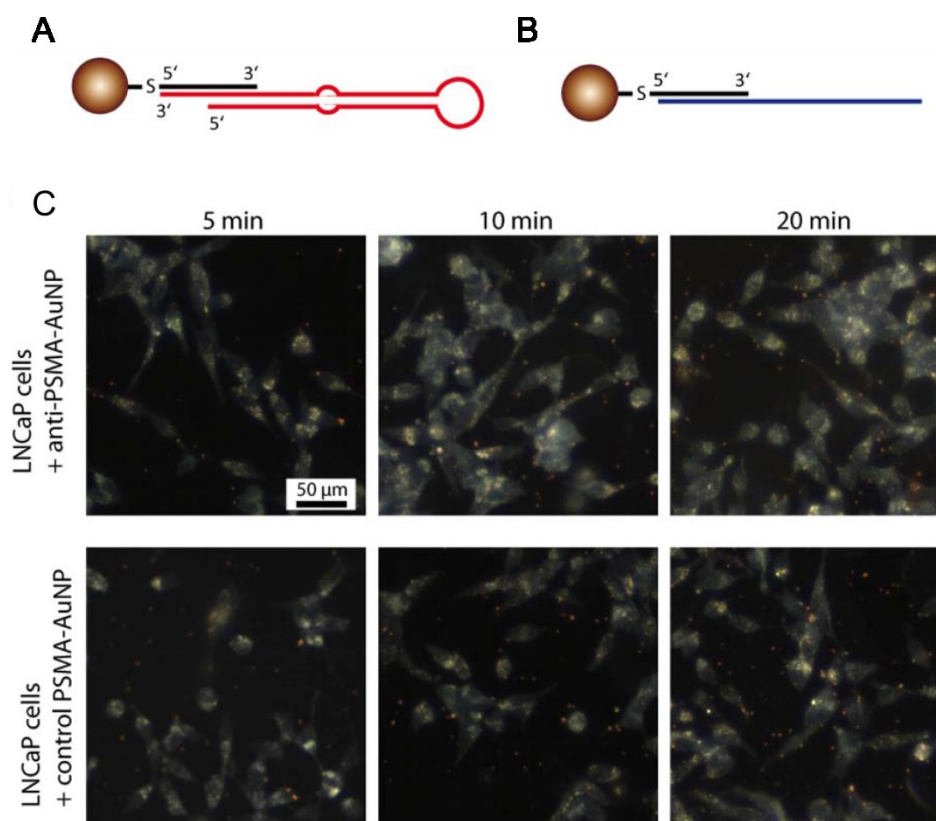


Figure 7.8. Internalization of anti-PSMA-AuNP into LNCaP cells. (A) Schematic overview of the AuNPs functionalized with anti-PSMA-AuNPs and (B) a non-binding control. (C) Dark field

microscopy images of LNCaP cells treated with either anti-PSMA-AuNPs or control PSMA-AuNPs for 5, 10 and 20 min. Scale bar represents 50 μm and is the same for all the images. (Taken from reference-99)

After confirming the internalization capability of the aptamer-AuNPs, we proceeded with in-liquid TEM measurements of the same system. Figure 7.9 A shows a light microscopy overview of the SiN viewing area seeded with LNCaP cells. We moved to the edge of the window since the bulging of the SiN windows is significantly reduced in these regions, which leads to a better resolution.
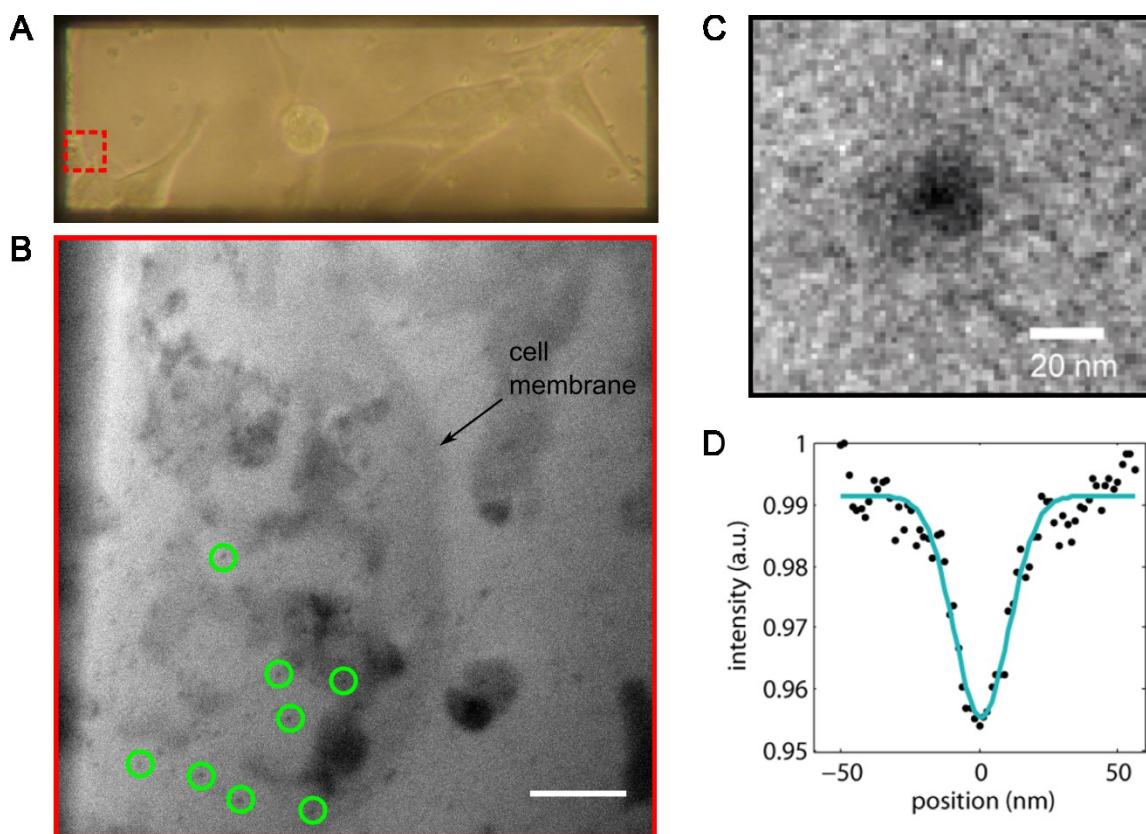


Figure 7.9. In-liquid TEM image of LNCaP cells targeted with anti-PSMA-AuNPs. (A) Light microscopy image of the SiN viewing area with LNCaP cells grown on the window. The region imaged with in-liquid TEM is marked in red. (B) In-liquid TEM image showing the membrane of the cell and single or cluster forms of anti-PSMA-AuNPs in the liquid and in different parts of the cell (partially highlighted with green circles). (C) An average image of the particles highlighted

in B. (D) The integrated profile of the averaged particle intensity shown in C with a Gaussian fit. Scale bar in B is 500 nm. (Adapted from reference-99)

Figure 7.9 B shows the LNCaP cells targeted with anti-PSMA-AuNPs. Some of the anti-PSMA-AuNPs are highlighted with green circles. Interestingly, we obtained slightly lower contrast from the nucleus and other cellular structures of the LNCaP cells compared to the PC3 cells without AuNP treatment. The highlighted particles in Figure 7.9 B were used for an estimation of the effective point resolution. We found AuNP locations as intensity minima after applying a Gaussian filter. Figure 7.9 C and D show an average of the particle images and the integrated profile of the averaged particle intensity, respectively. We calculated a FWHM of 27 nm from the averaged profile of the chosen particles. By considering the size of the AuNPs (20 nm), we can estimate a resolution better than 10 nm. Here, it should be pointed out that this value is not a direct measure of the achieved spatial resolution for mammalian cells, but rather of the smallest AuNP labels that can be resolved in mammalian cells with the presented method, which is a very important quantity for studies of endocytosis of labeled molecules.

We used an electron dose of ~40 $e^-\cdot nm^{-2}\cdot image^{-1}$ with a cumulative dose of ~2700 $e^-\cdot nm^{-2}$ for the non-fixed LNCaP cells. We observed first signs of structural damage in the form of ruptured cell membranes at 30 min after the first exposure. Our work constitutes *in situ* TEM imaging of non-fixed cells, and demonstrates exceptionally high total applied electron dose while preserving cell function to a certain extent. Not that the dose per image used in this study is significantly less than the one used for epithelial cells imaged with graphene liquid cell (~500 $e^-\cdot nm^{-2}$).[57] For a comparison; Kennedy et al. used a cumulative dose of 16300 $e^-\cdot nm^{-2}$ at 300 kV STEM for imaging *Escherichia coli* and P1 bacteriophages in their study.[105]

In conclusion, we managed to capture significant cellular dynamics of active trafficking in a non-fixed PC3 cell in real time. To the best of our knowledge, this is the first time that an intracellular transport event in a mammalian cell is recorded in real time with in-liquid TEM. We calculated the resolution in ~1 μm thick liquid cells using internalized AuNPs to be <10 nm. We suggest that encapsulation of the mammalian cells with SiN reduce the sample thickness thus increase the spatial resolution at low electron doses. Furthermore, using low electron dose reduces the radiation damage and leads to a significant increase in the total observation time with electrons.

As a follow up study, we will be working on monitoring AuNP–aptamer internalization and their fate in non-fixed cells in real time. The duration of this internalization process is ranging from milliseconds to minutes. Monitoring this process in nanometer scale leads to a better understanding and developing new tailored strategies for many life-threatening diseases like cancer[116] metabolic[117] or neurodegenerative diseases[118,119] that show altered endocytosis profiles. However, this is a very challenging task since AuNPs are internalized in relatively short time upon mixing with the cells (Figure 7.8) and the total observation time with TEM is limited due to the radiation damage. The sample loading into the liquid cell holder takes 15-20 min with the current setup. In order to catch the onset of the internalization process, a faster sample introduction is required. Alternatively, flow cells can be used to introduce AuNP-aptamers during the imaging. However, flow cells might require a greater channel thickness in order to flow the solution into the viewing area (to mammalian cells) without clogging the channel. This approach generally requires higher electron energy and STEM to avoid compromising the spatial resolution.[98,105]

# 8.    Visualization of label-free and AuNP tagged DNA origami structures with in-liquid TEM

Today's DNA technology offers the possibility of controlling DNA strands at nanometer scale to synthesize 2D/3D periodic or aperiodic structures for their potential use in biomimetic systems, energy transfer and photonics, molecular biophysics, diagnostics and therapeutics for human health.[120–124] Introducing the concept of using *scaffold* DNA to form aperiodic structures is one of the most crucial developments in DNA nanotechnology. If we underscore a few significant work in this field: Yan et al. used long ssDNA to organize double-crossover tiles into barcode patterned lattices[125] and Shih et al. used 1.7-kb ssDNA as a scaffold for the assembly of a 3D wire-frame octahedron.[126]

The concept of "DNA origami" was first introduced in 2006 by using a long scaffold strand (from the M13 phage genome, ~7,429 nt) and hundreds of short *staple* strands, which fold the long strand into desired 2D shapes. These 2D origami structures can be used as molecular stations (like a pegboard), where various type of proteins or NPs can be selectively attached with a precision of 4–6 nm.[127] Our collaborators from The University of Ulm (Prof. Tanja Weil group) provided such molecular pegboards for various applications in combination with in-liquid TEM. These 2D structures are ~100x70 nm in size, offers a monolayer of DNA array, where AuNPs can be attached on desired locations with conventional thiol bond. First we imaged plain origami structures without AuNP tagging. Figure 8.1 shows some of the planar DNA origami structures observed with in-liquid TEM. Surprisingly, 2D monolayer DNA planes provided high contrast without any contrasting agent in solution. The reason behind this could be the low frequency motion of the large origami structures compared to ssDNA (chapter-6), which allows us capturing them with low camera readout speed.
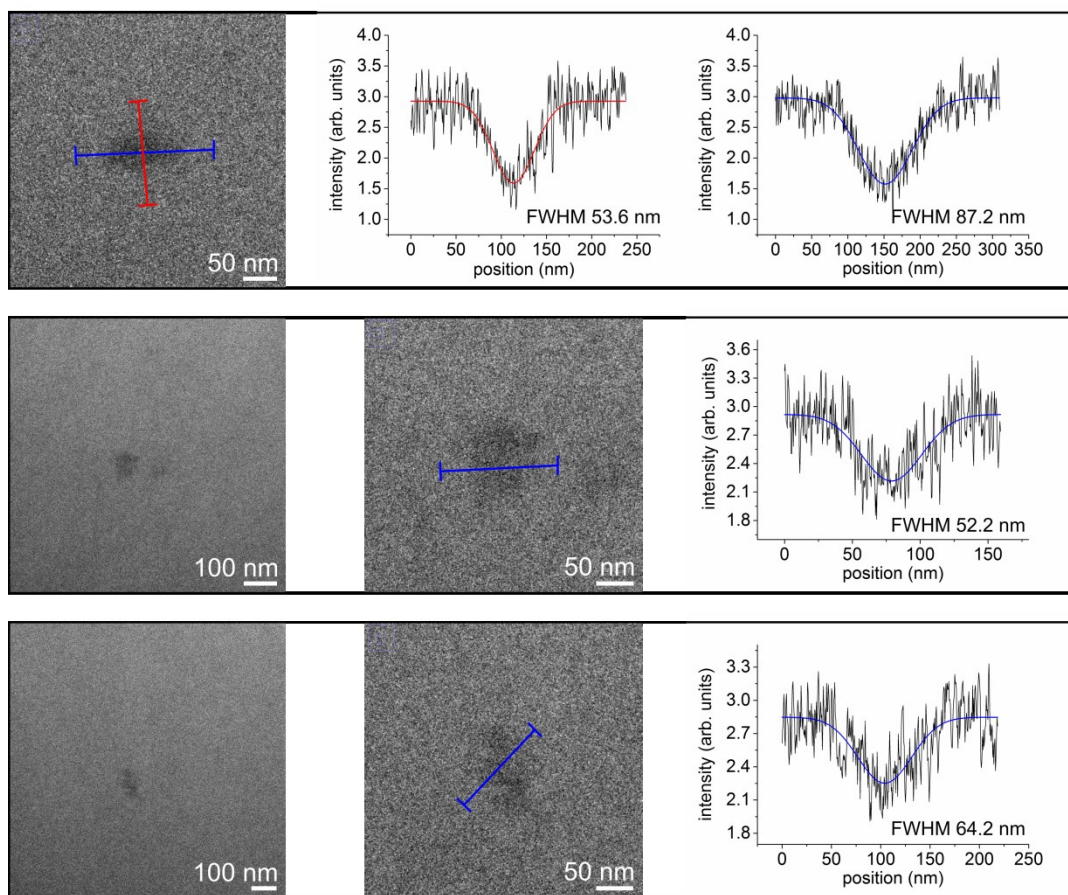
Figure 8.1. Visualization of DNA origami structures in solution. The origami structures are designed to be ~100x70 nm. The averaged line profiles are next to each figure. The lateral dimension and the thickness of the SiN windows are 100x15 µm and 50 nm, respectively, for each image.

We repeated the same measurements for the AuNP tagged DNA origami structures. The same structures are functionalized in the crossed corners or in the center with thiol groups for AuNP attachment as schematically illustrated in Figure 8.2 A. Theoretically; it should be possible to monitor the dynamics of the origami structures by following the trajectories of the AuNPs at different locations. The presence of the unbound AuNPs in solution also helps us to identify the direction of a possible convection flow in the static liquid cell. Figure 8.2 shows the in-liquid TEM images of the DNA origami structures labelled with AuNP(s) in the center (B) and in the crossed corners (D). The average diameter of the AuNPs is 20 nm. The line profile with a Gaussian fit given in Figure 8.2 C matches with the known size of the AuNPs. The 2D surface

plot given in Figure 8.2 C reveals the size of the overall structure and the locations of the AuNPs more precisely.
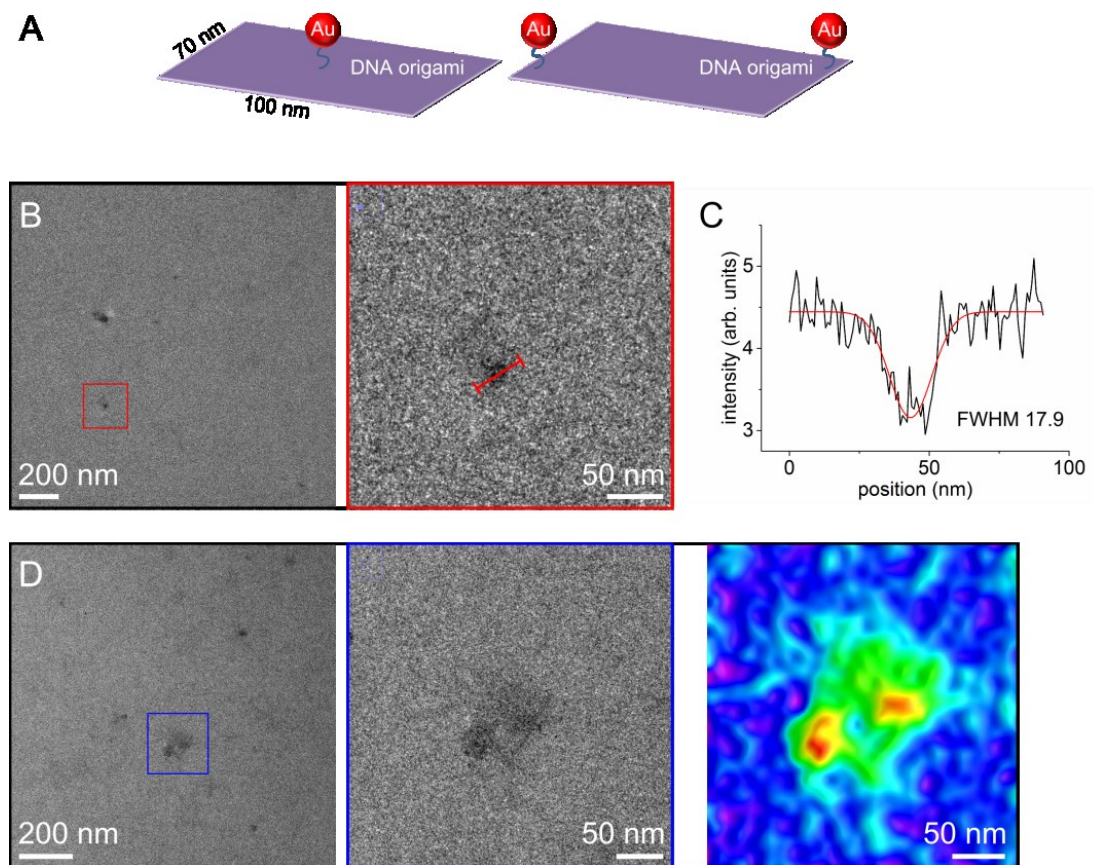


Figure 8.2. (A) Schematic illustration of the AuNP attached DNA origami structures. (B) In-liquid TEM images of the DNA origami structures labelled with a single AuNP in the center. (C) Plot profile of the line in B with a Gaussian fit. (D) In-liquid TEM images of the DNA origami structures labelled with AuNPs in the crossed corners with a 2D surface plot.

We observed the drifting of the unbound AuNPs in solution possibly due to a convection flow in the liquid cell as shown in Figure 8.3. In this experiment, we used the same origami structures but functionalized with smaller AuNPs of 8 nm in diameter. The structure shown in Figure 8.3 clearly has a single AuNP attached in one of its corners. As seen, the attached NP keeps its position while the unbound particles are drifting in the solution, which clearly suggest the bonding between the DNA origami and the NP. We observed that the attached AuNP was tumbling at low frequency, which blurs its projection in the consecutive TEM images. These findings suggest that the observed DNA origami structures are adhered on one of the SiN

windows probably due to electrostatic interactions. It is well known that phosphate backbone of DNA results a negative charge and considering the studied origami structure is composed of hundreds of DNA building blocks, it is very likely that it has a strong negative charge. On the other hand, it was reported that SiN windows are charged positively upon beam exposure because of the ejected secondary electrons from the material.[48] Therefore, the charged windows can attract the DNA origami structures. Although this situation is disadvantageous for investigating DNA origami dynamics, it also offers a platform on the SiN window, where can easily be functionalized for the attachment of various types of compounds such as metallic or polymeric particles or proteins. Whit this utility, same molecule can be kept under the electron beam (imaged continuously) while changing the solvent specifications such as pH or salt concentration with *in situ* flow to trigger dynamics.
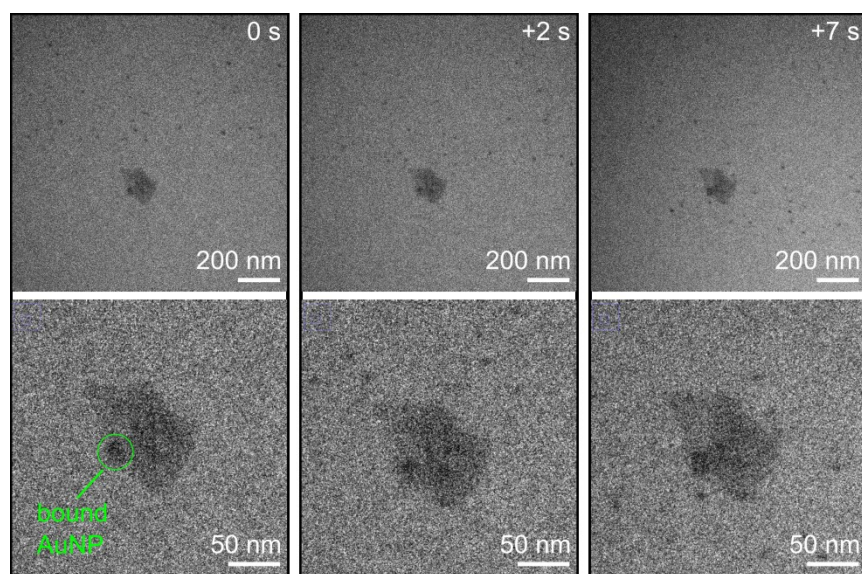


Figure 8.3. In-liquid TEM images of a DNA origami tagged with single AuNP in its corner at different time points. Drifting of the unbound AuNPs indicates a flow in the liquid cell.

# 9.    In-liquid Electron Diffraction on Water

The water molecules in the liquid phase are in an approximately tetrahedral arrangement, which is originated from four sp$^3$–hybridized electron valence pairs on oxygen. Two of these pairs are covalently bonded to two hydrogen atoms. The O–H bond has a polar character due to the greater electronegativity of oxygen compared to hydrogen; consequently oxygen partially exhibits a negative charge and the hydrogen atoms exhibit a partial positive charge. This partial charging is crucial for the interactions between neighboring water molecules and as a result, hydrogen bonding network in bulk water. There are other polar interactions in water, however hydrogen bonding is typically stronger and considered a class of its own. The oxygen in O–H covalent bond forms hydrogen bonds with the hydrogen atoms of neighboring water molecules, as depicted in Figure 9.1. One important characteristic of hydrogen bonding in water is its linearity for O–H···O bond. The linked water molecules provide a great internal cohesion to the overall structure and gives water unusual properties such as high melting and boiling points, and heat of vaporization compared to other solvents.

Another interesting property of water originated from the hydrogen bond network is that it reaches the maximum density at 4 ºC. As the temperature increases from 0 to 4 ºC, the ice clusters melt down to more and more water molecules, however the volume does not change in this ice-like structure due to the intermolecular attraction provided by hydrogen bonding. Therefore, the number of water molecules in the same volume increases, hence the density increases. After 4 ºC, the molecules start to vibrate/move faster at higher frequencies and their energy overcomes the barrier of the hydrogen bond network so the density starts decreasing continuously as the temperature increases (it behaves like a common substance).[128]
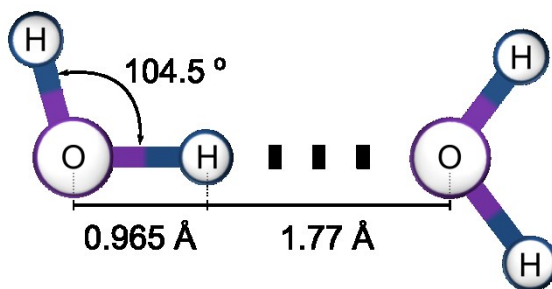


Figure 9.1. Two $H_2O$ molecules joined by hydrogen bonding.[129]

The H–O–H bond angle is 104.5º, which is slightly less than 109.5º of a perfect tetrahedron. The bond dissociation energy of O–H covalent bond is 470 kJ/mol. The hydrogen bonds between adjacent water molecules are relatively weaker with dissociation energy of ~23 kJ/mol. The kinetic energy of individual water molecules at room temperature is almost equal to the energy needed to break down neighboring hydrogen bonds. Therefore, a continual bond formation and break down take place at any given time. The life time of each hydrogen bond is 1 to 20 picoseconds ($10^{-12}$ s) and the formation of a new hydrogen bond takes only 0.1 ps.[129]

The structure and molecular arrangement of water is much more complicated than presented in this chapter. A more detailed discussion is beyond the scope of this thesis. We will continue by discussing the state of the art of investigations on water with X-rays and electrons.

The structure of water has been studied successfully with X-rays[130] in late 1930s and more experimental and theoretical work based on investigating the effect of temperature and pressure on water with X-rays have followed.[131–134] The problem with X-ray diffraction is that the contribution of H–O correlation is small and H-H correlation is negligible since the scattering cross section of hydrogen for X-rays is very small.[135] The X-ray studies on water give information mainly about O–O correlation since the oxygen has the highest electron density in the system. On the other hand, electrons scatter from the nucleus and they interact with matter more strongly compared to X-rays. This gives electrons a fundamental advantage for studying light matter. However, the number of reports with electrons is much less mainly because of their greater elastic scattering cross section comparing to X-rays, which requires very thin liquid samples in high vacuum. Note that X-rays can obtain signal from tens of micrometers thick liquid samples which can be easily achieved by liquid jets or standard microfluidic setups.

One significant study with electrons reported by Lengyel and Kalman includes an environmental chamber to bring water into high vacuum. Even though they obtained diffraction from liquid water, they could keep the thickness of water layer applicable for <100 keV electrons only for a few seconds.[136] As we discussed earlier, the nanofluidic cell provides a fully closed system and stable sample thickness for sufficiently long time. However, SiN windows (~200x100 µm) suffer from excessive bulging in vacuum as discussed in Chapter 5. Therefore, we tried to reduce the sample thickness by controlling the pressure in both inlet and outlet tubes. We found that balancing the vacuum pressure by generating an under pressure (<1 atm) in the tubing thins down the liquid film and increase the SNR. The small dimensions of the nanofluidic system prevent fast evaporation of the solution under low pressure. We investigated the efficiency of this

method by our interferometer and found that it is possible to reduce the liquid film thickness to <1 μm for 200x100 μm wide windows. The details of this method will be discussed in the following chapter.

We measured the sample cell loaded with liquid water in our custom designed FED setup.[137] In the setup, the output of a commercial Ti:sapphire laser system (800 nm, 50 fs) is converted into 266 nm wavelength laser and impinges on a gold photocathode to generate electron pulses. Electrons are accelerated to 80 keV by a DC potential. The beam contains $\sim10^4$–$10^5$ electrons per pulse with pulse length of ~1 ps and a spot size of ~ 50 μm on the cathode. The diffracted electrons from the sample are focused with a magnetic lens and captured with a fiber-coupled CCD detector. A general description of the used setup is illustrated in Figure 3.1.

We first measured the empty nanocell to quantify the background signal originated from SiN. The window size and thickness are ~200x100 μm and 50 nm, respectively. The spacer thickness is ~100 nm.

It was mentioned that SiN windows used in the study are deposited by LPCVD method. Ammonia ($NH_3$) and dichlorosilane ($H_2SiCl_2$) were the typical precursors for the deposition process. It was reported that atomic composition of forming SiN film changes based on the ratio between the gases of $NH_3$ and $H_2SiCl_2$ in deposition. In the same report, it was found that when the $NH_3$:$H_2SiCl_2$ ratio is 3:1, the radial distribution curve of the resulting film corresponds well with the theoretical curve calculated from the crystalline model.[138] In the structure, silicon atom is surrounded by four nitrogen atoms and the distance between Si–N varies 1.7–1.8 Å due to a structural distortion. The bond angles of Si–N–Si and N–Si–N are 120º and 109º, respectively, which result Si–1st Si distance is similar to the N–1st N distance (2.97–3 Å). Therefore, the radial distribution function gives a broad and strong peak at around 3 Å.[138]

Figure 9.2 shows the diffraction pattern obtained from empty liquid cell (A), the same cell filled with water (B), and their difference image (C). The liquid cell was filled using a syringe pump (PHD Ultra, Harvard Apparatus) with a flow rate of 0.25-1 mL/hour. Figure 9.2 D shows the radial average of intensities as a function of s-values (*momentum transfer parameter* calculated by Eq. 9.1) from the diffraction center for the empty (red) and loaded (blue) liquid cell and (black) for the difference image. Before radial averaging, distortions in the diffraction images arising from the aberration in post-sample magnetic lens were corrected. The beam blocker was masked and the fractions containing artifacts were removed from the images before radial averaging (not shown in Figure 9.2).
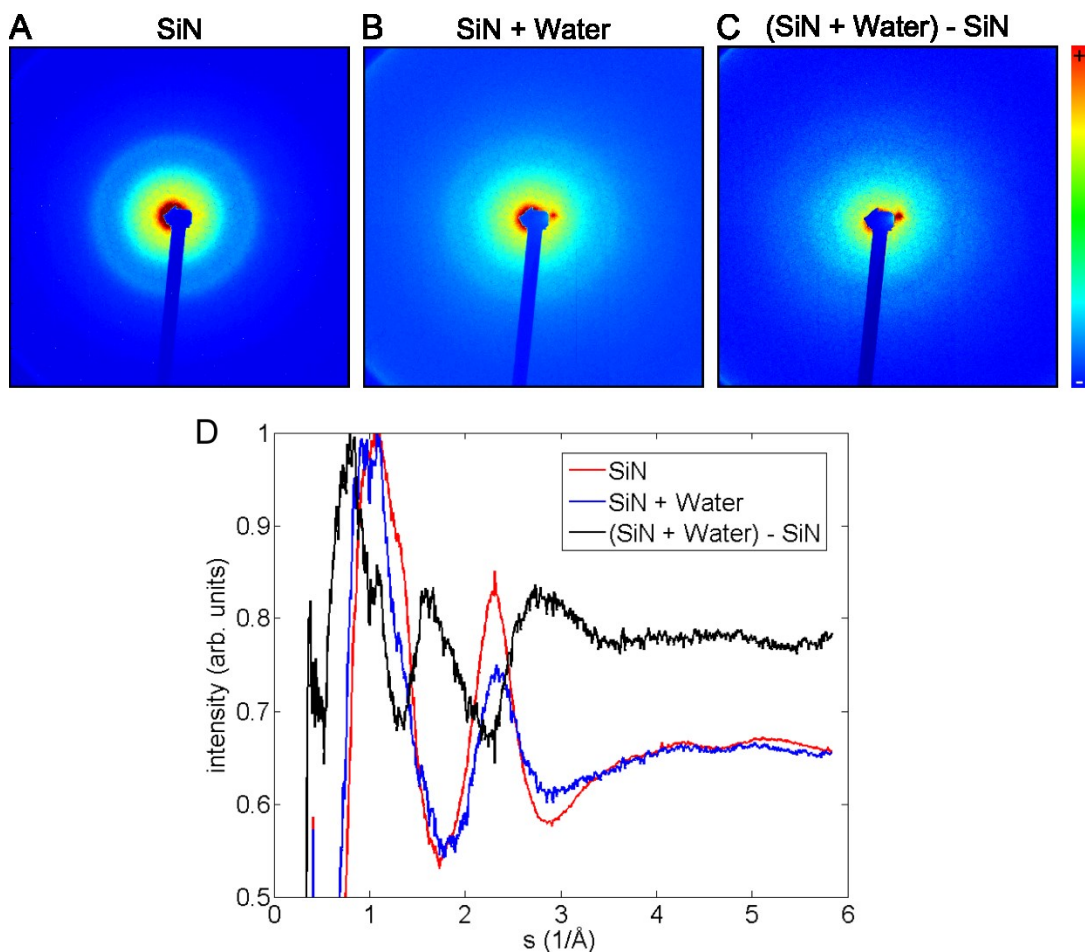
Figure 9.2. Diffraction patterns obtained from (A) empty and (B) water filled liquid cell and (C) their difference image. The images were taken with 1 s of exposure and accumulated 50 times. All the imaging parameters (electron energy, lens current, camera settings...etc.) were kept identical before and after loading of the liquid cell. (D) The radial average of the intensities as a function of s-values for all the images (A-C). The curves are normalized and background-corrected with a polynomial fitting. The distortions in the diffraction images originating from the magnetic lens are corrected in the radial averaging curves (D) but not in the images (A-C).

The electron beam is attenuated once the water enters the liquid cell, which causes a significant drop in the acquired intensities. In order to avoid negative intensities in the difference image, we multiply the pixel intensities of the image of (SiN + water) with a scaling factor so the lowest pixel value in the difference image becomes zero.

As shown in Figure 9.2 D, the most intense peak we observed in SiN at around 1.1 Å$^{-1}$ is shifting to a lower s-value once the water is introduced. This shift is clearer in the radially averaged curve of the difference image (Figure 9.2 D, black curve).

In order to assign the obtained signal (averaged intensity curves as a function pixel radius) to the interatomic distances, we followed a data analysis sequence, which is commonly applied to gas phase electron diffraction data.[139] The magnitude change in the momentum vectors between the incoming and scattered electrons, s-values, can be calculated with known scattering angle:

$$s = \frac{4\pi}{\lambda} \sin(\theta/2) \,, \tag{9.1}$$

where $\lambda$ is the Broglie wavelength of the electrons (0.0418 Å for 80 keV electron energy) and $\theta$ is the scattering angle between incident and scattered electrons. The scattering angle is given by:

$$\theta = \arctan(d/L) \,, \tag{9.2}$$

where $d$ is the distance on the detector plane relative to the center position, which can be calculated with known pixel size of the detector and $L$ is the distance from the sample plane to the detector, known as *camera length*. In order to calibrate the $L$, we used polycrystalline aluminum as a target with well-known crystalline structure obtained under the same conditions.

The modified molecular intensities, *sM(s)*, are obtained by rescaling the molecular scattering intensities, *$I_M(s)$,* with s. In order to calculate the *$I_M(s)$*, a background intensity curve corresponding to atomic scattering amplitude, *$I_A(s)$*, is subtracted from the total experimental intensities, *$I_T(s)$*. In order to calculate *$I_A(s)$*, a polynomial curve fitting is applied to the total scattering intensities. The *sM(s)* is given by:

$$sM(s) = s\frac{I_T(s)}{I_A(s)} \,. \tag{9.3}$$

In order to calculate the densities of interatomic distances in real space, the radial distribution function is calculated by transforming the *sM(s)* with a sine function, which is given by:

$$f(r) = \int_0^{S_{max}} sM(s) \sin(sr) \, exp(-ks^2)ds \,. \tag{9.4}$$

In order to avoid spurious signal arising from the finite size of the detector, the constant, *k*, known as damping coefficient is included and the sine transformation is performed up to the maximum s-value to avoid artifacts of finite data length.[139]

Figure 9.3 shows the total scattering intensities with a polynomial fit, the modified molecular intensity curve and the radial distribution curve (RDC) for empty liquid cell (top panel), the same liquid cell loaded with water (mid panel), and their difference image (lower panel). In the RDC of SiN, the peak obtained at 1.45 Å can be assigned to Si–N distance. The peak at 3.41 Å can have contributions from N–N, Si–Si and Sin–2$^{nd}$ Ni spacings.[138] The RDCs of the empty and water-filled liquid cell have similar peaks as seen in Figure 9.3; however, we observed a shift in the peak position to 3.14 Å in the water-filled liquid cell. This can be explained by the contribution of water with O···O distance at ~2.8 Å.[136] This is supported by the peak obtained at 2.4 Å in the RDC of the difference image (Figure 9.3, bottom-right).

Here it should be pointed that acquiring negative intensities in the difference image suggests that a fraction of the incoming beam is absorbed in the water-filled liquid cell due to multiple and inelastic scattering events. It requires a more elaborate analysis to obtain the contribution of these events in the total scatterings. Alternatively, obtaining a higher SNR increases the reliability of the analysis.

In this study, it was shown that FED with nanofluidic cell can allow studying the dynamics of H-bonding network of water in fast time scales. These unrevealed dynamics give water many unique properties.[135] In contrast to its X-ray and neutron counterparts, electrons can resolve the dynamics of pure water directly (model independent) without relying on highly debated theoretical studies and avoiding multiple interpretations of the same experimental results. [140] This leads to resolving the structure and function correlation of H-bonding network, which makes water the most anomalous and important liquid of life.

The nanofluidic cell with differential pressure control can be used for *in-situ* electron diffraction even for liquid water with low Z-contrast. Due to strong diffuse rings originating from 2 x 50 nm thick SiN windows  (overlapping with the signal originating from liquid water), we could not resolve O–H correlation, but only O···O interactions between neighboring water molecules, which can be attributed to the peaks obtained at 2.4 and 4.6 Å (Figure 9.3, bottom-right).[130] In order to reduce the contributions from the SiN windows and increase the SNR, thinner windows and higher electron energy are required.
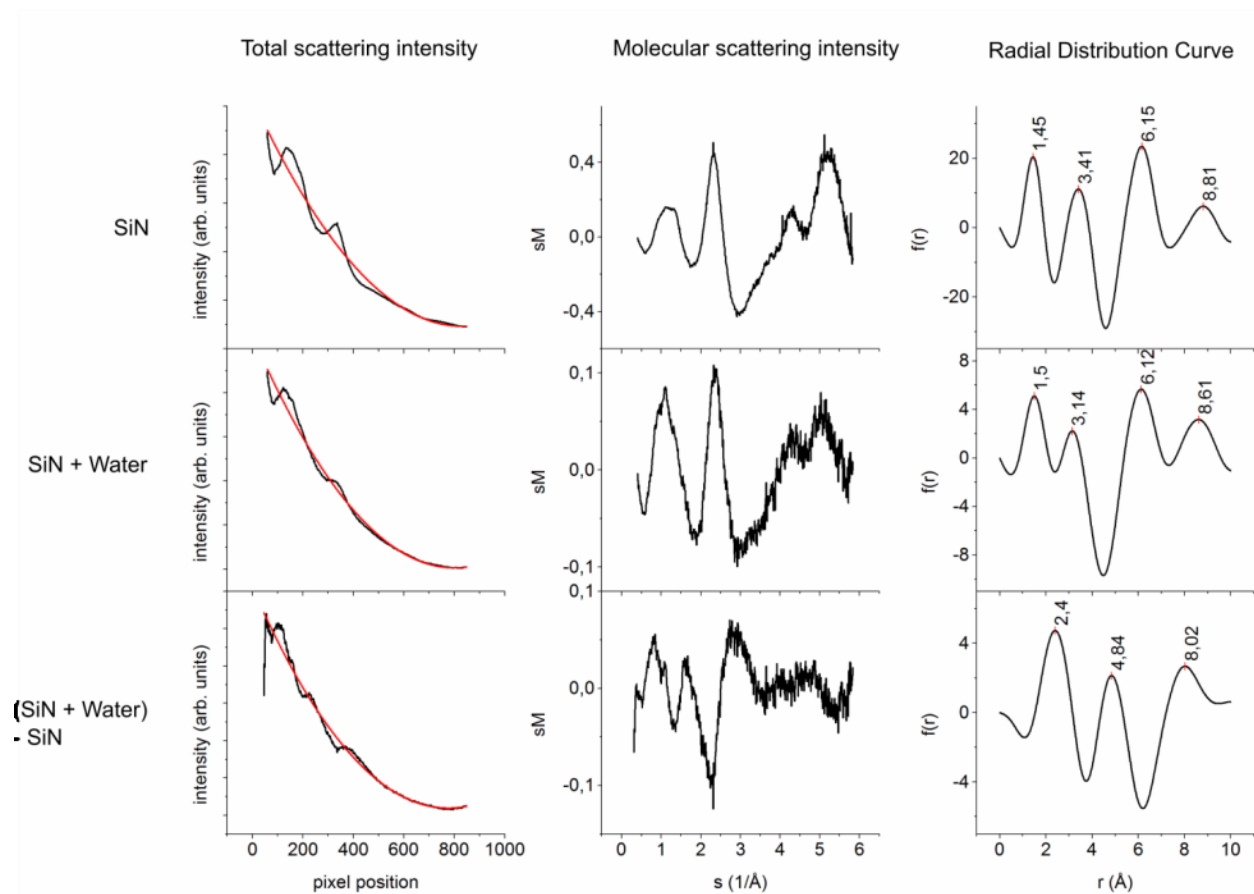
Figure 9.3. In-liquid electron diffraction of liquid water. From left to right: Total scattering intensity (black curve), atomic scattering intensity (red curve); molecular scattering intensity (sM) and radial distribution function (f(r)) obtained from the diffraction patterns of empty liquid cell (top), the same cell filled with water (middle) and the according difference image (bottom).

We repeated the same measurement with our MeV-range electron source (REGAE) at a much higher electron energy (5.2 MeV). We used a flow setup, which is almost identical with the one used at 80-keV electron source except the length of the tubing. The sample of liquid water was delivered into the beam path and the differential pressure method was implemented in the same fashion. Figure 9.4 shows the diffraction pattern obtained from empty liquid cell (A), the same cell filled with water (B), their difference image (C), and the molecular scattering curves calculated from each image.

The obtained Bragg spots originated from the silicon edge of the SiN windows are very clear in the image of unfilled nanocell and some of them are still visible in the image of the

88

water-filled one. This suggests a beam size that is larger than the aperture of the nanocell and a thin water layer qualitatively.

Note that the presented results obtained by REGAE here are preliminary and a more complete analysis including radial distribution curve will follow.
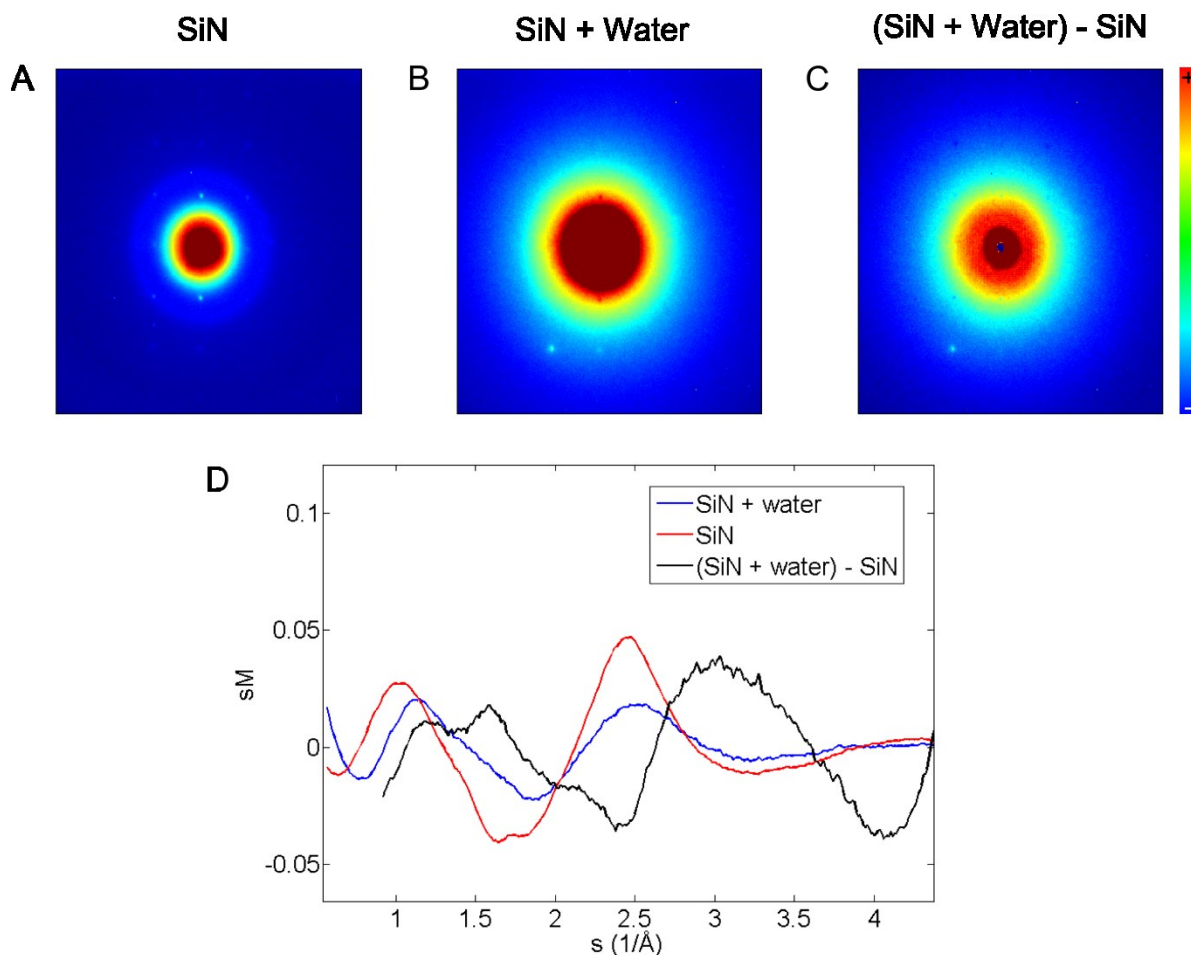


Figure 9.4. Diffraction patterns obtained from (A) empty and (B) water filled liquid cell and (C) their difference image. The image of SiN was taken with 30 s of exposure and accumulated 21 times and SiN+water was taken with 30 s of exposure and accumulated 10 times at an electron energy of 5.2 MeV. The charge of the electron beam was measured as 100 fC. The repetition rate of the electron beam generating laser is 12.5 Hz. All the imaging parameters were kept identical before and after loading of the liquid cell. (D) The molecular scattering curves of all the images (A-C).

## 9.1. Controlling the Thickness of the Liquid Film with Differential Pressure

The liquid film thickness can be controlled externally by generating an under pressure (< 1 bar) in the tubes to balance the vacuum pressure in the sample chamber. Figure 9.5 shows the schematic illustration of the flow system used. The process involves two stages. In stage one, the sample is loaded into the tubes and the nanocell by a syringe pump. In this step, valves 1-2 (V1 and V2) are kept open while the others are closed. Upon filling both inlet and outlet tubes, the outlet is blocked and the syringe is isolated from the flow system by closing V1 and V2, respectively. In stage two, the four valves, V3 to V6 are open to reduce the pressure in the tubes, which is monitored and simply adjusted with the valves, V5 and V6.
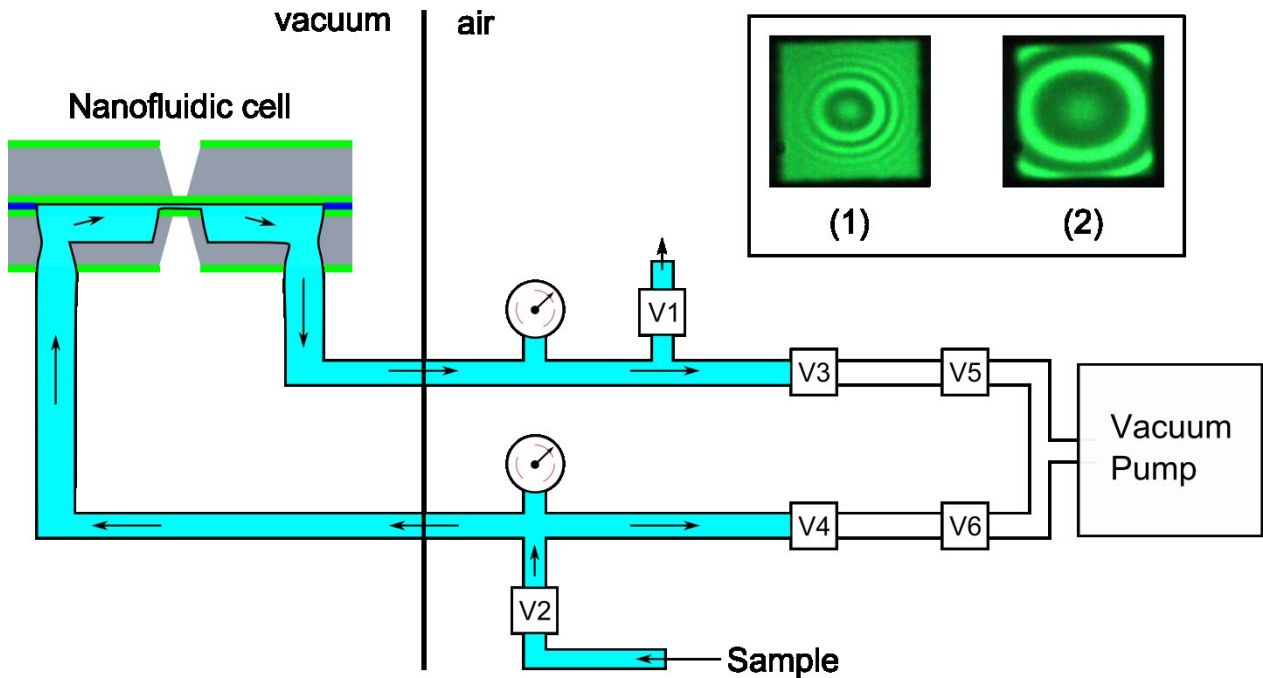


Figure 9.5. Schematic description of the flow system used to optimize the liquid film thickness in vacuum. The direction of the liquid flow is pointed by arrows. V1 to V6 represent the different plug valves in the setup. The window interference images during the loading (1) and thickness adjustment (2) are given as inset.

The measured interference images of the windows at stage one and two are given in Figure 9.5 as inset. As seen at stage one, during the loading of the cell, the windows are bulging normally. However, at stage two, the liquid thickness is reduced to ~0.63 μm for ~200x100 μm window size by considering three fringes in the window image. In the test, we could not equalize

the pressure in the chamber and in the tubes due to relatively small inner diameter of the liquid tubing and also additional liquid vapor pressure (for water, 23 mbar at 20 ºC). However, one can use a stronger pump for the tubes so it should be possible to obtain near flat windows in high vacuum by this method. Nevertheless, the presented method provided around one order of magnitude improvement in liquid film thickness using current generation nanofluidic cell. As a follow up study, we will test the same method on thinner and wider windows to optimize the conditions for the diffraction/imaging experiments.

We tested this differential pressure method for in-liquid TEM using citrate capped AuNPs with a dimeter of 20 nm. We simply casted 1-3 µL sample solution on the nanocell half and sealed it with the other identical half in the holder as described in previous chapters. Figure 9.6 shows in-liquid TEM images of citrate-AuNPs before (A) and after (B) evacuating the tubes and plot profile of the marked particle next to each image.
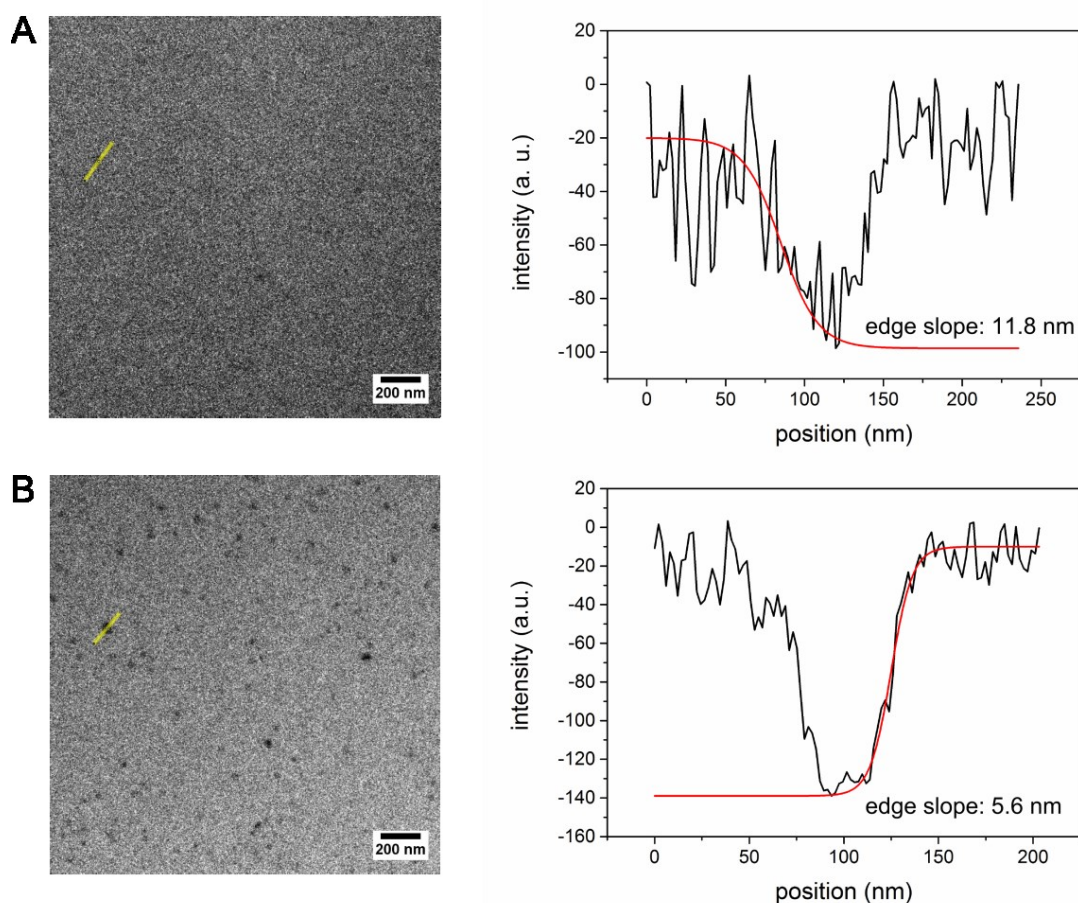
Figure 9.6 In-liquid TEM images of citrate-AuNPs before (A) and after (B) evacuating the tubes and the plot profile of the marked particle next to each image. The window dimension is 200x50 um.

We deliberately used large windows ($\sim$200x50 $\mu$m) to start with relatively low resolution before sample thickness adjustment. As seen in Figure 9.6 A, a few NPs with blurry edges are barely visible. As soon as the tubing is evacuated, the effect on the resolution evolves rapidly and much more NPs become visible with a better resolution (Figure 9.6 B). For a comparison, we extracted line profiles from the same NP before and after the thickness adjustment and we fitted the intensity drop in the line profiles with a Boltzmann function described in the previous chapter. Based on the edge analysis for multiple particles, we can suggest an improvement in the resolution of a factor of 2-3.

This method allows using larger window sizes without compromising the resolution. We are currently working on increasing the efficiency of this method by adjusting the parameters such as the differential pressure in the tubing or the total sample volume used. These parameters directly affect the evaporation rate of the sample, which defines the total observation time before the sample completely evaporates.

# 10.    Sample Preparation for FED using Ultramicrotomy

Microtomy is one of the conventional sample preparation methods for electron microscopy and diffraction. Ultramicrotomy, as an advanced subcategory of microtomy, is used for preparing thin-films of organic and inorganic crystals at ambient and cryogenic conditions. In this method, a fine diamond knife embedded into a reservoir (boat) is used to cut bulk crystals down to generally 20-200 nm thick sections. In room temperature sectioning, the reservoir is filled with water to allow cut sections floating on top of water. Then, floating sections are transferred onto suitable substrates such as standard TEM grids.

In this thesis study, a Leica U-7 Ultramicrotome was mainly used to section the crystals of $Me_4P[Pt(dmit)_2]_2$ ($Me_4P$ = tetramethylphosphonium, dmit = 1,3-dithiol-2-thione-4,5-dithiolate)[141], molybdenum disulfide ($MoS_2$), iridium telluride ($IrTe_2$), indium(III) selenide ($In_2Se_3$) and purely organic diphenylcyclopropenone (DPCP). Figure 10.1 shows a picture of the ultramicrotome (A) with zoom-in images of knife stage (B) and sample holder (C), a schematic illustration of the microtoming process and a picture of typical thin films on a standard copper mesh.

It is more challenging to section soft organic matter compared to inorganic crystals since the process can easily damage soft crystals or induce structural distortion in the cut thin-films. An example for this distortion is given in Figure 10.2 for $Me_4P[Pt(dmit)_2]_2$ crystals cut into <150 nm sections and placed on substrate. We usually used TEM grids with 1000 or 1500 mesh sizes as substrate. However, we found using an orientation fitting method that ultra-thin layer carbon (~3 nm) coated copper meshes provide a better support to the sample.  Therefore, we used samples on such grids for the FED experiments. Figure 10.2 shows a low-magnification TEM image of typical $Me_4P[Pt(dmit)_2]_2$ sections after microtoming (A) and a higher magnification image showing the microcrystalline domains. We found by TEM analysis that the structure of thin-film crystals was distorted by microtoming resulting microcrystallites, which appear as micron-sized domains separated by ripples. Despite the fact that microcrystalline formation changes the diffraction pattern significantly, we found that it was possible to model the disorder accurately by the orientation fitting method. We found excellent agreement between the simulation of the diffraction pattern including the disorder in the crystalline structure and the experimental data (Figure 10.3 C and D).
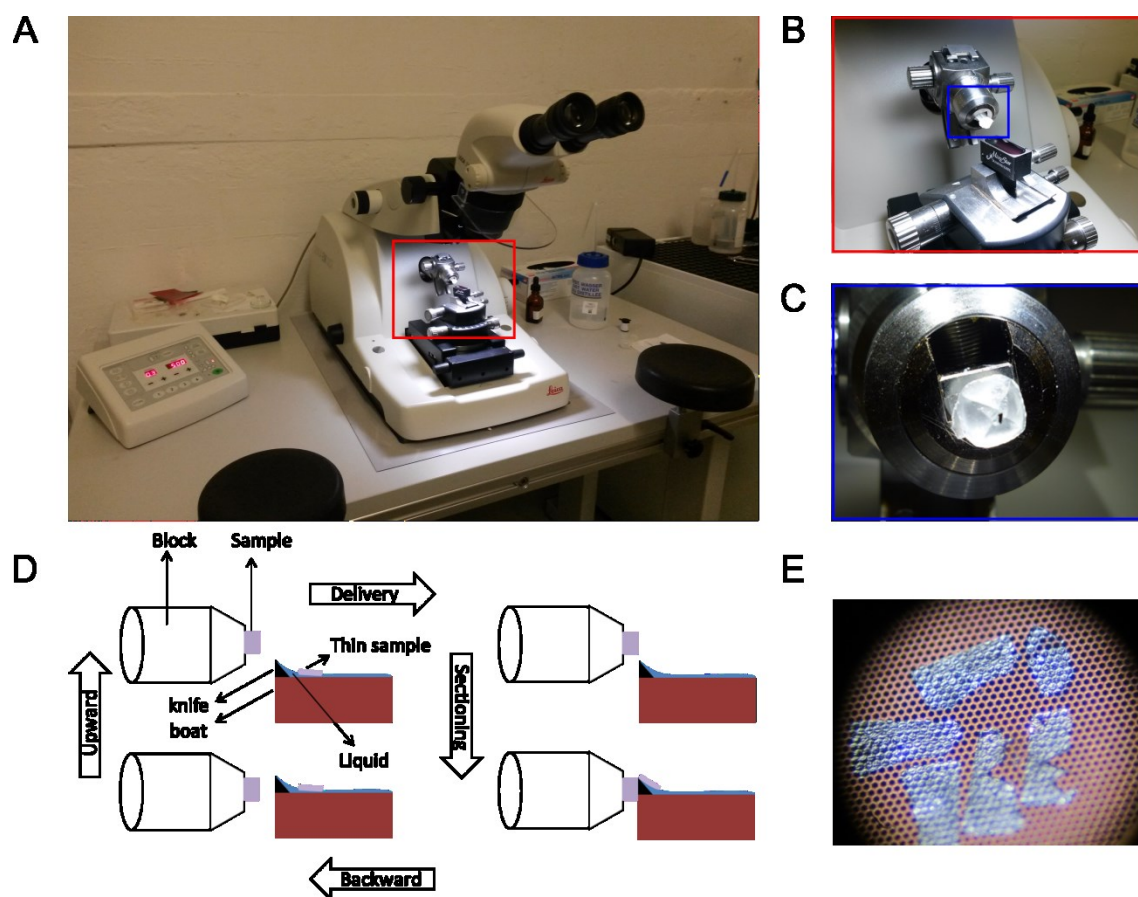
Figure 10.1. Ultramicrotome. (A) Picture of a Leica U7 Ultramicrotome. Zoom-in images of its (B) knife stage and (C) sample holder. (D) Schematic illustration of the microtoming process. (E) Picture of typical thin films on a standard copper mesh.

Me$_4$P[Pt(dmit)$_2$]$_2$ is a molecular system with a complex structure and relatively large unit cell size ($a$=28.9 Å, $b$=12.6 Å, $c$=37.4 Å at low temperature). In the crystal structure, each Me$_4$P cation accompanies two Pt(dmit)$_2$ molecules (Figure 10.2 B). It exhibits a photoinduced phase transition (PIPT) from charge-separated (CS) phase (low temperature phase) to metallic phase (high temperature phase) similar to that induced by temperature (transition temperature 218 K). In the CS phase, four crystallographically independent dimers of Pt(dmit) form, as being different than the crystalline structure at metallic phase.
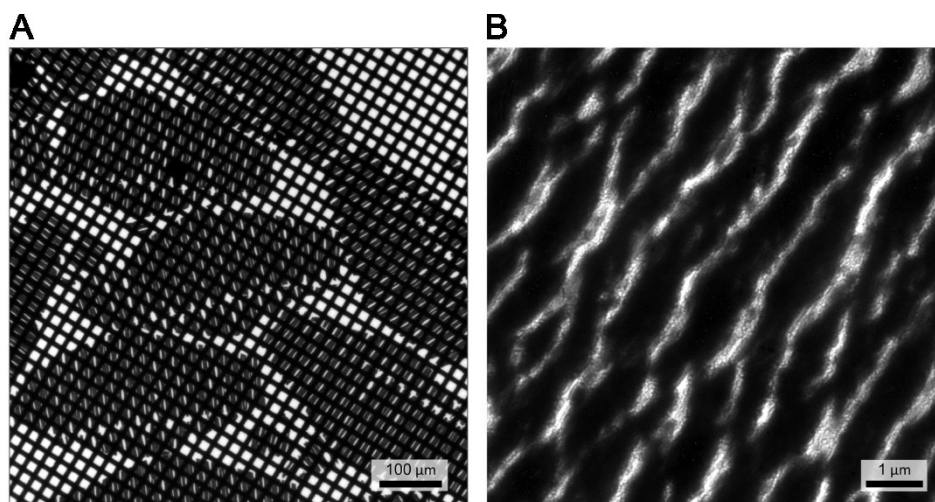
Figure 10.2. TEM bright-field images of typical Me4P[Pt(dmit)2]2 samples after microtoming. (A) Low-magnification image showing multiple cut samples, (B) higher magnification showing the microcrystalline domains. The images were acquired using a Philips/FEI CM-12 microscope operating at 80 kV. (Taken from reference-141)

The dimers in the CS phase can be categorized into two groups based on the Pt–Pt distances between the molecules. One group of molecules are neutral with a Pt–Pt distance of 2.93 Å (neutral dimers) and other group has a charge of –2 and a Pt–Pt distance of 3.31 Å (divalent dimers). Charge separation among the dimers results them ordering like a checkerboard and consequent doubling of the unit cell along both the *a* and *b* axes.

Figure 10.3 shows a diffraction image of $Me_4P[Pt(dmit)_2]_2$ at 90 K (CS phase) recorded at an acceleration voltage of 110 kV (C), simulated diffraction pattern with marked Miller indices (D) and thermal phase transition assuming a fixed unit cell (E). Figure 10.3 F shows the time-resolved FED analysis performed with an excitation pulse at a wavelength of 800 nm and a repetition rate of 250 Hz. The images showing the averaged intensity differences at selected time points ($I^{laser\ on}(t) - I^{laser\ off}$) are given with the associated molecular motions for neutral dimers under each image in Figure 10.3 F. Figure 10.3 G and H show the relative intensity changes for the selected diffraction spots as a function of delay time and the intermolecular S··S distance for neutral and divalent dimers, respectively.
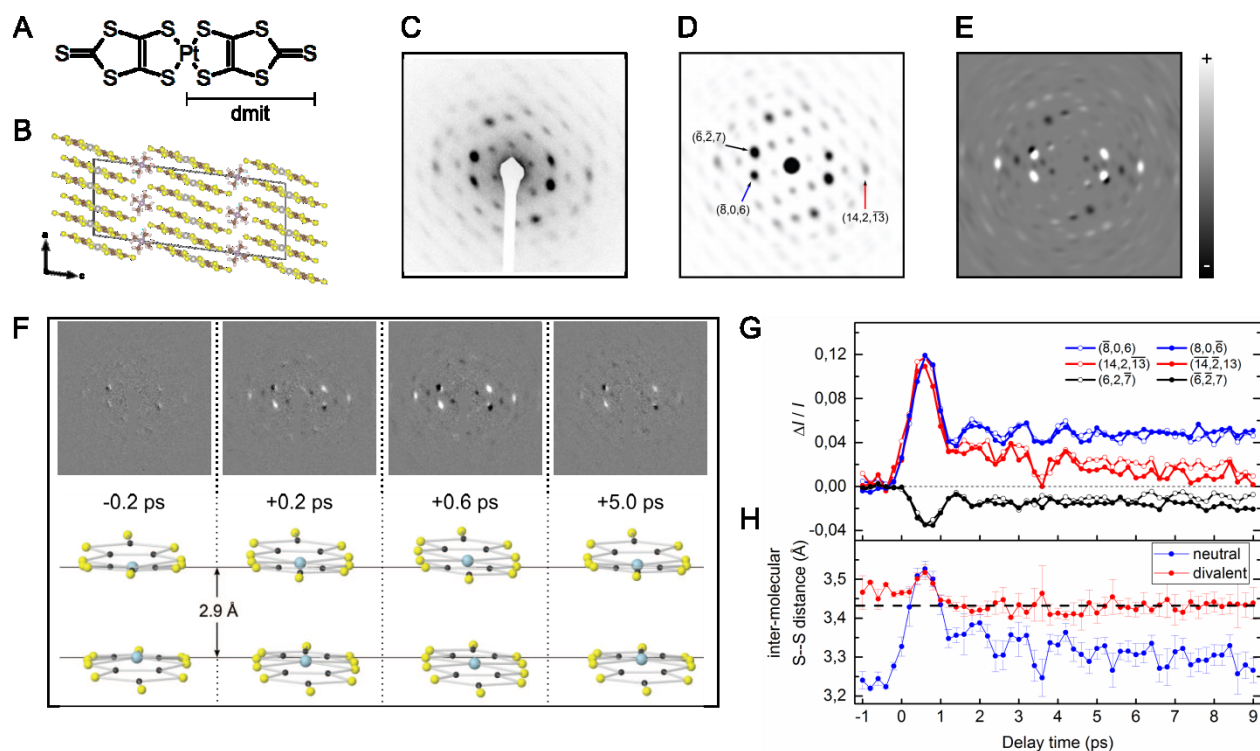
Figure 10.3. Femtosecond electron diffraction on single crystalline $Me_4P[Pt(dmit)_2]_2$. (A) Chemical structure of $Pt(dmit)_2$, (B) crystal structure of $Me_4P[Pt(dmit)_2]_2$ viewed along *b* axis, (C) experimental diffraction pattern at 90 K, (D) simulated diffraction pattern with marked Miller indices, (E) difference between the simulated diffraction patterns for low and high temperature phases, (F) time-resolved FED data at selected time points relative to the laser excitation and associated molecular dynamics, (G) relative intensity changes for the selected diffraction spots as a function of delay time, (H) intermolecular S··S distance for neutral and divalent dimers. (Adapted from reference-141)

As seen in Figure 10.3 F, there is no obvious difference between only probe and the probe immediately after the photoexcitation (-0.2 ps). However, the differential intensity of the peaks at +0.2 to +0.6 ps is significantly high and also exhibits a remarkable resemblance to the simulated thermal difference pattern (Figure 10.3 E). This indicates that the photoinduced structure change is similar to the one observed transition between low and high temperatures as anticipated from the optical studies.[142]

The positions of the individual atoms were found using a minimization function considering known chemical structures for the CS and metal-like phases and the obtained FED

data. The key importance of this study is the large unit cell size of $Me_4P[Pt(dmit)_2]_2$ crystals and a unique approach to construct the ultrafast structural dynamics allowing an atomic-level picture of the dynamics on the sub-picosecond time scale to be produced.

Besides $Me_4P[Pt(dmit)_2]_2$, the thin-films of iridium telluride ($IrTe_2$), indium(III) selenide ($In_2Se_3$), molybdenum disulfide ($MoS_2$), and organic diphenylcyclopropenone (DPCP) were prepared with ultramicrotomy. Figure 10.4 shows the static diffraction patterns of these compounds obtained by different electron diffraction setups.
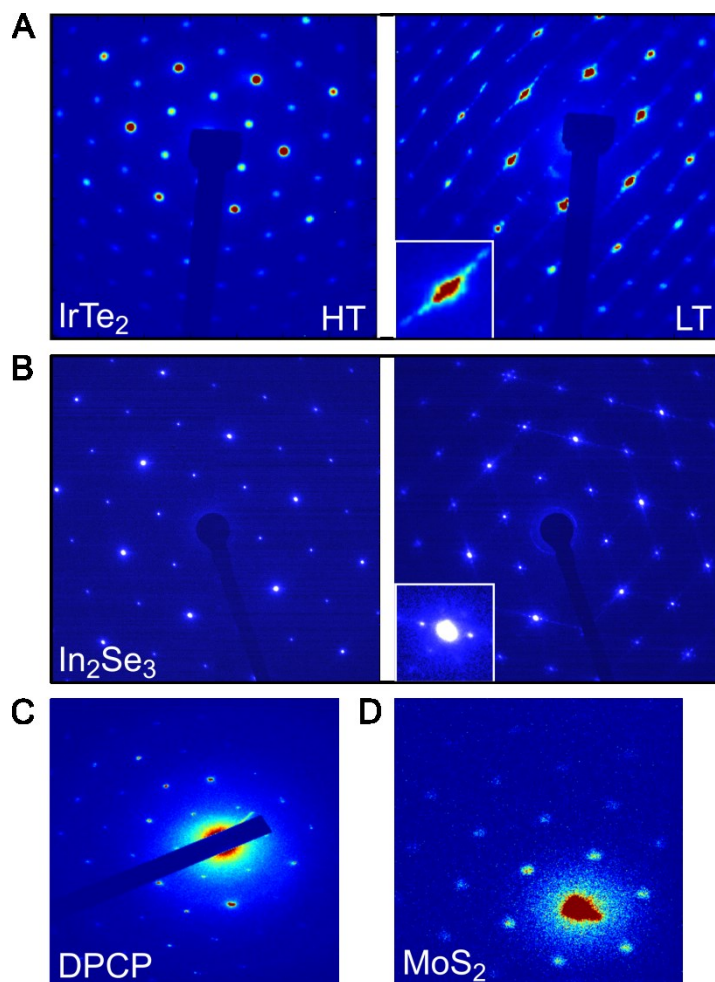


Figure 10.4. Diffraction patterns of (A) $IrTe_2$ in high (HT, ~300 K) and low temperatures (LT, ~200 K). (B) $\alpha$-$In_2Se_3$ (Superlattice peaks are visible in the image on the right). (C) DPCP and (D) $MoS_2$. The films thicknesses are 30-100 nm. Inset figures in A and B highlight the superlattice peaks observed around and in between the more intense Bragg peaks.

IrTe$_2$ is a highly interesting system to investigate the correlation between the structural phase transition and charge ordering. It is a layered material and shows a different structural/electronic transition than well-known CDW (charge density wave)-like transition, at low temperature (LT: <260-270 K). It was reported that the charge ordering in the LT phase results Ir-dimerisation and/or polymerization of Te chains and consequent shortening of the Ir-Ir and Te-Te bonds.[143,144] We performed time-resolved FED on 20-100 nm thick sections of IrTe$_2$ crystals with an optical excitation to observe the photoinduced atomic motions governing the phase transition. Figure 10.4 A shows the diffraction patterns obtained from 40 nm thick sample in HT and LT phase. The diffraction pattern has a six-folded symmetry and superlattice peaks between the Bragg peaks appear in LT phase. The relative intensity change between Bragg and superlattice peaks indicate that the photoexcitation suppresses the lattice distortion and enhances the symmetry in the crystalline structure by redistributing the electron density. The observed dynamics can be explained with the aid of DFT (density functional theory) calculations as follows: Upon photoexcitation, the sample's electrons go to the d$_{xy}$ antibonding state and this breaks the dimerization. Dimerization recovers when the electron population in this antibonding state is reduced by electron-electron scattering and following electron-phonon interactions at a time scale of 5 to 10 ps. This study is in the stage of manuscript preparation.

In$_2$Se$_3$ is an important thermoelectric material that can directly convert thermal energy into electrical energy for generally ion battery and photovoltaic solar cell applications[145]. It has five known crystalline forms ($\alpha$, $\beta$, $\gamma$, $\delta$, $\kappa$). The $\alpha$- and $\beta$-forms are common and have a layered crystalline structure. In the structure of $\alpha$-In$_2$Se$_3$, In and Se atoms are covalently bonded and neighboring layers are bonded by van der Waals interactions[145]. It was reported that exfoliated $\alpha$-In$_2$Se$_3$ nanosheets show higher photoresponsivity compared to the photodetectors on graphene.[146]

We used 30 nm thick microtomed sections for TEM measurement. Figure 10.4 B shows the diffraction images obtained from $\alpha$-In$_2$Se$_3$. We clearly observed the superlattice[145] peaks around the Bragg peaks in some patches of even the same section. The major indication of the phase transition in $\alpha$-In$_2$Se$_3$ is the relative intensity change in the Bragg and superlattice peaks. The physical properties of indium selenide are mainly determined by its stoichiometry, crystal structure, and phase. In order to manipulate its properties such as enhancing the thermoelectric efficiency, it is important to investigate the structural phase transition in atomic level. For this purpose, we performed photoinduced FED on $\alpha$-In$_2$Se$_3$. We clearly distinguished the electronic

and thermally driven phase changes, which happened on a time scale of 1ps and 300 ps, respectively.

Figure 10.4 C shows a diffraction pattern obtained from DPCP. First, we should highlight two important optical studies on DPCP. It was reported that photoexcitation with 267 nm induce decarbonylation of DPCP and it forms DPA (diphenylacetylene) both in solid[147] and solution state[148] (Figure 10.5).   Takeuchi and Tahara studied the photoinduced reaction dynamics of DPCP in solution with time-resolved absorption spectroscopy in subpicosecond regime.[148] In their transient absorption spectra, they assigned 480-nm band with 0.2 ps life time to excited state of DPCP (initially populated $S_2$ state). They obtained two broad peaks at 430 nm and 700 nm, which are both assigned to $S_1$ state of DPA at 30 ps relative to the photoexcitation. The system further relaxes by forming $T_1$ DPA at 200 ps by intersystem crossing. In order to reveal coherent nuclear dynamics of the photodissociation, they focused on the fast components of the spectra and suggested that DPA is produced in its $S_2$ excited state and it undergoes to $S_1$ state via internal conversion. Based on the data and the DFT calculations, they suggested a large displacement in the C=O group and a deformation in the Ph–C=C–Ph group that are driving the photodissociation.[148] Doan et al. investigated the nanocrystalline form of DPCP in water using a liquid jet. They also used transient absorption spectroscopy and suggested that photodissociation leaves high amount of energy in DPA and this energy initiates a quantum chain reaction (QCR) by exciting the nearby DPCP molecules in solid state.[147] As seen, decarbonylation of DPCP is a very interesting process and the full dynamic picture of this structural transition is missing. Therefore, we prepared the thin films of DPCP crystals by microtoming for FED experiments. We first characterized the diffraction pattern with TEM (JEOL JEM-2100) at 200 kV, as shown in Figure 10.4 C.
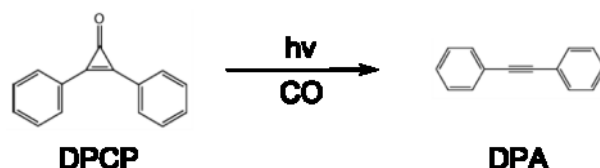


Figure 10.5. Photodissociation of DPCP yielding DPA and carbon monoxide.

Here it should be noted that the high vacuum conditions destroys the structural integrity of the DPCP crystals. Therefore, the sample is isolated from the vacuum in between two

commercially available SiN grids glued at the edge. This study is in the sample preparation stage and time-resolved FED analysis will follow.

Figure 10.4 D shows the diffraction pattern obtained from inorganic crystal $MoS_2$. It is shown to illustrate the diffraction quality obtained by our MeV-range electron source (REGAE).[13]

# 11.    Conclusion and Prospect

In this work, we demonstrated the nanofluidic cell as an excellent tool for studying the structure and dynamics of nanomaterials, biomolecules and organisms in natural liquid environment with nanometer spatial resolution. Tapered reservoirs of the cell reduce the high flow resistance area and allow using high flow rate with a reasonable internal pressure.[66] Using high flow speed leads to fast sample exchange and thusly ultrashort electron pulses can continually hit fresh sample during a pump-probe experiment.

Silicon nitride is a very rigid material and relatively easy to process. As an example, 50 nm thick 200 μm x 100 μm wide membranes can hold a pressure difference of >4 bars as tested using $N_2$ gas. However, SiN shows a high absorption in UV region, which is problematic to photoexcite mainly organic compounds. Also, SiN as an amorphous material gives diffuse and broad rings in its diffraction pattern, which overlap with the diffuse rings originating from liquid samples. This makes it difficult to subtract the contribution of SiN from the total scattered intensities. Instead of SiN, single crystalline silicon or diamond windows can be used. Single crystals gives distinct Bragg spots in their diffraction patterns, which can easily be subtracted from amorphous diffraction pattern of liquid samples. Shchepetov et al. fabricated single crystal, flat Si membranes with a thickness of 6 nm using SOI (silicon-on-insulator) wafers and by controlling the strain with an additional SiN film.[149] However, mechanical stability of these materials in vacuum must be considered before fabrication.

The SiN window size of <15 μm reduces the bulging and keeps the liquid sample thickness less than 500 nm in vacuum as shown with thin film interferometry. The SiN windows supported with a grid pattern (for this case, it is a honeycomb pattern with 10 μm wide hexagons separated with 7-10 μm bars) provides large viewing area and a liquid thickness of ~170 nm due to the bulging of the SiN windows. In the next generation design, thinner SiN windows can be used to reduce the scattering from the windows and narrower support bars to further increase the viewing area.

In order to decrease the minimum sample quantity for flow cell, a micropump (electrostatic or electro-osmotic as the driving force) integrated into the liquid cell can be used. This will also lead to have a better control on the flow conditions since the sample volume will be decreased. However, including such a device into the liquid specimen holder is not trivial because of the limited space in the holder.

In this thesis work, we used static nanocells and investigated the hybridization dynamics of DNA using AuNP labels. This study demonstrated the first steps of watching DNA as it functions in its natural environment. It was shown that DNA maintains its structural integrity under electron beam exposure and can undergo hybridization with complementary strands. With the developments in sample preparation methods and electron source technologies, it will lead to direct observation of DNA duplex formation (helix nucleation and elongation), random changes in DNA conformation (and transitions between known conformations) and its interactions with other molecules in solution. In general, it will shed light on the biophysics of DNA.

New camera technology with two order of magnitude faster read out speed is under development in our group. This will help reducing the motion blur, consequently gaining in spatial resolution, which leads to observing single-molecule trajectories in solution. It is extremely valuable to track single molecules especially in living systems in order to eliminate ensemble averaging of motions, but reveal irregular diffusion processes (ergodicity-breaking dynamics) with high spatiotemporal resolution.[150,151] This can be achieved by electrons in a label-free fashion without using short-lived fluorescent reporters that generally interfere with the dynamics of interest.

In order to avoid heat deposition and ionization in the sample, a pulsed electron beam must be used instead of a continuous flux of electrons. This can be achieved either by using a laser triggered source or a mechanical shutter to give sample a relaxation time between consecutive shots. With these developments, the sample can be hit by short but very bright electron pulses and more information can be gained while decreasing the radiation damage and beam induced artifacts. It can also be suggested that operating the TEM in pulse mode reduces the charging of the SiN windows. In order to further reduce this effect, an ultra-thin layer of conducting material (such as single layer of graphene) can be transferred or directly grown onto the SiN windows.

We imaged mammalian cancer cells with in-liquid TEM using liquid cells with a spacer thickness of <1 μm. This led us achieve a resolution of <10 nm within the cells, which is higher than the one obtained with fluorescent based optical methods. As a follow up study, we will be working on observing real-time endocytosis of AuNP tagged aptamers into the cancerous cells. The viability of mammalian cells during *in situ* imaging with electrons (the onset and the level of the radiation damage for a particular electron dose) is currently under debate. In order to conclude this discussion, the cells could be recovered after the imaging and an according viability

test could be applied. However, recovering the adherent cells from the liquid cell can easily rupture the cell membranes, especially for mammalian cells without cell walls. An alternative and much more informative approach is to watch cell division, which is the certain proof of viability, real time with in-liquid TEM. This is one of the major future prospects of this study.

We have also shown that the nanofluidic cell can be used to study liquid water with electrons. The relatively high scattering cross section of electrons can obtain diffraction signal even from hydrogen and allows one to investigate the dynamics of H-bond network in water on time scales of femtoseconds, if a sufficient SNR is achieved depending mostly on the nanocell specifications and flow conditions. This will provide a new insight into the H-bond network and will not only contribute to solving the mystery of the key compound of life, but also answer many open questions in biochemistry as water is always present as the solvent (e.g. protein stability and function).

The combination of FED and the nanofluidic cell is an excellent tool to study solution phase chemistry on the time scales of femtosecond and length scales of angstrom. This will improve our understanding on far-from equilibrium motions that drive chemical changes and provide an atomic level perspective of structural phase transitions in solution phase. Such level of understanding of chemistry will give rise to more comprehensive explanations for the functionality of complex systems, e.g. enzymatic activity of proteins.

# 12.    References

1.    Sciaini, G. & Miller, R. J. D. Femtosecond electron diffraction: heralding the era of atomically resolved dynamics. *Reports Prog. Phys.* **74,** 096101 (2011).

2.    Miller, R. J. D. Electrons, U. Femtosecond Crystallography with Capturing Chemistry in Action. Science **394,** 386–394 (2011).

3.    Tavernier, S. *Experimental techniques in nuclear and particle physics. Experimental Techniques in Nuclear and Particle Physics* (2010). doi:10.1007/978-3-642-00829-0

4.    Weierstall, U. Liquid sample delivery techniques for serial femtosecond crystallography. *Phil Trans R Soc B* **369,** 20130337 (2014).

5.    Kim, K. H. *et al.* Direct observation of bond formation in solution with femtosecond X-ray scattering. *Nature* **518,** 385–389 (2015).

6.    Kim, J. G., Kim, T. W., Kim, J. & Ihee, H. Protein Structural Dynamics Revealed by Time-Resolved X-ray Solution Scattering. *Acc. Chem. Res.* **48,** 2200–2208 (2015).

7.    Williams, D. B. & Carter, C. B. *Transmission Electron Microscopy: A Textbook for Materials Science. Materials Science* **V1-V4,** (2009).

8.    Jean-Ruel, H. *et al.* Femtosecond dynamics of the ring closing process of diarylethene: A case study of electrocyclic reactions in photochromic single crystals. *J. Phys. Chem. A* **115,** 13158–13168 (2011).

9.    Gao, M. *et al.* Mapping molecular motions leading to charge delocalization with ultrabright electrons. *Nature* **496,** 343–346 (2013).

10.    Reed, B. W. *et al.* The evolution of ultrafast electron microscope instrumentation. *Microsc. Microanal.* **15,** 272–281 (2009).

11.    Evans, J. E. & Browning, N. D. Enabling direct nanoscale observations of biological reactions with dynamic TEM. *J. Electron Microsc. (Tokyo).* **62,** 147–156 (2013).

12.    Search, H., Journals, C., Contact, A., Iopscience, M. & Address, I. P. Low energy electron microscopy. **895,** (1994).

13.    Manz, S. *et al.* Mapping atomic motions with ultrabright electrons: towards fundamental limits in space-time resolution. *Faraday Discuss.* **177,** 467–491 (2015).

14.    Musumeci, P. *et al.* Laser-induced melting of a single crystal gold sample by time-resolved ultrafast relativistic electron diffraction. Appl. Phys. Lett. **063502,** (2013).

15.    Reimer, L. & Kohl, H. *Transmission Electron Microscopy Physics of Image Formation.*

*Springer series in optical sciences* **51,** (2008).

16. Knoll, M. & Ruska, E. Das Elektronenmikroskop. *Zeitschrift fur Phys.* **79,** 699 (1932).

17. Siwick, B. J. An Atomic-Level View of Melting Using Femtosecond Electron Diffraction. *Science (80-. ).* **302,** 1382–1385 (2003).

18. LaGrange, T. *et al.* Nanosecond time-resolved investigations using the in situ of dynamic transmission electron microscope (DTEM). *Ultramicroscopy* **108,** 1441–1449 (2008).

19. Browning, N. D. *et al.* Recent developments in dynamic transmission electron microscopy. *Curr. Opin. Solid State Mater. Sci.* **16,** 23–30 (2012).

20. Haider, M., Uhlemann, S., Schwan, E., Rose, H. & Kabius, B. Electron microscopy image enhanced. *Nature* **392,** 768–769 (1998).

21. Haider, M., Hartel, P., Müller, H., Uhlemann, S. & Zach, J. Current and future aberration correctors for the improvement of resolution in electron microscopy. *Philos. Trans. A. Math. Phys. Eng. Sci.* **367,** 3665–82 (2009).

22. Hanne, J. *et al.* STED nanoscopy with fluorescent quantum dots. *Nat. Commun.* **6,** 7127 (2015).

23. Willig, K. I., Rizzoli, S. O., Westphal, V., Jahn, R. & Hell, S. W. STED microscopy reveals that synaptotagmin remains clustered after synaptic vesicle exocytosis. *Nature* **440,** 935–939 (2006).

24. Huang, B., Wang, W., Bates, M. & Zhuang, X. Three-Dimensional Super-Resolution Reconstruction Microscopy. *Science (80-. ).* **319,** 810–813 (2008).

25. Cherry, S. R., Sorenson, J., Phelps, M. E. & Methé, B. M. *Physics in Nuclear Medicine*. *Medical Physics* **31,** (2004).

26. Manson, S. T. Dependence of the Phase Shift on Energy and Atomic Number for Electron Scattering by Atomic Fields. Phys. Rev. **182**, 97 (1969).

27. Danev, R. & Nagayama, K. Transmission electron microscopy with Zernike phase plate. *Ultramicroscopy* **88,** 243–252 (2001).

28. Danev, R., Buijsse, B., Khoshouei, M., Plitzko, J. M. & Baumeister, W. Volta potential phase plate for in-focus phase contrast transmission electron microscopy. *Proc. Natl. Acad. Sci. U. S. A.* **111,** 15635–40 (2014).

29. Nagayama, K. & Danev, R. Phase-plate electron microscopy: A novel imaging tool to reveal close-to-life nano-structures. *Biophys. Rev.* **1,** 37–42 (2009).

30. Grandfield, K. & Engqvist, H. Focused Ion Beam in the Study of Biomaterials and

Biological Matter. *Adv. Mater. Sci. Eng.* 841961 (2012). doi:10.1155/2012/841961

31. Kato, N. I. Reducing focused ion beam damage to transmission electron microscopy samples. *J. Electron Microsc. (Tokyo).* **53,** 451–458 (2004).

32. Giannuzzi, L. a. & Stevie, F. a. A review of focused ion beam milling techniques for TEM specimen preparation. *Micron* **30,** 197–204 (1999).

33. Burrows, N. D. & Penn, R. L. Cryogenic transmission electron microscopy: aqueous suspensions of nanoscale objects. *Microsc Microanal* **19,** 1542–1553 (2013).

34. Strunk, K. M., Wang, K., Ke, D., Gray, J. L. & Zhang, P. Thinning of large mammalian cells for cryo-tem characterization by cryo-fib milling. *J. Microsc.* **247,** 220–227 (2012).

35. Fukuda, Y. & Nagayama, K. Zernike phase contrast cryo-electron tomography of whole mounted frozen cells. *J. Struct. Biol.* **177,** 484–489 (2012).

36. de Jonge, N. & Ross, F. M. Electron microscopy of specimens in liquid. *Nat. Nanotechnol.* **6,** 695–704 (2011).

37. Kirk, S. E., Skepper, J. N. & Donald, a M. Application of environmental scanning electron microscopy to determine biological surface structure. *J Microsc* **233,** 205–224 (2009).

38. Stokes, D. J. *Principles and Practice of Variable Pressure/Environmental Scanning Electron Microscopy (VP-ESEM). Principles and Practice of Variable Pressure/Environmental Scanning Electron Microscopy (VP-ESEM)* (2008). doi:10.1002/9780470758731

39. Zhu, G. *et al.* Atomic resolution liquid-cell transmission electron microscopy investigations of the dynamics of nanoparticles in ultrathin liquids. *Chem. Commun.* **49,** 10944 (2013).

40. Evans, J. E., Jungjohann, K. L., Browning, N. D. & Arslan, I. Controlled growth of nanoparticles from solution with in situ liquid transmission electron microscopy. *Nano Lett.* **11,** 2809–2813 (2011).

41. Park, J. *et al.* Direct observation of nanoparticle superlattice formation by using liquid cell transmission electron microscopy. *ACS Nano* **6,** 2078–2085 (2012).

42. Williamson, M. J., Tromp, R. M., Vereecken, P. M., Hull, R. & Ross, F. M. Dynamic microscopy of nanoscale cluster growth at the solid–liquid interface. *Nat. Mater.* **2,** 532–536 (2003).

43. Zheng, H., Mirsaidov, U. M., Wang, L. W. & Matsudaira, P. Electron beam manipulation

of nanoparticles. *Nano Lett.* **12,** 5644–5648 (2012).

44. Zheng, H. *et al.* Observation of Single Colloidal Platinum Nanocrystal Growth Trajectories. *Science (80-. ).* **324,** 1309–1312 (2009).

45. Grogan, J. M. & Bau, H. H. The Nanoaquarium: A Platform for In Situ Transmission Electron Microscopy in Liquid Media. *J. Microelectromechanical Syst.* **19,** 885–894 (2010).

46. Keskin, S. *et al.* Visualization of Multimerization and Self-Assembly of DNA-Functionalized Gold Nanoparticles Using In-Liquid Transmission Electron Microscopy. *J. Phys. Chem. Lett.* 4487–4492 (2015). doi:10.1021/acs.jpclett.5b02075

47. Jiang, Y. *et al.* In situ study of oxidative etching of palladium nanocrystals by liquid cell electron microscopy. *Nano Lett.* **14,** 3761–3765 (2014).

48. Liu, Y., Lin, X.-M., Sun, Y. & Rajh, T. In Situ Visualization of Self-Assembly of Charged Gold Nanoparticles. *J. Am. Chem. Soc.* **135,** 3764–3767 (2013).

49. Mueller, C., Harb, M., Dwyer, J. R. & Miller, R. J. D. Nanofluidic cells with controlled pathlength and liquid flow for rapid, high-resolution in situ imaging with electrons. *J. Phys. Chem. Lett.* **4,** 2339–2347 (2013).

50. Proetto, M. T. *et al.* Dynamics of Soft Nanomaterials Captured by Transmission Electron Microscopy in Liquid Water. *J. Am. Chem. Soc.* **136,** 1162–1165 (2014).

51. Mirsaidov, U. M., Zheng, H., Casana, Y. & Matsudaira, P. Imaging Protein Structure in Water at 2.7 nm Resolution by Transmission Electron Microscopy. *Biophys. J.* **102,** L15–L17 (2012).

52. Cameron Varano, A. *et al.* Visualizing virus particle mobility in liquid at the nanoscale. *Chem. Commun.* **51,** 16176–16179 (2015).

53. Ross, F. M. Opportunities and challenges in liquid cell electron microscopy. *Science (80-. ).* **350,** aaa9886–aaa9886 (2015).

54. Chen, Q. *et al.* 3D motion of DNA-Au nanoconjugates in graphene liquid cell electron microscopy. *Nano Lett.* **13,** 4556–4561 (2013).

55. Wang, C., Qiao, Q., Shokuhfar, T. & Klie, R. F. High-Resolution Electron Microscopy and Spectroscopy of Ferritin in Biocompatible Graphene Liquid Cells and Graphene Sandwiches. *Adv. Mater.* **26,** 3410–3414 (2014).

56. Algara-Siller, G. *et al.* Square ice in graphene nanocapillaries. *Nature* **519,** 443–445 (2015).

57. Park, J. *et al.* Direct Observation of Wet Biological Samples by Graphene Liquid Cell Transmission Electron Microscopy. *Nano Lett.* **15,** 4737–4744 (2015).

58. Wojcik, M., Hauser, M., Li, W., Moon, S. & Xu, K. Graphene-enabled electron microscopy and correlated super-resolution microscopy of wet cells. *Nat. Commun.* **6,** 7384 (2015).

59. Helmersson, U., Lattemann, M., Bohlmark, J., Ehiasarian, A. P. & Gudmundsson, J. T. Ionized physical vapor deposition (IPVD): A review of technology and applications. *Thin Solid Films* **513,** 1–24 (2006).

60. Mattox, D. M. *Handbook of Physical Vapor Deposition (PVD) Processing. Handbook of Physical Vapor Deposition (PVD) Processing* (2010). doi:10.1016/B978-0-8155-2037-5.00007-1

61. Madou, M. J. in *Fundamentals of Microfabrication: The Science of Miniaturization* 49 (2002). doi:10.1038/nmat2518

62. Kovacs, G. T. a, Maluf, N. I. & Petersen, K. E. Bulk micromachining of silicon. *Proc. IEEE* **86,** 1536–1551 (1998).

63. Wu, B., Kumar, A. & Pamarthy, S. High aspect ratio silicon etch: A review. *J. Appl. Phys.* **108,** 8–11 (2010).

64. Marty, F. *et al.* Advanced etching of silicon based on deep reactive ion etching for silicon high aspect ratio microstructures and three-dimensional micro- and nanostructures. *Microelectronics J.* **36,** 673–677 (2005).

65. Ray, T., Zhu, H. & Meldrum, D. R. Deep reactive ion etching of fused silica using a single-coated soft mask layer for bio-analytical applications. *J. Micromechanics Microengineering* **20,** 097002 (2010).

66. Mueller, C. In Situ Techniques for Structure Determination in the Liquid Phase. 1–146 (2014).

67. Zhang, T. Microbridge testing of silicon nitride thin films deposited on silicon wafers. *Acta Mater.* **48,** 2843–2857 (2000).

68. Yang, J. & Paul, O. Fracture properties of LPCVD silicon nitride thin films from the load-deflection of long membranes. *Sensors Actuators, A Phys.* **97-98,** 520–526 (2002).

69. Vlassak, J. J. & Nix, W. D. A New Bulge Test Technique for the Determination of Young Modulus and Poisson Ratio of Thin-Films. *J. Mater. Res.* **7,** 3242–3249 (1992).

70. Kraft, B. O., Volkert, C. a & Kraft, O. Mechanical Testing of Thin Films and Small

Structures. *Adv. Eng. Mater.* **3,** 99–110 (2001).

71. Despont, M., Gross, H., Arrouy, F., Stebler, C. & Staufer, U. Fabrication of a silicon-Pyrex-silicon stack by ac anodic bonding. *Sensors and Actuators a-Physical* **55,** 219–224 (1996).

72. Lukacs, G. L. *et al.* Size-dependent DNA mobility in cytoplasm and nucleus. *J. Biol. Chem.* **275,** 1625–1629 (2000).

73. Giljohann, D. A. *et al.* Gold Nanoparticles for Biology and Medicine. *Angew. Chemie Int. Ed.* **49,** 3280–3294 (2010).

74. Li, H. & Rothberg, L. Colorimetric detection of DNA sequences based on electrostatic interactions with unmodified gold nanoparticles. *Proc. Natl. Acad. Sci. U. S. A.* **101,** 14036–9 (2004).

75. Peckys, D. B. & de Jonge, N. Liquid scanning transmission electron microscopy: imaging protein complexes in their native environment in whole eukaryotic cells. *Microsc. Microanal.* **20,** 346–65 (2014).

76. Liao, J. *et al.* Linear aggregation of gold nanoparticles in ethanol. *Colloids Surfaces A Physicochem. Eng. Asp.* **223,** 177–183 (2003).

77. Bakshi, M. S., Possmayer, F. & Petersen, N. O. Role of different phospholipids in the synthesis of pearl-necklace-type gold-silver bimetallic nanoparticles as bioconjugate materials. *J. Phys. Chem. C* **111,** 14113–14124 (2007).

78. Wang, C., Chen, J., Talavage, T. & Irudayaraj, J. Gold Nanorod/Fe3O4 nanoparticle 'nano-pearl- necklaces' for simultaneous targeting, dual-mode imaging, and photothermal ablation of cancer cells. *Angew. Chemie - Int. Ed.* **48,** 2759–2763 (2009).

79. Park, J. *et al.* Direct observation of nanoparticle superlattice formation by using liquid cell transmission electron microscopy. *ACS Nano* **6,** 2078–2085 (2012).

80. Schneider, N. M. *et al.* Electron-Water interactions and implications for liquid cell electron microscopy. *J. Phys. Chem. C* **118,** 22373–22382 (2014).

81. Shao, L., Kner, P., Rego, E. H. & Gustafsson, M. G. L. Super-resolution 3D microscopy of live whole cells using structured illumination. *Nat. Methods* **8,** 1044–6 (2011).

82. Jones, S. a, Shim, S.-H., He, J. & Zhuang, X. Fast, three-dimensional super-resolution imaging of live cells. *Nat. Methods* **8,** 499–508 (2011).

83. Hell, S. W. & Wichman, J. Breaking the diffraction resolution limit by stimulated emission: stimulated-emission-depletion fluorescence microscopy. *Opt. Lett.* **19,** 780 – 782

(1994).

84. Rust, M. J., Bates, M. & Zhuang, X. W. Sub-diffraction-limit imaging by stochastic optical reconstruction microscopy (STORM). *Nat Methods* **3,** 793–795 (2006).

85. Cella Zanacchi, F. *et al.* Live-cell 3D super-resolution imaging in thick biological samples. *Nat Methods* **8,** 1047–9 (2011).

86. Cohen, M. *et al.* Transmission electron microscope studies of the nuclear envelope in Caenorhabditis elegans embryos. in *Journal of Structural Biology* **140,** 232–240 (2002).

87. Goldberg, M. W. & Allen, T. D. High resolution scanning electron microscopy of the nuclear envelope: Demonstration of a new, regular, fibrous lattice attached to the baskets of the nucleoplasmic face of the nuclear pores. *J. Cell Biol.* **119,** 1429–1440 (1992).

88. Low, S. H. *et al.* The SNARE machinery is involved in apical plasma membrane trafficking in MDCK cells. *J. Cell Biol.* **141,** 1503–1513 (1998).

89. Gray, E. G. Axo-somatic and axo-dendritic synapses of the cerebral cortex. *J. Anat.* **93,** 420–433 (1959).

90. Choi, B. *et al.* Acute Toxicity of Arsenic in Rats and Mice. *Pathology* **15,** 323–334 (2003).

91. McLaughlin, A., Milton, R. & Perry, K. M. A. Toxic manifestations of osmium tetroxide. *Br. J. Ind. Med.* **3,** 183 (1946).

92. Glaeser, R. M. & Taylor, K. A. Radiation damage relative to transmission electron microscopy of biological specimens at low temperature: a review. *J. Microsc.* **112,** 127–138 (1978).

93. Wade, R. H. The temperature dependence of radiation damage in organic and biological materials. *Ultramicroscopy* **14,** 265–270 (1984).

94. Milne, J. L. S. *et al.* Cryo-electron microscopy - A primer for the non-microscopist. *FEBS J.* **280,** 28–45 (2013).

95. Schmid, M. F. Single-particle electron cryotomography (cryoET). *Adv. Protein Chem. Struct. Biol.* **82,** 37–65 (2011).

96. Koster, A., Grimm, R. & Typke, D. Perspectives of molecular and cellular electron tomography. *J. Struct. ...* **120,** 276–308 (1997).

97. Peckys, D. B. & de Jonge, N. Visualizing Gold Nanoparticle Uptake in Live Cells with Liquid. *Nano Lett.* **11,** 1733–1738 (2011).

98. de Jonge, N., Peckys, D. B., Kremers, G. J. & Piston, D. W. Electron microscopy of whole cells in liquid with nanometer resolution. *Proc Natl Acad Sci U S A* **106,** 2159–2164

(2009).

99.     Besztejan, S. *et al.* Visualization of Cellular Components in a Mammalian Cell with Liquid Cell Transmission Electron Microscopy. (In preparation)

100.    Egerton, R. F. Outrun radiation damage with electrons? *Adv. Struct. Chem. Imaging* **1,** 5 (2015).

101.    Isaacson, M., Johnson, D. & Crewe, A. V. Electron Beam Excitation and Damage of Biological Molecules; Its Implications for Specimen Damage in Electron Microscopy. *Radiat. Res.* **55,** 205–224 (1973).

102.    Boudaïffa, B., Cloutier, P., Hunting, D., Huels, M. a & Sanche, L. Resonant formation of DNA strand breaks by low-energy (3 to 20 eV) electrons. *Science* **287,** 1658–1660 (2000).

103.    Köhler, A. & Hurt, E. Exporting RNA from the nucleus to the cytoplasm. *Nature reviews. Molecular cell biology* **8,** 761–773 (2007).

104.    Speese, S. D. *et al.* Nuclear envelope budding enables large ribonucleoprotein particle export during synaptic Wnt signaling. *Cell* **149,** 832–846 (2012).

105.    Kennedy, E., Nelson, E. M., Tanaka, T., Damiano, J. & Timp, G. Live Bacterial Physiology Visualized with Five-Nanometer Resolution Using Scanning Transmission Electron Microscopy. *ACS Nano* acsnano.5b07697 (2016). doi:10.1021/acsnano.5b07697

106.    Gauthier, N. C., Masters, T. A. & Sheetz, M. P. Mechanical feedback between membrane tension and dynamics. *Trends in Cell Biology* **22,** 527–535 (2012).

107.    Gumbiner, B. M. Cell adhesion: The molecular basis of tissue architecture and morphogenesis. *Cell* **84,** 345–357 (1996).

108.    Shafaq-Zadah, M. *et al.* Persistent cell migration and adhesion rely on retrograde transport of β1 integrin. *Nat. Cell Biol.* **18,** 54–64 (2015).

109.    Kim, D., Jeong, Y. Y. & Jon, S. A drug-loaded aptamer-gold nanoparticle bioconjugate for combined CT imaging and therapy of prostate cancer. *ACS Nano* **4,** 3689–3696 (2010).

110.    Liu, H. *et al.* Constitutive and antibody-induced internalization of prostate-specific membrane antigen. *Cancer Res.* **58,** 4055–4060 (1998).

111.    Javier, D. J., Nitin, N., Levy, M., Ellington, A. & Richards-Kortum, R. Aptamer-targeted gold nanoparticles as molecular-specific contrast agents for reflectance imaging. *Bioconjug. Chem.* **19,** 1309–1312 (2008).

112.    Tuerk, C. & Gold, L. Systematic evolution of ligands by exponential enrichment: RNA ligands to bacteriophage T4 DNA polymerase. *Science* **249,** 505–510 (1990).

113. Ellington, A. D. & Szostak, J. W. In vitro selection of RNA molecules that bind specific ligands. *Nature* **346,** 818–22 (1990).

114. Lupold, S. E., Hicke, B. J., Lin, Y. & Coffey, D. S. Identification and characterization of nuclease-stabilized RNA molecules that bind human prostate cancer cells via the prostate-specific membrane antigen. *Cancer Res.* **62,** 4029–4033 (2002).

115. Mirkin, C. a, Letsinger, R. L., Mucic, R. C. & Storhoff, J. J. A DNA-based method for rationally assembling nanoparticles into macroscopic materials. *Nature* **382,** 607–609 (1996).

116. Sigismund, S. *et al.* Clathrin-Mediated Internalization Is Essential for Sustained EGFR Signaling but Dispensable for Degradation. *Dev. Cell* **15,** 209–219 (2008).

117. Garuti, R. *et al.* The modular adaptor protein autosomal recessive hypercholesterolemia (ARH) promotes low density lipoprotein receptor clustering into clathrin-coated pits. *J. Biol. Chem.* **280,** 40996–41004 (2005).

118. Cataldo, a M. *et al.* Endocytic pathway abnormalities precede amyloid beta deposition in sporadic Alzheimer's disease and Down syndrome: differential effects of APOE genotype and presenilin mutations. *Am. J. Pathol.* **157,** 277–286 (2000).

119. Pal, A., Severin, F., Hopfner, S. & Zerial, M. Regulation of Endosome Dynamics by Rab5 and Huntingtin-HAP40 Effector Complex in Physiological versus Pathological Conditions. *Methods in Enzymology* **438,** 239–257 (2008).

120. Pinheiro, A. V, Han, D., Shih, W. M. & Yan, H. Challenges and opportunities for structural DNA nanotechnology. *Nat. Nanotechnol.* **6,** 763–72 (2011).

121. Nowald, J. DNA-Templated Self Assembly of Protein Arrays and Highly Conductive Nanowires. *Science (80-. ).* **301,** 1882–1884 (2003).

122. Andersen, E. S. *et al.* Self-assembly of a nanoscale DNA box with a controllable lid. *Nature* **459,** 73–6 (2009).

123. Mathur, D. & Henderson, E. R. Complex DNA nanostructures from oligonucleotide ensembles. *ACS Synthetic Biology* **2,** 180–185 (2013).

124. Han, D. R. *et al.* DNA Origami with Complex Curvatures in Three-Dimensional Space. *Science (80-. ).* **332,** 342–346 (2011).

125. Yan, H., LaBean, T. H., Feng, L. & Reif, J. H. Directed nucleation assembly of DNA tile complexes for barcode-patterned lattices. *Proc. Natl. Acad. Sci. U. S. A.* **100,** 8103–8108 (2003).

126. Shih, W. M., Quispe, J. D. & Joyce, G. F. A 1.7-kilobase single-stranded DNA that folds into a nanoscale octahedron. *Nature* **427,** 618–621 (2004).

127. Rothemund, P. W. K. Folding DNA to create nanoscale shapes and patterns. *Nature* **440,** 297–302 (2006).

128. Pauling, L. *General Chemistry. Foundations of Chemistry* **159,** (1988).

129. Boyle, J. Lehninger principles of biochemistry (4th ed.): Nelson, D., and Cox, M. *Biochem. Mol. Biol. Educ.* **33,** 74–75 (2005).

130. Morgan, J. & Warren, B. E. X-Ray Analysis of the Structure of Water. *J. Chem. Phys.* **6,** 666 (1938).

131. Narten,  a. H. Liquid Water: Molecular Correlation Functions from X-Ray Diffraction. *J. Chem. Phys.* **55,** 2263 (1971).

132. Hermansson, K. A simulated X-ray diffraction study of liquid water : beyond the spherical-atom approximation. *Chemical Physics Letters.* **2614,** (1996).

133. Gorbatyi, Yu. E. & Dem'yanets, Yu. N. X-ray diffraction studies of the structure of liquid and supercritical water at high temperatures and pressures. II. The molecular density radial distribution functions and the paired correlation functions. *J. Structural Chemistry.* **24**, 385–392 (1983).

134. Radnai, T. & Ohtaki, H. X-ray diffraction studies on the structure of water at high temperatures and pressures. *Mol. Phys.* **87,** 103–121 (1996).

135. Amann-Winkel, K. *et al.* X-ray and Neutron Scattering of Water. *Chem. Rev.* acs.chemrev.5b00663 (2016). doi:10.1021/acs.chemrev.5b00663

136. Lengyel S. & Kalman E. Electron diffraction on liquid water. *Nature* **248**, 405–406 (1974).

137. Hada, M. *et al.* Cold ablation driven by localized forces in alkali halides. *Nat. Commun.* **5,** 3863 (2014).

138. Coleman, M. V. & Thomas, D. J. D. The structure of amorphous silicon nitride films. *Phys. Status Solidi* **25,** 241–252 (1968).

139. Cao, J., Ihee, H. & Zewail,  a H. Ultrafast electron diffraction and direct observation of transient structures in a chemical reaction. *Proc. Natl. Acad. Sci. U. S. A.* **96,** 338–342 (1999).

140. Pettersson, L. G. M., Henchman, R. H. & Nilsson, A. Water—The Most Anomalous Liquid. *Chem. Rev.* **116,** 7459–7462 (2016).

141. Ishikawa, T. *et al.* Direct observation of collective modes coupled to molecular orbital-

driven charge transfer. *Science (80-. ).* **350,** 1501–1505 (2015).

142. Ishikawa, T. *et al.* Large and ultrafast photoinduced reflectivity change in the charge separated phase of Et2 Me2 Sb [Pd (1,3-dithiol-2-thione-4,5-dithiolate) 2] 2. *Phys. Rev. B - Condens. Matter Mater. Phys.* **80,** 1–8 (2009).

143. Li, Q. *et al.* Bond competition and phase evolution on the IrTe2 surface. *Nat. Commun.* **5,** 1–7 (2014).

144. Oh, Y. S., Yang, J. J., Horibe, Y. & Cheong, S. W. Anionic depolymerization transition in IrTe2. *Phys. Rev. Lett.* **110,** (2013).

145. Han, G., Chen, Z. G., Drennan, J. & Zou, J. Indium selenides: Structural characteristics, synthesis and their thermoelectric performances. *Small* **10,** 2747–2765 (2014).

146. Jacobs-Gedrim, R. B. *et al.* Extraordinary photoresponse in two-dimensional In2Se3 nanosheets. *ACS Nano* **8,** 514–521 (2014).

147. Doan, S. C., Kuzmanich, G., Gard, M. N., Garcia-Garibay, M. A. & Schwartz, B. J. Ultrafast spectroscopic observation of a quantum chain reaction: The photodecarbonylation of nanocrystalline diphenylcyclopropenone. *J. Phys. Chem. Lett.* **3,** 81–86 (2012).

148. Takeuchi, S. & Tahara, T. Femtosecond absorption study of photodissociation of diphenylcyclopropenone in solution: Reaction dynamics and coherent nuclear motion. *J. Chem. Phys.* **120,** 4768–4776 (2004).

149. Shchepetov, A. *et al.* Ultra-thin free-standing single crystalline silicon membranes with strain control. *Appl. Phys. Lett.* **102,** 10–14 (2013).

150. Manzo, C. & Garcia-Parajo, M. F. A review of progress in single particle tracking: from methods to biophysical insights. *Rep Prog Phys* **78,** 124601 (2015).

151. Deniz, A. a, Mukhopadhyay, S. & Lemke, E. a. Single-molecule biophysics: at the interface of biology, physics and chemistry. *J. R. Soc. Interface* **5,** 15–45 (2008).

152. Besztejan, S. Metal Ion Based Probes for Imaging. (2016).

# 13.   Appendix

**Appendix-1: Nanofabrication and Cleaning Protocols**

In this thesis, the recipe for the nanofluidic cell fabrication is adapted to Micro-structuring facility of Technical University of Hamburg (TUHH). The process flow of the fabrication and the recipe for the honeycomb patterned nanofluidic cells are developed and implemented in the collaboration with Trieu Group (Deybith Venegas Rojas, Svenja Riekeberg and Prof. Hoc Khiem Trieu) in TUHH. The success -quality and yield- of these processes strongly depends on the parameters and the materials chosen. The yield of the nanofluidic cell fabrication is generally over 90% since it is a relatively straightforward process with well-defined parameters compared to honeycomb patterned cells. The fabrication process of honeycomb patterned cells requires further trials to optimize process parameters and the geometries of the features.

The recipes used in this thesis study are given below. The obtained results with the given parameters here can show variations in different machines, or even with the same machine but in different times. Ideally, the parameters of the key steps such as lithography or (D)RIE should be characterized before preparing a new batch.

## 1.1.   Cleaning Procedures

In order to remove organic contaminants and from the liquid cell surface, hot piranha cleaning can be implemented. Another effective cleaning procedure, namely RCA (Radio Corporation of America) cleaning, can be used to remove metallic residues from the cell surface.

In this thesis, we routinely used piranha cleaning for the nanocells. We also used plasma cleaning for ~1 min to further increase the hydrophilicity of the nanocell surface.

### 1.1.1.   Piranha cleaning

A ratio of 3:1 of sulfuric acid ($H_2SO_4$, 98%) and hydrogen peroxide ($H_2O_2$, 30%) at 80-100 ºC for 30 min is used to clean the nanocells. In the process, hydrogen peroxide is added drop by drop into sulfuric acid, which is stirred continuously. Then, the solution is heated up and the nanocells are placed in the solution bath. A Teflon holder is used for TEM cells to ease the handling as shown in Figure A1.1. The cells are transferred into $dH_2O$ after piranha solution and then blow dried with compressed nitrogen.

Figure A1.1. Teflon holder for piranha cleaning.

### 1.1.2. RCA cleaning

In the procedure, a solution of ammonium hydroxide, hydrogen peroxide and water (ratio 1:1:5) is heated up to 70-80 °C to remove organic contamination. Then, natural grown oxide on silicon is removed with diluted hydrofluoric acid (ratio 1:50 in water). Finally, metallic contaminants are removed with a mixture of hydrochloric acid, hydrogen peroxide and deionized (DI) water (ratio 1:1:6). Samples are rinsed with deionized water and dried in between the steps and as a final step.

### 1.2. Photoresist

In the spin coating process, wafers need to be pre-baked on a hot plate at 120 °C for at least 10 min to remove all the moisture. A fresh developer solution of precisely 0.5% NaOH at 25 °C is set each time prior the spin coating. The spinner chuck in TUHH is intended for 100 mm wafers. Before spinning the photoresist, a primer, namely Ti primer, is spin coated on the wafers with 4500 rpm (revolutions per minute) for 20 sec (accl.-dccl. speed 500 rpm). Primer increases the adhesion of the photoresist. Then, the wafers are hard-baked at 120 °C for >2 min. A ~3 mL volume of a positive photoresist, HPR-504, is spin coated on the primer coated side of the wafer with 2000 rpm (accl. 5000 rpm, dccl. 1500 rpm) for 20 sec resulting around 2 μm resist thickness. The wafers are then hard-baked again at 105 °C for 1 min. The second baking time is crucial to achieve the ideal resist strength. Similar results could be achieved with an alternative photoresist, AZ3662. Here, no back-side spin is necessary.

HPR-504 is also used as glue to bond the thin Si wafers to dummy wafers for support. The same parameters given above are used to coat the resist on the dummies. Then, the thin wafer

is carefully placed and aligned on the dummy, a soft tool is used to press gently on the wafer stack to achieve a good contact.

A different photoresist, AZ9260, is used in the fabrication of the reinforced liquid cells. This resist is more viscous than HPR-504 resulting in thicker layers, which is important to stand in many DRIE cycles. It is coated with 2000 rpm (accl. 5000 rpm, dccl. 1500 rpm) for 20 sec resulting around 9-10 μm resist thickness. Upon spin coating, the wafers are baked on a hot plate at 105 °C for 5 min 30 sec.

## 1.3.    Photolithography

The mask aligners, EVG 620 and Süss MA 4 with front and back side alignment functions, both equipped with mercury UV-lamp are used for patterning the photoresists in this thesis. In EVG 620, the exposure is set to 53-60 mJ/cm$^2$ for 2 μm thick HPR-504. The soft exposure is used for large features (>10 μm). In soft exposure mode, the wafer and the mask are in contact but the mask is not pressing on the wafer. This keeps the mask clean and also extends its life span. The alignment tool measures the exposure time automatically. The mask features for the front side are aligned with the wafer by using horizontal alignment gaps overlapped with the primary flat of the wafer. The back side features are aligned with the front ones using the alignment marks placed on the two sides of the wafer perimeter.

Süss MA 4 is used for AZ9260 in hard contact mode (vacuum contact) with 6 min 45 sec exposure time.

A developer solution of 0.5% NaOH at 25 °C is used for HPR-504 for 10-15 sec. The wafer is moved rigorously in the developer bath and then placed in DI water bath for >10 min. For AZ9260, 1% NaOH at 25 °C is used for 45-60 sec and then rinsed. The wafer is spin-dried and placed in 90 °C oven for 2 h to strengthen the photoresist before DRIE (only for AZ9260).

## 1.4.    Dry Etching

The plasma etching system used in this work is CO31 Alcatel SEL, Advanced Silicon Etching and Advanced Oxide Etching (ASE/AOE). To remove 50 nm SiN, SF$_6$ (130 sccm) and O$_2$ (13 sccm) gases are used. The plasma is generated with an ICP power of 350 W and etching is performed with an RIE power of 16 W. The wafer is continuously cooled through the helium pressure, which is crucial especially for long etching processes. The etching time for 50 nm SiN was experienced as 85-110 sec resulting usually a few microns over-etch in silicon. This over-

etch is not important at this point since the silicon is etched all the way to the backside SiN layer in the next step.

It should be noted here that the selectivity of plasma etching for SiN/Si is poor. Therefore, as a general approach, a sacrificial layer is included between them in order to protect one of the layers. Silicon oxide is commonly used as a sacrificial layer as we did for honeycomb patterned cells. The etch rate of the $SF_6$–$O_2$ plasma in silicon oxide is much slower compared to that for both silicon and SiN.

In etching of 100 µm deep features with DRIE, the used ICP and RIE powers are 350 W and 13 W, respectively. The $SF_6$ (130 sccm) and $O_2$ (13 sccm) gases are used for etching and $C_4F_8$ (85 sccm) is used as passivation layer. One etch cycle is set as 12 s of etching and 6 s of passivation. The silicon is etched until the oxide with ~200 cycles, which corresponds to an etch rate of 0.5 µm/cycle. The blue-purple color of oxide is a good indicator to stop the etching. The etching is performed with smaller steps (10-20 cycles) through the end of the process and the hexagons are checked in between the etching steps with a light microscope.

It is well-known for plasma etching that the etch rate is higher in larger features. It is more difficult to remove byproducts in small features. Accumulation of the byproducts in the features slows down and eventually stops the etching.

## 1.5. Wet Etching

KOH etching is mainly used in the nanofluidic cell fabrication with SiN layer as hard mask. A concentration of 20% KOH in water at 90 °C is generally used in this thesis. It was experienced that it takes ~150 min to etch 300 µm thick Si wafer suggesting an etch rate of ~2 µm/min. The etch rate is heavily depending on the concentration and temperature. Using higher KOH concentration with the addition of isopropanol results in much slower etch rates, however a smoother etch profile. The wafer is rinsed in a water bath for minimum ~10 min after the etching, spin-dried and the windows are characterized with a light microscope.

BOE is used to pattern the oxide spacer into the channel features in the nanocell and to remove the sacrificial layer in the reinforced nanocell. The BOE solution contains a ratio of 6:1 of $NH_4F$ (40% in water) and HF (49% in water). The HPR-504 is used as masking layer. BOE also attacks photoresist but the process takes ~2 min for removing 100-120 nm oxide and relatively thick photoresist can survive for such short time. The etching time depends on the type of the SiO (stoichiometry and deposition method).

For reinforced nanocells, the wafer is etched in BOE for slightly longer times due to the small features with high aspect ratios and additional 9-10 μm resist thickness. The ideal etching time was experienced to be around 4 min.

The concentrated HF (50%) is used to etch Pyrex glass wafers with ~200 nm polysilicon as hard mask. The HPR-504 is spin-coated with the given recipe above to pattern and further protect the polysilicon during the etching. The photoresist is reinforced with a temperature ramp in an oven. The wafer is placed in the oven and it is heated up to 180 °C, kept for 1 h at this temperature, then slowly cooled down to room temperature. The polysilicon is patterned with $SF_6$ plasma and then HF etching for Pyrex is performed.

## 1.6.  Thin-film Deposition

The sputtering deposition is used to deposit SiO for the spacer material of the nanocell. An Ar-$N_2$O plasma is used with 200 W HF for the deposition at a temperature of <200 °C. A deposition rate of ~10 nm/min was experienced. We found that the etching time with BOE is similar for the oxide films deposited by sputtering and PECVD, indicating similar film strength.

Thermally grown oxide as sacrificial layer for the reinforced nanocells was obtained commercially.

## 1.7.  Silicon-Glass Anodic Bonding

The thin silicon wafers are bonded to 500 μm thick Pyrex glass wafers at a temperature and voltage of 380 °C and 800 V, respectively. The chamber pressure is $1.0 \times 10^{-2}$ mbar. A pressure of 1000 N is applied to the whole wafer surface during the bonding and the process takes 45 min.

**Appendix-2: Preparation of DNA-AuNPs and their Characterization**

The samples of DNA-AuNPs, anti-PSMA-RNA aptamer AuNPs were prepared and the cell culture for in-liquid TEM studies was performed by Dr. Stephanie Besztejan at the Chemistry Department, Institute for Biochemistry and Molecular Biology of the University of Hamburg.[152]

**2.1. Coupling of AuNPs with thiol-modified oligonucleotides**

Citrate stabilized AuNPs were provided by the Center for Applied Nanotechnology GmbH (CAN), Hamburg, Germany (Katja Werner).

Thiol-modified DNA (100 µM) was purchased from (DNA1) IBA GmbH (Göttingen, Germany) and (DNA2) Life Technologies (Carlsbad, USA). The batch sizes for both DNA1-AuNP and DNA2-AuNP were set to 2 mL. For coupling of DNA1 to the 17.5 nm AuNP (4.5 nM), 1.6 nmol DNA1 was required to cover the particle's surface with approximately 200 binding positions. Due to the larger surface of the 63.8 nm AuNP (197 pM), 2000 potential binding positions were estimated for DNA2-AuNP, thus 0.76 nmol DNA2 used for coupling. For reduction of disulfide bonds between the DNA strands, 16 µL of DNA1 and 8 µL of DNA2 were incubated with 8 µM tris(2-carboxyethyl)phosphine (TCEP) for 30 min at room temperature. The AuNP and DNA solutions were mixed and the final solution was shook at 300 rpm and 25°C for 14 h. Then, the DNA-AuNPs were matured via salt aging in 10 steps by adding NaCl and sodium phosphate buffer to the DNA-AuNP mix to final concentrations of 0.1 M and 0.01 M, respectively. This mixture was incubated overnight. Unbound DNA was washed away by centrifugation of the DNA-AuNPs at 21,000xg and room temperature for 15 min.[115] The DNA-AuNP pellet was resuspended in ddH2O and the solution was characterized via DLS and UV-Visible (UV-Vis) spectroscopy.

**2.1.1. DLS Measurements**

The diameter of the AuNPs was analyzed before and after coupling. A Malvern Zetasizer Nano ZS ZEN 3600 (Malvern Instruments Ltd, Malvern, United Kingdom) was used for the analysis with disposable low volume cuvettes. A solution of 50 µL AuNP was analyzed for each sample (before and after coupling and after hybridization). Each measurement involves 15 cycles and was repeated 3 times. Table A2.1 shows the mean diameters of the AuNPs before and after DNA coupling.

Table A2.1. Mean diameters of AuNPs before and after DNA coupling

| Nanoparticles | Mean Diameters (nm) | |
|---|---|---|
| | Before Coupling | After Coupling |
| 17.5 nm | 23±1 | 84±10 |
| 60 nm | 67±3 | 113±7 |

## 2.1.2. UV-Vis Measurements

UV-Vis analysis was performed to examine the surface plasmon resonance (SPR) of the AuNPs before and after coupling. Bigger hydrodynamic shells shift the maximum peak position to higher wavelengths (Figure A2.1 A). The spectra were measured in 96 well plates using a TECAN M200 Pro multiplate reader (Tecan Group AG, Männedorf, Swiss) in absorbance scanning mode at 400-700 nm.

## 2.1.3. Hybridization of DNA-AuNPs with a combining DNA-strand (Hyb-DNA)

The DNA1-AuNPs and DNA2-AuNPs were mixed together with either control DNA or Hyb-DNA. Hybridization was fostered by a temperature gradient of 1°C/min from 80 to 20 °C in a BioRad Mastercycler Gradient (BioRad Laboratories, Berkeley, USA). After hybridization, the structures were analyzed by DLS, UV-Vis and in-liquid TEM.
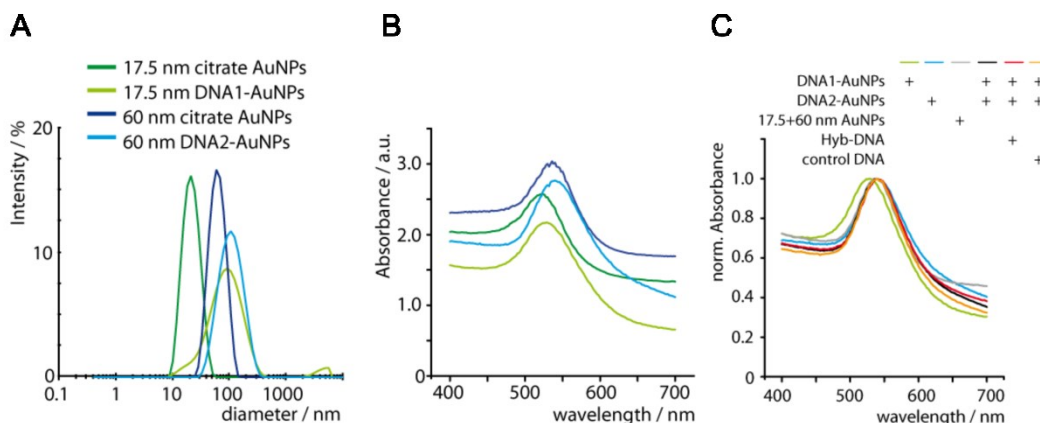


Figure A2.1. (A) DLS analysis of AuNPs before and after coupling with thiol-modified DNA. (B) UV-Vis spectra of AuNPs before and after coupling. (C) UV-Vis spectra of AuNPs after hybridization. (Adapted from reference-47).

**Appendix-3: Preparation of anti-PSMA-RNA-aptamer AuNPs and Cell Culture Protocol**

**3.1.    Synthesis of 2'-fluoropyrimidine stabilized anti-PSMA-RNA aptamers**

The 2'-fluoropyrimidine stabilized PSMA-RNA aptamers (A9) were used for 20 nm large AuNPs.[109,114] The T7 RNA polymerase variant Y639F was used to synthesize the aptamer and a scrambled control RNA. The sequence contains hybridizing extension for 5'-thiol modified ssDNA to immobilize on AuNPs. The transcription reaction was performed in a mixture (a typical volume of 20 µL) containing 40 mmol/L Tris (pH 8), 30 mmol/L $MgCl_2$, and 5 mmol/L spermidine, 1 mmol/L ATP and GTP, 2 mmol/L of 2' F dCTP, 2' F dUTP (TriLink Biotech, CA), and 2 ng dsDNA template at 42 °C for 4 h. After transcription, the DNA was removed enzymatically at 37 °C for 10 min. Then, the RNA was purified with electrophoresis using denaturing 10% polyacrylamide gel. It was extracted and recovered afterwards by ethanol precipitation.

The RNA aptamer was hybridized with complementary ssDNA on the AuNP surfaces. A control sequence was also designed to check the specificity of the hybridization. Table A3.1 shows RNA and DNA sequences used in the experiments.  Table A3.2 shows the mean diameters of the AuNPs measured with DLS before and after DNA coupling.

**3.2.    Preparation of anti-PSMA-RNA aptamer AuNPs**

A single stranded 5'-thiol modified capture DNA was coupled using a protocol reported by Mirkin et al.[115] Aptamers were mixed with the AuNP solution to start the hybridization between the capture oligonucleotide and aptamer. For hybridization, the mixture solution was heated up to 80 °C and cooled down to 20 °C with temperature steps of 1 °C/min. The unbound aptamers were separated via centrifugation and discarded in three consecutive washing steps. Then, the anti-PSMA-AuNPs were analyzed by DLS (Table A3.2). The details of the DLS measurements are given in Appendix-2.

Table A3.1. RNA and DNA sequences used in the experiments. Grey highlighted subunits show aptamer and scrambled control, respectively. Underlined subunits show the complementary units for hybridization

| Name | Length/nt | Sequence |
| --- | --- | --- |
| Anti-PSMA A9 | 91 | GGG AGG ACG AUG CGG ACC GAA AAA GAC CUG ACU UCU AUA CUA AGU CUA CGU UCC CAG ACG ACU CGC CCG ACG ACG ACG ACG ACG ACG A |
| scrambled Anti-PSMA A9 | 92 | GGG AGG ACG AUG CGG CAG GCA UGC CUA GCU AAG CAG CCC AUG GCU UAU GCG CGG ACA GAC GAC UCG CCC GAC GAC GAC GAC GAC GAC GA |
| 5'-thiol modified capture DNA | 33 | 5-HS-CC-AAAAAAAAAA-TCG TCG TCG TCG TCG TCG TCG |
| T7 promotor | 33 | *TAA TAC GAC TCA CTA TA*G GGA GGA CGA TGC GG |
| anti-PSMA DNA template | 91 | GGG AGG ACG ATG CGG ACC GAA AAA GAC CTG ACT TCT ATA CTA AGT CTA CGT TCC CAG ACG ACT CGC CCG ACG ACG ACG ACG ACG ACG A |
| scrambled anti-PSMA A9 DNA template | 92 | GGG AGG ACG ATG CGG CAG GCA TGC CTA GCT AAG CAG CCC ATG GCT TAT GCG CGG ACA GAC GAC TCG CCC GAC GAC GAC GAC GAC GAC GAC GA |

Table A3.2. Mean diameters of the AuNPs measured with DLS before and after DNA coupling

| Sample | Diameter (nm) |
| --- | --- |
| 20 nm AuNPs | 27.9±2 |
| Coupled AuNPs | 46.2±5 |
| Anti-PSMA-AuNPs | 135±23 |
| Control PSMA-AuNPs | 730±293 |

## 3.3.    Cell culture

PC3 cells were cultivated in a 1:1 mixture of Ham's F12 and RPMI 1640, accompanied with 10 % fetal calf serum (FCS) and 1 % Penicillin/Streptomycin. LNCaP cells were cultivated in RPMI 1640 mixed with 20 % fetal calf serum and 1 % Penicillin/Streptomycin.

For in-liquid TEM measurements, a number of $\sim10^5$ PC3 or LNCaP cells were seeded on the SiN surface in a conventional cell culture dish. The PC3 and LNCaP cells were grown for up to 24 h at 37 °C and 5 % $CO_2$ in the corresponding media. The cell density was checked via light microscopy. The cells were prepared for imaging by either fixation with 4 % paraformaldehyde or without fixation.

For anti-PSMA-AuNP treatment, the LNCaP cells were seeded 24 h before the in-liquid TEM imaging. The cells were washed twice with PBS and incubated in a media containing of RPMI 1640 and 10 % Hepes for 30 min before adding anti-PSMA-AuNP. The anti-PSMA-AuNPs and control PSMA-AuNPs were mixed at a final concentration of 1 nM. The sample was incubated up to 20 min at 37 °C before imaging with either dark field light microscopy or in-liquid TEM.

**Appendix-4: List of used substances according to GHS**

Table A4.1. Hazardous substances used in this work, marked with according pictograms and H (hazard) and P (precautionary) statements

| Substance | Pictogram | H-Statements | P-Statements |
|---|---|---|---|
| Acetone | | 225, 319, 336 | 210, 261, 305+351+338 |
| Ethanol | | 225, 319 | 210, 240, 305+351+338, 403+233 |
| Hydrofluoric acid | | 330, 310, 300, 314 | 260, 264, 280, 284, 301+310-302+350 |
| Hydrogen peroxide | | 271, 302, 314, 332, 335, 412 | 220, 261, 280, 305+351+338-310 |
| Isopropanol | | 225, 319, 336 | 210, 261, 305+351+338 |
| Potassium hydroxide | | 302, 314 | 280, 305+351+338, 310 |
| Sodium hydroxide | | 314 | 280, 305+351+338, 310 |
| Sulfuric acid | | 314 | 260, 264, 280, 301+330+331, 303+361+353, 363, 304+340, 305+351+338, 310, 321, 310, 405, 501 |

# 14.    Acknowledgement

study. I am honored to have worked with and learnt from them in the very interesting and the highest ranked studies.

I would like to thank Dr. Sascha Epp for his valuable input in numerous situations during the project.

I would like to thank Dr. Christina Müller for providing nanofabrication training and her guidance in the beginning of the project.

I would like to thank the remarkable engineers of Miller group, Djordje Gitaric and Josef Gonschior for all the clever designs and Carsten Meklenburg (Mecki) for great machining and also being my informal German teacher.

I thank the entire Miller group, Dr. Andreas Rossos, Dr. Wesley Robertson, Yinfei Lu, Maria Katsiaflaka, Khalid Siddiqui… for their support and friendship.

Finally, I thank my dear wife Esengül for her matchless support from the beginning of my journey in science. I am truly blessed to have her in my life. We have faced difficulties, shared happiness and enjoyed life together. I owe her so much for my success.

I am also one lucky man to have such a great mother and father, no one has better ones.

## 15. Declaration on oath

"I hereby declare on oath, that I have written the present dissertation by my own and have not used other than the acknowledged resources and aids. The submitted written version corresponds to the version on the electronic storage medium. I hereby declare that I have not previously applied or pursued for a doctorate (Ph.D. studies)." 28.11.2016